UiT
THE ARCTIC UNIVERSITY OF NORWAY

Faculty of Science and Technology
Department of Geosciences

# The Link Between Fluid Flow and Glacial Erosion Along the Ringvassøy- Loppa Fault Complex, Tromsøflaket, SW Barents Sea

**June Berg**

*EOM-3901 Master's Thesis in Energy, Climate and Environment*
*June 2017*

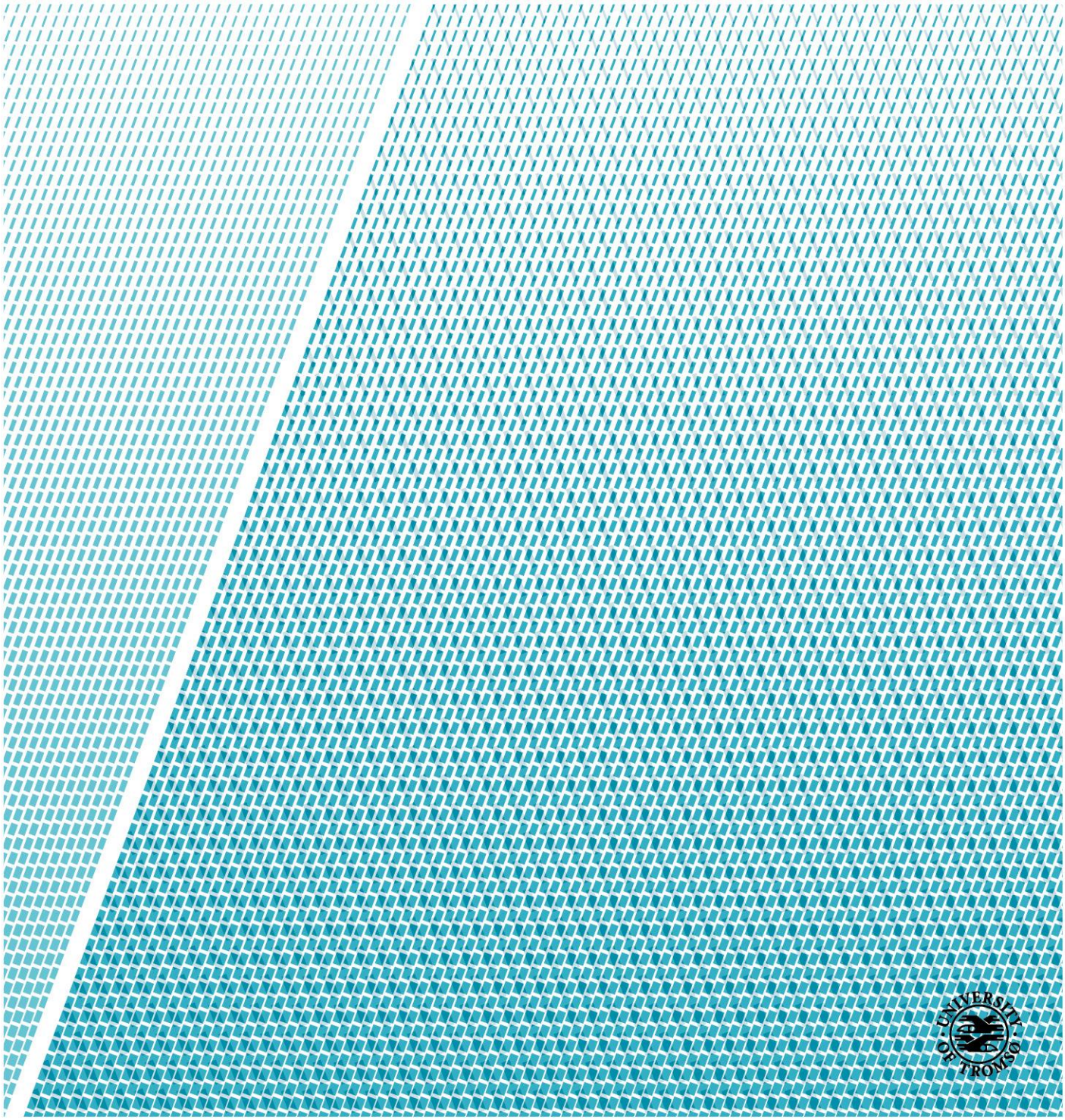

# Abstract

This master thesis has focused its efforts to investigate the link between glacial erosion and focused fluid flow in the SW Barents Sea, on the shallow bank area of Tromsøflaket where the Ringvassøy-Loppa Fault Complex borders the Tromsø basin in west, and the Loppa High in east. Here, large, elongated depressions are identified on the buried Upper Regional Unconformity (URU) and may resemble tunnel valleys or are related to fluid flow and gas hydrate formation beneath the Barents Sea ice sheet. The thesis is based on a 3D seismic dataset, the Caliente 3D, two sets of 2D seismic lines (the SH-8601 and SH-9103) and well data from two wells (well 7120/1-1 and 7120/1-2).

Mapping of faults, stratigraphy and amplitude anomalies revealed that vertical fluid migration are dominated by the faulted nature of the study area, which promote leakage of deep thermogenic gas into shallow Tertiary units. Above the base Tertiary reflector a change from vertical to lateral migration is observed. Together with the faults, the shallowing seismic stratigraphy focusses fluid migration towards the Loppa High in East and where the permeable carrier beds are truncated by the URU. Four elongated deep depression, with well-developed bases and sides are identified on the URU, these exhibit clear orientations reminiscent of paleo ice stream directions on the Barents Sea shelf. Several theories for their generation is argued, relating them to tunnel valleys and hill-hole pairs. The spatial relation of the depressions with the fluid flow system within the study area suggests that focussed fluid flow and glacial erosion are likely to have played a major part in their origin. Eventually a four-stage conceptual model is inferred for their formation, where localized formation of gas hydrates create sticky spots underneath the Barents Sea Ice Sheet, and a weak decollement failure plane at the base of the fluctuating GHSZ leads to glacial erosion of the depressions and re-deposition of the gas hydrate bearing sediments

# Forord

Etter fem lange år med krevende studier er det endelig tid for innlevering av det siste verket. Studietiden har vært en spennende tid som har gått alt for fort. Jeg sitter igjen med mange gode minner og venner for livet. Selv om det ikke blir enkelt, skal jeg gjøre et forsøk på å takke alle som har bidratt til å gjøre studietiden så bra som den har vært.

Jeg vil først takke veileder Stefan Bünz for raske tilbakemeldinger gjennom en hektisk masteroppgave. Jeg ønsker å takke for at du har gitt meg muligheten til å jobbe med en spennende oppgave.

Det må også rettes en stor takk til resten av EKM-gjengen. Jeg setter utrolig stor pris på det gode samholdet, det ville vært vanskelig å komme i mål med sivilingeniørgraden uten dere! Guttene på kontoret (Petter, Jarl-Eirik, Jørn og Bjørnar) fortjener en ekstra takk for nødvendige kaffepauser, dilemmas, triksing og latter.

En stor takk sendes også til familien min for all økonomisk støtte og kjærlighet.

June Berg
Juni 2017

# Table of Content

# 1 Objectives

The objectives of this master thesis are to investigate the relationship between focussed fluid flow and glacial erosion in the in the SW Barents Sea, on the shallow bank area of Tromsøflaket where the Ringvassøy-Loppa Fault Complex borders the Tromsø basin in west, and the Loppa High in east.

# 2 Introduction

## 2.1 Subsurface fluid migration dynamics

Fluid migration is the movement of all fluids in the subsurface. Petroleum migration generally classifies different categories of migration based on the path hydrocarbons are following, primary, secondary and tertiary (Figure 2.1-1). Primary migration is the expulsion of petroleum from a source rock into adjacent rocks, whereas secondary migration is the flow of hydrocarbons through carrier beds and to the reservoir (Selly & Sonnenberg, 2015) (Bjørlykke, 2010). Tertiary migration or dismigration relates to the movement hydrocarbons may take once confined in a trap, for instance remobilisation in the form of leakage or seepage at surface (Durand, 1988). The exact process of primary migration is not clear, and there are many theories (Selly & Sonnenberg, 2015). This thesis will not go further into detail to what processes governs expulsion of hydrocarbons from source rock, but focus on the secondary and tertiary migration mechanisms.

Familiarity with the processes occurring in the subsurface and their relation to fluid migration is vital, and the subsequent sections will look at the fundamental dynamics governing fluid flow and the different migration mechanisms. Lastly we will state a simple migration model.

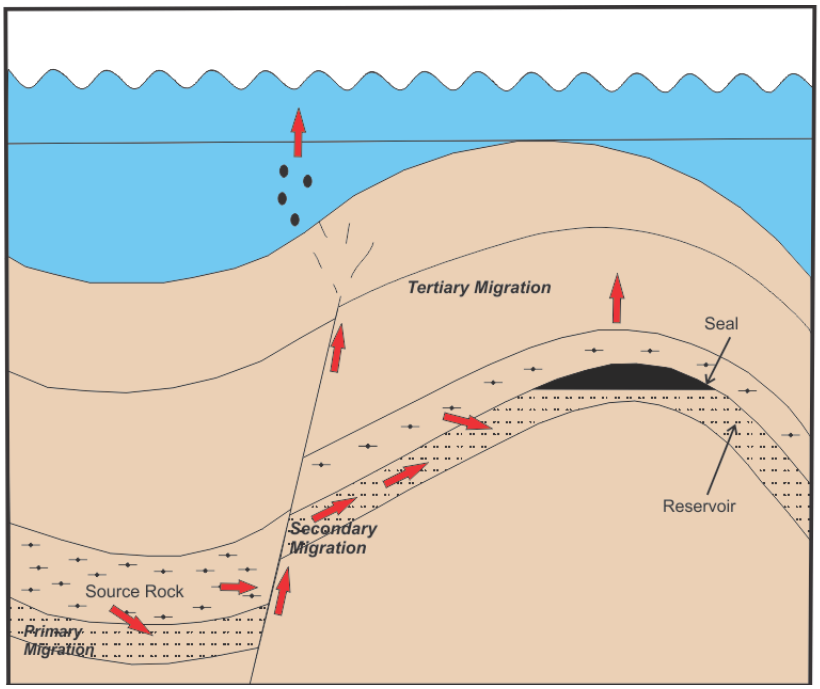


***Figure 2.1-1*** *Schematic presentation of primary, secondary and tertiary migration. Figure modified from Tissot & Welte (1978).*

### 2.1.1 Pressure

We know from rudimentary physics that pressure is the force per unit area acting on a surface. In the subsurface, we mainly talk about the overburden pressure that can be further divided into lithostatic pressure and fluid pressure. Lithostatic pressure refers to the pressure exerted by the weight of overlying sediments, and varies with depth, density, and the extent to which water pressure limits the grain-to-grain contact. Lithostatic pressure has a gradient of approximately 1psi/ft (Fertl & Chilingarian, 1976).

Fluid pressure is due to the fluids existing within the pore space and there are two types, hydrostatic and hydrodynamic. Hydrostatic pressure is caused by a column of fluid at rest, and has a gradient about 0.465 psi/ft (Selly & Sonnenberg, 2015). Formations where the pressure deviates from the hydrostatic gradient are either overpressured or underpressured, this could have many possible causes, the most common being artesian, structural, compactional and diagenetic (Fertl & Chilingarian, 1976).

Hydrodynamic pressure relates to groundwater fluid flow, which sets up a hydrodynamic pressure gradient, or fluid potential gradient. Water in the carrier beds will flow from an area of high potential to areas of low potential, setting up the gradient. This mechanism is one of the driving forces for secondary and tertiary migration, but in most cases it has relatively low importance and do not compare to the effects of buoyancy (Durand, 1988).

### 2.1.2 Buoyancy force

The main driving force for secondary and tertiary separate phase migration is the buoyancy force. The buoyancy force is set up due to density difference of immiscible fluids, such as hydrocarbons and water, and since hydrocarbons have lower densities they will rise and upward movement occur. The greater the density difference between the immiscible phases, the greater the buoyancy force and the rise (Schowalter, 1979; Durand, 1988; Bjørlykke, 2010).

The buoyancy force is a function of the density contrast between the hydrocarbon phase ($\rho_o$), the water phase ($\rho_w$), and the height (H) of the continuous hydrocarbon column.

$$BF = (\rho w - \rho o)H \quad (1)$$

The pressure in the water phase for a 100m high and narrow oil column with a density of 0,8g/cm3 is 1MPa, and for the oil phase it is 0,8MPa, hence the pressure difference between the oil and water face is 0,2MPa for each 100m. (Bjørlykke, 2010)

In the subsurface hydrocarbons needs to migrate through narrow pores in rocks that set up resisting forces. However, as long as the buoyance force is greater than any resisting force, the fluids will migrate. The main resisting force in the subsurface is the capillary force revised in the following section (Verweij, 1993).

### 2.1.3 Capillary force

*"The capillary pressure is the difference between the ambient pressure and the pressure exerted by a column of liquid"* (Selly & Sonnenberg, 2015).

In geological terms, the capillary pressure is related to the pore throat diameter in the sense that the capillary pressure is inversely proportional to pore size. The capillary pressure is also related to the interfacial tension between fluids and the wettability. The pressure at which a fluid imbibe the pore throats is called the capillary entry pressure, and once exceeded, fluid intrusion increases until the irreducible saturation of the fluid that previously occupied the reservoir is reached, usually the irreducible water saturation (Selly & Sonnenberg, 2015). The capillary pressure ($P_c$) for water-wet reservoirs is given by the following equation:

$$Pc = \frac{2\gamma cos\theta}{R} \quad (2)$$

Where the capillary pressure is a function of the interfacial tension ($\gamma$) between water and petroleum, wettability ($\theta$) expressed by the contact angle of hydrocarbon and water against the solid pore walls measured through the water phase, and lastly the radius (R) of the largest connected pore throats. Increasing the surface tension and decreasing the contact angle or pore radius will make the capillary force greater (Schowalter, 1979).

The resisting force is higher for gas than oil since the interfacial tension between gas and water ranges from 30-70dynes/cm and for oil it varies from 5-35dynes/cm, but the buoyancy force on the other hand is greater for the gas, levelling this out (Bjørlykke, 2010).

We have now seen that the pore size is vital for migration since it decreases the capillary force, but there is no use in having good porosity in a reservoir if there is no connection

between the pores allowing migration and accumulation possibilities. The permeability is the other important resisting "force" in the sub surface.

### 2.1.4 Darcy's law and Permeability

For hydrocarbons to migrate there have to exist some effective permeability, the pores have to be connected. Permeability relates to the fluids ability to move through porous media. The higher the permeability, the easier the fluid migrates through the rock (Selly & Sonnenberg, 2015). The absolute permeability (k) can be found using Darcy's law, which describes fluid flow through a porous medium (Bjørlykke, 2010; DAKE, 1978):

$$Q = \frac{kA(p_b - p_a)}{\mu L} \tag{3}$$

Where Q= volumetric flow rate, μ = viscosity, A=cross section area where migration occurs, ΔP=pressure difference over migration length L. Eq (3) assumes that the permeability is constant, this statement only applies for single-phase fluid flow with the exception of gas flow at low pressures or high flow rates.

Hydrocarbon migration on the other hand has to be considered multiple-phase flow. Two fluids, such as oil flowing together, each have their own effective permeability. Assuming that the flow is governed by Darcy's law, but that each parameter- pressure, viscosity and permeability, is related to each phase, the following equations are obtained:

$$u(w) = -\frac{kw}{\mu_w}\frac{dPw}{dx} \tag{3}$$

$$u(o) = -\frac{ko}{\mu_o}\frac{dPo}{dx} \tag{4}$$

Where $k_w(k_o)$ - effective permeability of the rock to water(oil), $P_w(P_o)$- pressure of water(oil), $\mu_w(\mu_o)$- viscosity of water(oil) (DAKE, 1978).

The sum of the effective permeabilities are always less than the absolute permeability and dependent on the fluid saturation. Figure 2.1-2 illustrates the saturation dependence.

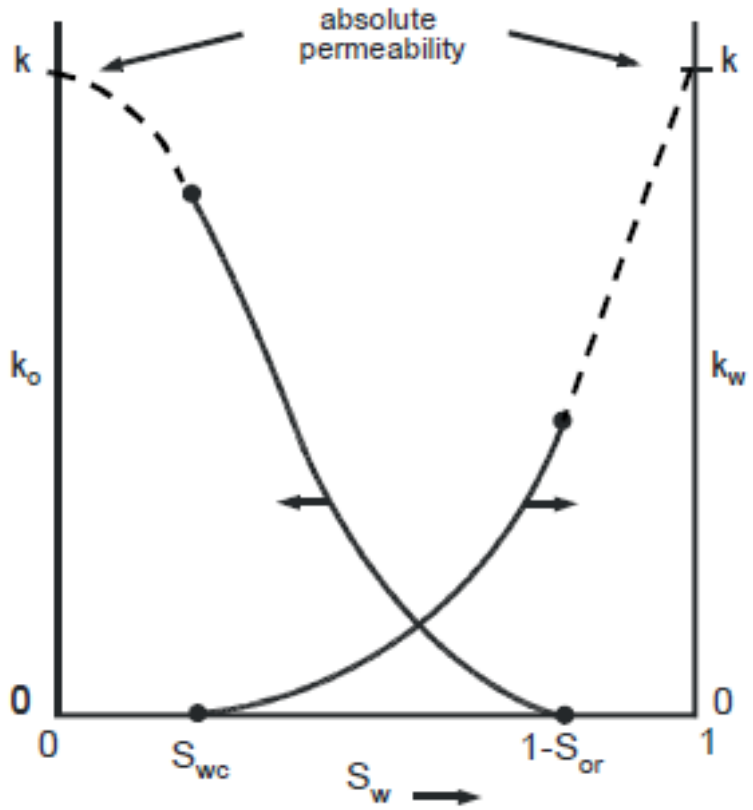


***Figure 2.1-2*** *K= absolute permeability of porous medium, Ko= effective permeability of porous medium to oil, Kw= effective permeability of porous medium to water, Sw= water saturation, Swc= irreducible water saturation, Sor= irreducible oil saturation. Looking at effective permeability curve for water; when Sw=Swc no water will flow and Kw=0. When Sw=1 rock is completely water saturated and Kw=K, absolute permeability. In between these values the effective permeability function follow the curve, where the shape depend on the wettability. Figure modified from (DAKE, 1978)*

## 2.2 Simple migration model

When the secondary migration starts, two main forces, the capillary and the hydrodynamic pressure gradient, drive the fluids, where the latter being of less importance. The main forces resisting the movement of hydrocarbons are the capillary forces and low permeability rocks.

Flow of hydrocarbons needs to be considered two- or three-phase flow, hence the relative permeability of oil, water and gas is key. If the saturation of the hydrocarbons is low, the capillary force will be greater than the buoyancy, hence the fluids will not migrate through the pore throats due to the relative permeability being low. Reservoirs are usually water-wet and have a low hydrocarbon saturation, meaning the grains are coated with a thin film of water that separates any hydrocarbons from the pore walls. This wettability condition will imbibe water and resist flow of hydrocarbons (Bjørlykke, 2010). Said shortly, if the driving force of an accumulation of fluids surpasses the resisting force of the barrier, hydrocarbons will imbibe the rock through the largest connected pores throats and displace the water (Schowalter, 1979).

### 2.2.1 Lateral and vertical migration

A simplified geological model can be useful as an example. Schowalter (1979) describes a laterally continuous homogeneous reservoir with a high-displacement-pressure seal underlain by a source rock. The hydrocarbons will start to accumulate at the resevoir boundary until the buoyancy force exceeds the capillary entry pressure. Furthermore, the hydrocarbon phase will then migrate vertically upward the reservoir until they meet the low permealibily seal, from here it will spread out along the boundary (Schowalter, 1979; Bjørlykke, 2010).

The height of a vertical oil column necessary to migrate updip through the resevoirs have been found to range from 1-10ft for sandstones, and 3-5ft for carbonate reservoirs. This height is reffered to as the critical vertical hydrocarbon height. These calculations have been made assuming water-wet reservoir rocks, interfacial tension of 30dynes/cm, hydrostatic conditions, and a buoyancy gradient of 0.1psi/ft. In the case of dipping carrier beds, the lateral length needed to reach the critical vertical hydrocarbon phase column depend on the degree of dip. The steeper the beds are positioned, the shorter the column need to be (Schowalter, 1979; Aschenbrenner & Achauer, 1960).

Once the critical length has been achieved the migration will carry on laterally updip through the reservoir along the path of least resistance. The hydrocarbons will mostly flow along the upper parts of the carrier beds, leaving the rest of the system barren. This is due to the buoyancy of the hydrocarbon phase in water. While migrating some of the oil droplets and gas bubbles at the base of the accumulation will be left behind as residual hydrocarbons, trapped in the capillaries. The gas and the soluable parts of the oil may then dissolve in the water and dissipate through diffusion (Verweij, 1993). Residual oil shows can be good indicators for migration pathways in exploration. Gas on the other hand, does not exhibit this behaviour due to its diffusive nature (Bjørlykke, 2010; Schowalter, 1979).

Migration in the carrier beds will continue as long as the loss of residual oil and gas through diffusion do not reduce the buoyancy force to less of that of the capillary pressure and there is a continuous supply of hydrocarbons down dip (Schowalter, 1979). The basics of secondary fluid migration are illustrated in Figure 2.3-1.

Vertical migration occurs when the resisting forces in the overlying seal are less than the driving forces. Fluids will migrate vertically through the seal until another barrier is reached.

Faults play a role in vertical and lateral migration (Section 2.2.3) by juxtapositioning of permeable carrier beds and migration along fault planes. Vertical fluid migration can often be identified on seismic data by gas chimneys and pipes (Selly & Sonnenberg, 2015; Løseth, et al., 2009). These features and other seismic identification of fluid flow will be presented in section 2.4.

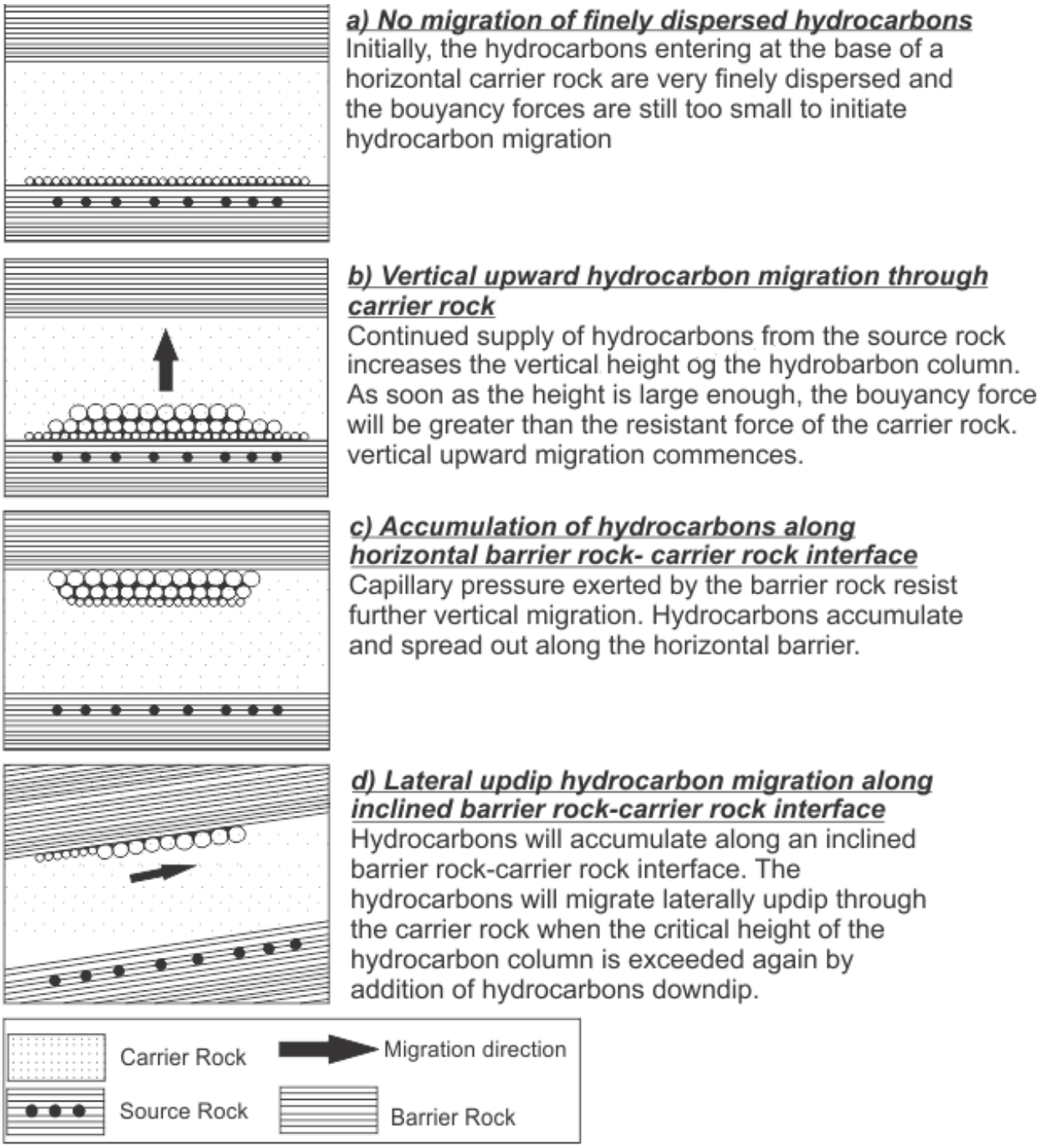


***Figure 2.2-1*** *Secondary separate phase migration under hydrostatic conditions. Figure modified from Verweij (1993).*

### 2.2.2 Trapping of hydrocarbons and tertiary migration

Migration will stop once the oil or gas is confined in a trap. There are many types of traps and the classifications varies between different authors. Generally, we can say that we have structural, diapiric, stratigraphic, hydrodynamic, and combination traps (Selly & Sonnenberg, 2015). We will not go further into detail describing the different types, assuming it is common knowledge for readers.

The important aspect of a trap related to migration is its capability to halt migration through an effective sealing caprock or displacement pressure barrier. All rocks may act as a seal as long as it is impermeable to hydrocarbon migration. Shales are the most common seals due to their fine-grained nature, producing high capillary pressures (Selly & Sonnenberg, 2015).

Assuming the critical vertical height of hydrocarbons in the caprock of a structural trap is less than the accumulation space available, hydrocarbons will migrate into the trap until it is filled to spill. If more hydrocarbons are added beyond the spill point, the trap will spill and the excess hydrocarbons will migrate further. If the capability of the seal is exceeded by the hydrocarbon column before filled to spill, oil and gas can leak vertically through the caprock and tertiary migration commences. Stratigraphic traps, as the one explained in the previous section, will fill until the hydrocarbons escapes at the flanks of the displacement-pressure barrier, or they can leak laterally updip through the barrier when the buoyancy force increases sufficiently to overcome the resisting force (Schowalter, 1979).

Permanent trapping of hydrocarbons relies on several factor, where the most important being a stable geological environment. Hydrodynamic gradients, change in dip, alteration of sealing caprock or lateral barrier and density variations of the fluids in the system can all contribute to tertiary migration. The soluble components of the hydrocarbons can be swept away in a hydrodynamic setting or dissipate through diffusion (Schowalter, 1979). Erosion and uplift can reduce the lithostatic pressure in the trap, altering the phase behavior of the fluids. Large amounts of gas can escape the oil and water and due to its high buoyancy, the gas will displace the other fluids out of the trap. Uplift and extension can lead to fracturing of the caprock, opening conduits where fluids can migrate. Overpressure may also fracture the caprock (Bjørlykke, 2010).The effect and importance of faults as migration pathways are discussed further in the Chapter 2.2.3.

#### 2.2.2.1 Tertiary migration mechanisms through caprock

The most common leakage mechanisms in consolidated sediments are fracture flow, Darcy flow, and diffusion. Fracture flow can take place in several ways, along fractures in fault, in hydro-fractures above overpressured reservoirs, along fractures induced by tectonic salt movement at the flanks or above domes, in fracture pipes, and in natural micro-fractures in rocks. This flow mechanism has high flow rates and can drain a hydrocarbon accumulation in a relatively short manner (Løseth, et al., 2009).

Diffusion and matrix flow on the other hand have low flow rates, and identification of such anomalies in seismic data could act as good indicators of hydrocarbons still being present in the trap (Løseth, et al., 2009). Figure 2.3-2 shows a schematic illustration of diffusion of gas through a water saturated caprock. Krooss & Laythaeuser (1996) state the conditions under which molecular transport should be considered a relevant tertiary migration mechanism:

1. *"Absence of volume flow (leakage) over extended periods of geological time,*
2. *tectonically stable areas, and*
3. *No further hydrocarbon supply from source rocks"*

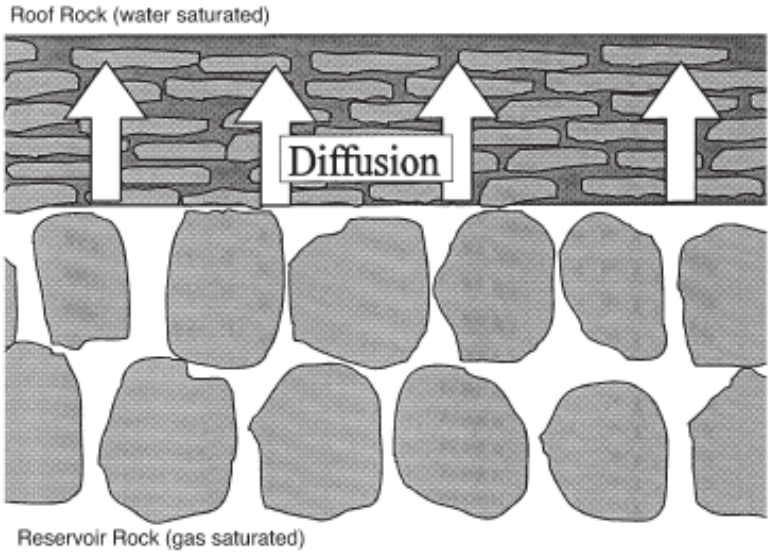


***Figure 2.2-2*** *Diffusion of gas through water saturated caprock. Illustration from Krooss & Laythaeuser, (1996).*

### 2.2.3 Migration along faults

Whether or not a fault can act as a conduit for fluid migration depends on the faults sealing capability. There is also an important distinction between migration along the fault plain and across it (Bjørlykke, 2010). Faulting may cause smearing of ductile clay or cement along the fault plane. This will act as a sealing mechanism, creating trap structures where fluids may migrate into and accumulate (Egholm, et al., 2008; Selly & Sonnenberg, 2015), thereby restricting migration.

Faulting, folding and fracturing are common responses to stress in sedimentary rocks. Reasons for the stress are often related to basement involved tectonic activity. The fault created by the stress may connect numerous fractures, increasing permeability and initiating fracture flow along the fault. Hence, fault zones may act as vertical fluid conduits (Løseth, et al., 2009).The faulting also initiate lateral migration when permeable carrier beds are juxtaposed (Selly & Sonnenberg, 2015).

Polygonal faults are non-tectonic fault located within sedimentary layers. The formation of polygonal faults relates to sediment compaction and fluid expulsion. Pipe structures are often found at the termination of these fault systems, indicating that such systems act as pathways for fluid migration (Berndt, et al., 2003; Berndt, 2005).

A basic understanding of the dynamics governing secondary and tertiary migration has now been achieved, and a simple migration model presented. For this thesis, identification of fluid flow features in seismic data is important, and the following section will describe the seismic characteristics of such features.

## 2.3 Indications of hydrocarbons in seismic data

When hydrocarbons are present, or have previously been present in sediment pore space, it will be recognisable in seismic data in a variety of ways. Hydrocarbons will normally reduce the seismic compressional p-wave velocity ($V_p$), (Figure 2.4-1), and since the appearance of seismic reflectors partially relies on velocity it will have an effect. Gas will also decrease the density to some extent. The most common types of hydrocarbon indicators are amplitude anomalies, flat spots, velocity effects, polarity/phase reversal, and other effects such as loss of frequency (Andreassen, 2009).

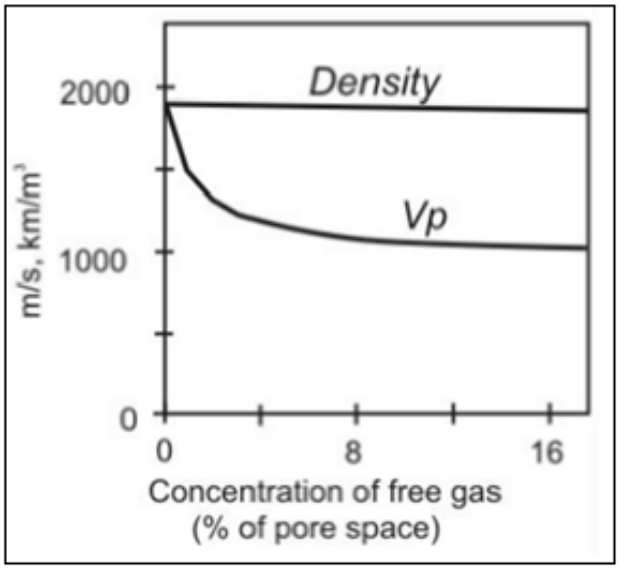


***Figure 2.3-1*** *Illustration showing how free gas will reduce the P-wave velocity and density. Y-axis indicates velocity, x-axis concentration of gas. The graph is given as a function of gas saturation for sediments with porosity 0.4 and Vp=1900m/s. (Andreassen, 2009)*

Amplitude anomalies are divided into two groups. Bright spots that refer to reflectors of anomalously high amplitudes, and dim spots, which relates to anomalously low amplitude. If the sediment pore-space is occupied by gas, the compressional velocity will noticeably reduce. This reduction leads to a negative acoustic impedance contrast. If the contrast is high, the amplitude anomaly from the top of the gas column is known as a bright spot and will appear as a trough in the wiggle trace plot. The interface between the gas-phase and the water-phase, the gas water contact (GWC), will produce a reflection called a flat spot, a positive impedance contrast marking the density difference between the two phases. This contact will normally be horizontal in depth, but may differ in seismic data due to velocity effects (Andreassen, 2009; Løseth, et al., 2009).

Velocity effects occur due to the reduction or increase in Vp velocity. If the gas column is sufficiently thick, a pull-down of the underlying reflectors can be seen. Since the gas decreases the velocity, the waves use longer time to reach the reflectors directly below the gas zone than they would otherwise do if the sediment was water filled. Hence the reflectors will be interpreted to be deeper positioned, and a down-bending trend takes place (Andreassen,

2009). The opposite is true when dealing with high velocity/high density regions, resulting in pull-up effects (Løseth, et al., 2009).

Phase reversal refers to an 180 degree phase shift along a continuous reflector, which is common for gas-oil and gas-water contacts. The top-reservoir bright spot reflection could also reveal a phase reversal (Andreassen, 2009). Figure 2.4-2 shows how a bright spot, dim spot, phase reversal and flat spot may appear in seismic data.

The hydrocarbon indicators mentioned above are the most common ones, but the effect from frequency loss and diffraction should also be stated. Beneath bright spots in the gas bearing sediments, seismic propagating energy is being absorbed at a greater extent than in the water-filled parts. This absorption depletes the seismic signal of the high frequencies. Diffraction at the flanks of the gas column occurs when the lateral contrast in acoustic impedance is significant, particularly at the ends of bright spots. This will make non-migrated seismic data more difficult to interpret.

The characteristics of hydrocarbon accumulations are usually used to identify gas. Oil on the other hand is not that easy to recognize. This is due to the low density difference between oil and water not creating a significant acoustic impedance contrast (Andreassen, 2009). Other seismic indications of gas bearing sediments are acoustic masking/blanking and acoustic chaotic reflections. Gas in sediments will give rise to low velocity zones that distorts and disturbs the seismic reflectivity due to absorption of acoustic energy at the top of the gas bearing sediments. In some cases, the reflections might be completely absent, and this effect is known as acoustic masking. Chaotic reflections zones are areas in seismic data where the reflections are chaotic compared to adjacent areas. This is often the case for areas where gas migrate through hydraulic fractures (Andreassen, 2009; Løseth, et al., 2009).

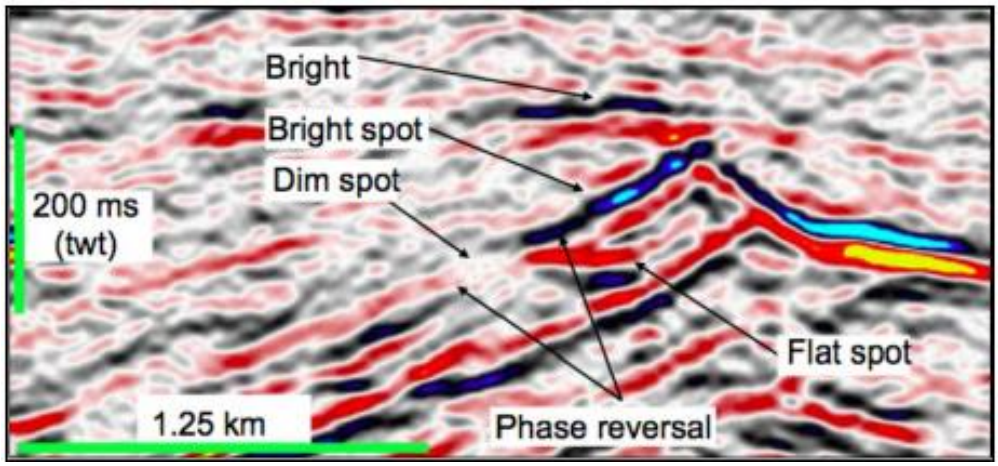


***Figure 2.3-2*** *seismic section showing bright spot, dim spot, flat spot and phase reversal. From (Løseth, et al., 2009)*

## 2.3.1 Seismic fluid flow expression

When fluids migrate through the sediments, changes in the seismic expression can be recognized. This section of the thesis will describe and illustrate leakage anomalies in seismic data.

### 2.3.1.1 Gas chimneys and pipes

Gas chimneys are vertical/subvertical zones of acoustic masking representing a subsurface leakage of gas from a fractured caprock. The shape of the chimney can vary from well-defined vertical pipes to diffuse shadows. Not all zones of acoustic masking can be identified as gas chimneys, as there has to be some collaborating evidence that the anomaly is caused by gas leakage. Therefore, it is normal to look for other indicators of gas. Bright spots and velocity pull downs are usually observed at respectively the top and base of the chimneys (Løseth, et al., 2009; Andreassen, 2009).

Acoustic pipes are types of gas chimneys resulting from short-lived violent gas blowouts. Pipes appear as narrow vertical columns of acoustic masking which may display stacked amplitude anomalies (Figure 2.4-3). In seismic time slices pipes are identifiable as narrow circular zones of disturbed seismic reflectors (Løseth, et al., 2009). Acoustic pipes are one of the seal bypass system groups described by Cartwright, et al (2007). The author distinguishes between four different types of pipes based on the contextual setting; dissolution pipes, hydrothermal pipes, blowout pipes and seepage pipes.

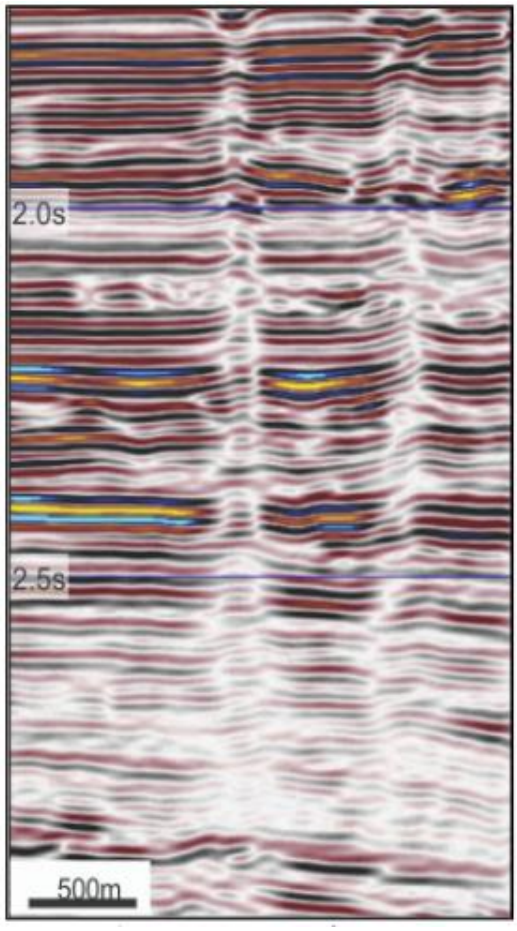


**Figure 2.3-3** Seismic appearance of acoustic pipe with stacked amplitude anomalies. Modified from *(Løseth, et al., 2011)*

Dissolution pipes forms from the dissolution of rocks in the subsurface, creating cavities. This sets up an instability, which may lead to collapse of the sediments. Formation of dissolution pipes can lead to overburden collapse and set up vertical migration

pathways for fluids. The leakage zone is characterised by intense faulting, fracturing and sagging. The rate of formation is controlled by the degree of solution, which may be gradual or rapid. Dissolution pipes are common for areas of evaporite and karst (Cartwright, et al., 2007).

Hydrothermal pipes are migration conduits that form by the release of high-flux hydrothermal fluids. These are often related to fluids coming into contact with igneous intrusions, and can be expected to be found in any basin with mafic sills or dikes. When these intrusion crosses sealing sequences it can significantly enhance the vertical migration. In seismic data the pipes can be recognised by columnar inward-dipping disturbed/collapsed reflections, and their location directly above igneous intrusions can also aid in identifying the feature. The dimension of the hydrothermal pipes varies dramatically. Diameters can range from 100-3000m, and heights from 100m-2500m (Cartwright, et al., 2007).

Blowout pipes show the same characteristic in seismic data as the pipes already discussed, but can be distinguished by their upward termination at surface or as paleo pockmarks. In addition, their formation also differs from the other acoustic pipes. Blowout pipes is not connected to sill intrusions or areas of evaporite and karst, but have been interpreted to form when overpressured reservoir leaks (Cartwright, et al., 2007).

The last of the pipe types discussed by Cartwright et al., (2007) is the seepage pipes. These pipes have comparable seismic expressions to that of blowout pipes, but lack the pockmark craters triggered by the violent fluid expulsion. The geological setting in which seepage pipes form is also silimar to blowout pipes, as they can be found at the crest of gas reservoirs and at the lateral margin of aquifers. However, the physical properties of the host rock in which seepage occurs are generally sand and silt dominated, wheras blowout pipes form in fine-grained sealing sequences where fluid pressure builds up.

#### 2.3.1.2 Faults

Faults are the largest group of the seal bypass systems, and the relation between faults and migration has been explained in section 2.2.3. This section will only describe their appearance in seismic data. Generally, for faults to be seismically recoverable, the throw has to be greater than 10m (Cartwright, et al., 2007). The fault will appear as vertical seismic discontinuities. If the fault is acting as a conduit for fluid migration, the seismic expression can alter. High

amplitude anomalies above the fault plane, or in the carrier beds besides the fault, can be observed, implying fluid migration through the fault or into permeable layers adjacent to the fault. If the fault extends to the surface or near to it, surface expressions can be recognized (Løseth, et al., 2009; Vadakkepuliyambatta, et al., 2013). These features will be explained in the following section. Cartwright et al., (2007) subdivide the SBS group into two families based on whether the fault is confined within a sealing sequence, or whether the fault acts as a trap laterally limiting fluid flow. Both families will show amplitude anomalies distributed within the fault system indicating gas accumulations.

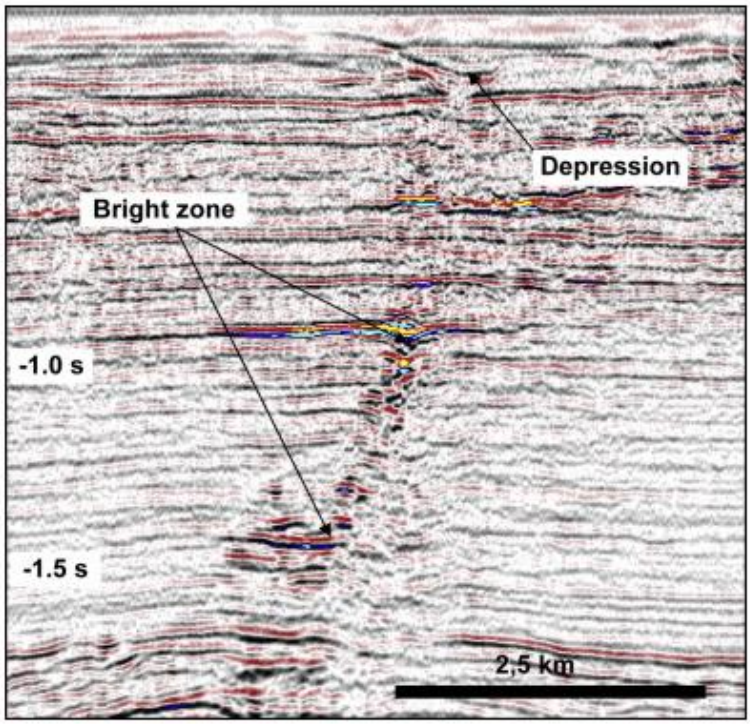


**Figure 2.3-4** Seismic expression of fault where gas is migrating along the fault plane. Bright anomalies represent gas migrating into permeable beds along the fault. Figure from *(Løseth, et al., 2009)*

#### 2.3.1.3 Surface expression

When hydrocarbons reach the surface they can create different structures such as pockmarks, sand or mud volcanoes, diapirs, and carbonate build-ups (Løseth, et al., 2009). Pockmarks are depressions in the seabed where fluids, most often gas, have escaped and removed the overlying seabed sediments. The depression are shallow and range from a few meters to tens of meters in depth. The diameters vary to a great extent from just a few meters, up to several hundreds of meters. Pockmarks are generally created in soft, fine-grained sediments and have a circular shape. Pockmarks may also merge into each other along strings when located above fault planes (Judd & Hovland, 1992; Løseth, et al., 2009). In seismic data, pockmarks can be located above vertical zones of acoustic masking such as pipes and chimneys (Løseth, et al., 2009).

#### 2.3.1.4 Intrusions

Intrusions are the last of the main seal bypass system groups. Intrusions can breach the sealing sequence in three ways. The first is by puncturing the seal, allowing fluids to flow along with the intrusive material through the seal. Formation of mud volcanoes exhibit this behaviour and will appear as cylindrical conduits with amplitude anomalies within the intrusion, and adjacent to it, in seismic data. The second is when the intrusive material has a lower permeability than the seal. The intrusion will hence act as a conduit due to its lower resisting forces, and this mechanism is often related to sand intrusions in shales. In seismic data these intrusion occur as discordant amplitude anomalies. The third and last way in which intrusions breach the seal is through intense fracturing and deformation of the sealing sequence. This will enhance the permeability in certain areas, permitting secondary migration. Deformation and fracturing is common for salt diapirs and igneous intrusions, where the latter often can be seen in seismic data in relation to hydrothermal pipes (Cartwright, et al., 2007).

## 2.4 Gas hydrate formation and stability zone

Gas clathrates, or more commonly hydrates, are ice/snow-like material consisting of small gas molecules trapped within voids in a water-structure lattice (Figure 2.5-1 and 2.5-2).

***Figure 2.4-1*** *Gas hydrates from the Gulf of Mexico. From (Winters & Lorenson, 2002)*

Several gas molecules have the appropriate size to form hydrates but the most abundant hydrates in marine settings are the methane hydrates. Hydrates formation is restricted to the shallow geosphere, and can be found as pure hydrate nodules, as cement within pore space, as lamina, and in form of veins. (Andreassen, 2009; Kvenvolden, 1998; Sloan, 1998).

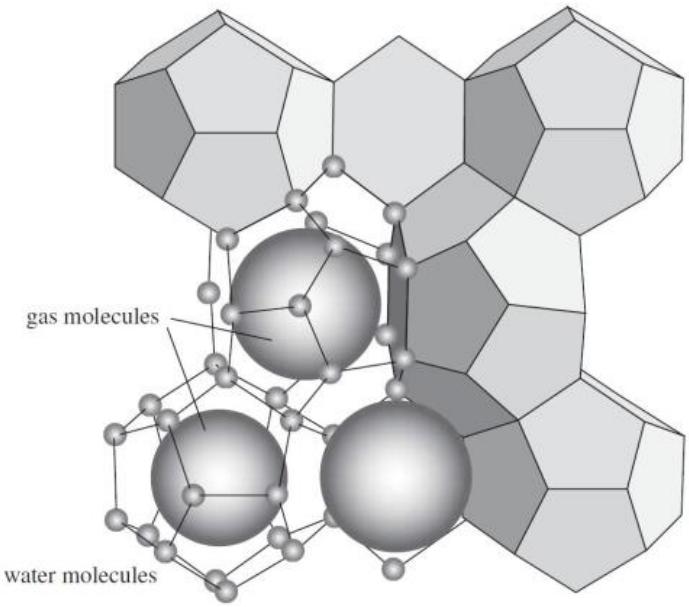


***Figure 2.4-2*** *Sketch showing a typical gas hydrate structure where water molecules trap gas molecules, such as methane, in the voids. From (Maslin, et al., 2010).*

The maximum amount of methane confined in the hydrates are controlled by the clathrate geometry. For a fully saturated structure I methane clathrate, $1m^3$ of methane hydrate is equivalent to $164m^3$ of gas and $0.8m^3$ of water at STP. Thus, gas hydrates can contain more gas per unit volume than free gas would occupy, making hydrates important as a potential energy resource, as well as a geohazard and a climate threat (Kvenvolden, 1998; Max & Johnson, 2014).

Formation of hydrates is dependent on temperature, pressure and composition. Low temperature and/or high pressure create environments for stable hydrates. There also needs to be a large supply of gas molecules due to the low solubility of methane in seawater. These requirements limits the regions on Earth where hydrates are found in the ocean floor sediments at depths greater than approximately 500m, and polar regions associated with permafrost (Kvenvolden, 1998).

Given that these factors are met, hydrates may form within the gas hydrate stability zone (GHZS) illustrated in Figure 2.5-3, showing the phase diagram. The GHSZ is a relatively narrow zone situated approximately parallel to the seabed/terrestrial surface (Max, 2003). The thickness of the GHSZ is determined by the composition of the gas and the water, hydrostatic

pressure gradient, bottom water temperature, and the geothermal gradient (Sloan & Koh, 2008), typically increasing with water depth due to pressure buildup (Max & Johnson, 2014).

The lower boundary of the GHSZ is often marked by a strong negative impedance contrast.

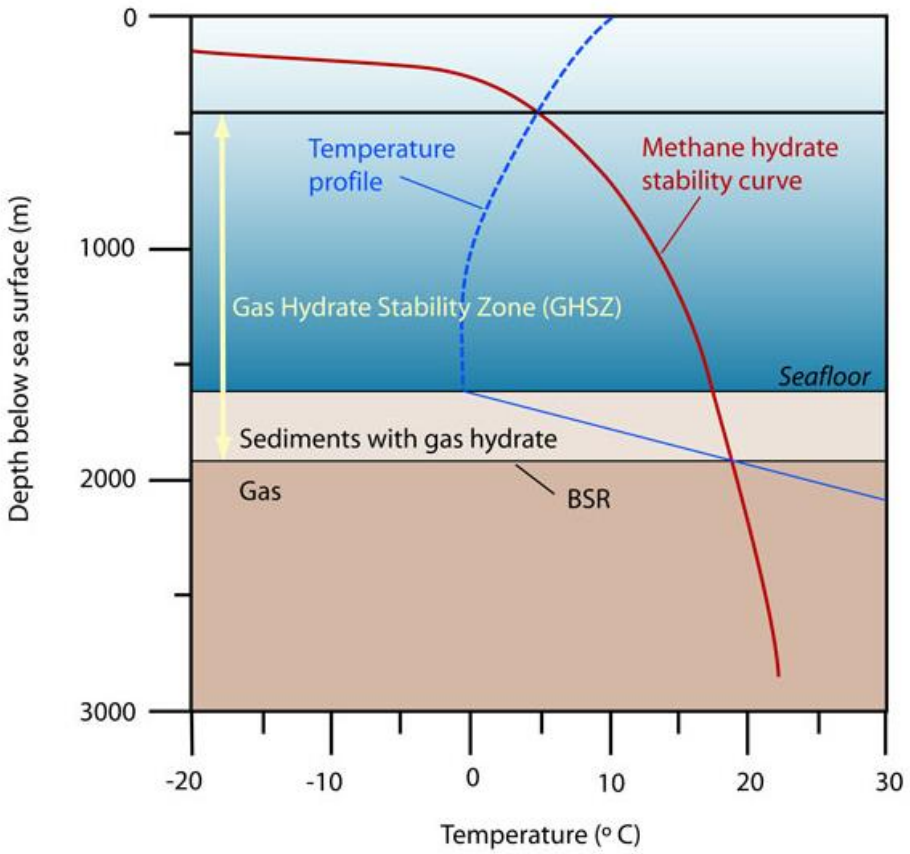


***Figure 2.4-3*** *Conceptual model showing the GHSZ in Polar Regions with geothermal gradient of 50°C/km. Collected from [http://archive.noc.ac.uk/IPY/background.html](http://archive.noc.ac.uk/IPY/background.html) (modified from (Chand & Minshull, 2003) ).*

Due to the fact that the composition of gas and fluids change little with depth, and that the fluid pressure profile is close to hydrostatic, the boundary will follow iso-temperature lines, resulting in a reflection parallel to the seafloor. This boundary is known as the bottom simulation reflector (BSR) (Andreassen, 2009; Clennell, et al., 1999). There is some disagreement regarding the conditions that produce the BSR. One theory is that the negative impedance contrast is due to the presence of low velocity free gas beneath the hydrate stability zone while other argue that the boundary arise from the transition zone from a high velocity hydrate layer and lower velocity sediments underneath (Clennell, et al., 1999).

The BSR is dynamic and will move vertically to maintain the thermodynamic balance. In the case of increased sedimentation, geological uplift, lowering of the sea level, or seafloor warming, the BSR will move upwards. When the BSR migrates up, hydrates beneath the GHSZ will begin to dissociate, possibly creating an overpressure at the BSR. This overpressured gas can drive pore water and has the potential to vent or cause blowouts of gas and water masses to the seafloor (Max & Johnson, 2014).

The Barents Sea water depth is on average 230m, but during the last glacial period it was approximately 120m less. This makes it unlikely that the gas hydrates is related to permafrost, but rather migrating of deeper thermogenic gases. During the late Cenozoic the Barents Sea shelf underwent much erosion due to glacial advances. Laberg (1998) suggests that this erosion may have led to increased gas leakage from deeper reservoirs, enabling hydrate formation. Glacial erosion could also contribute to a thicker GHSZ due to seafloor subsidence and sediment removal (Laberg, et al., 1998).

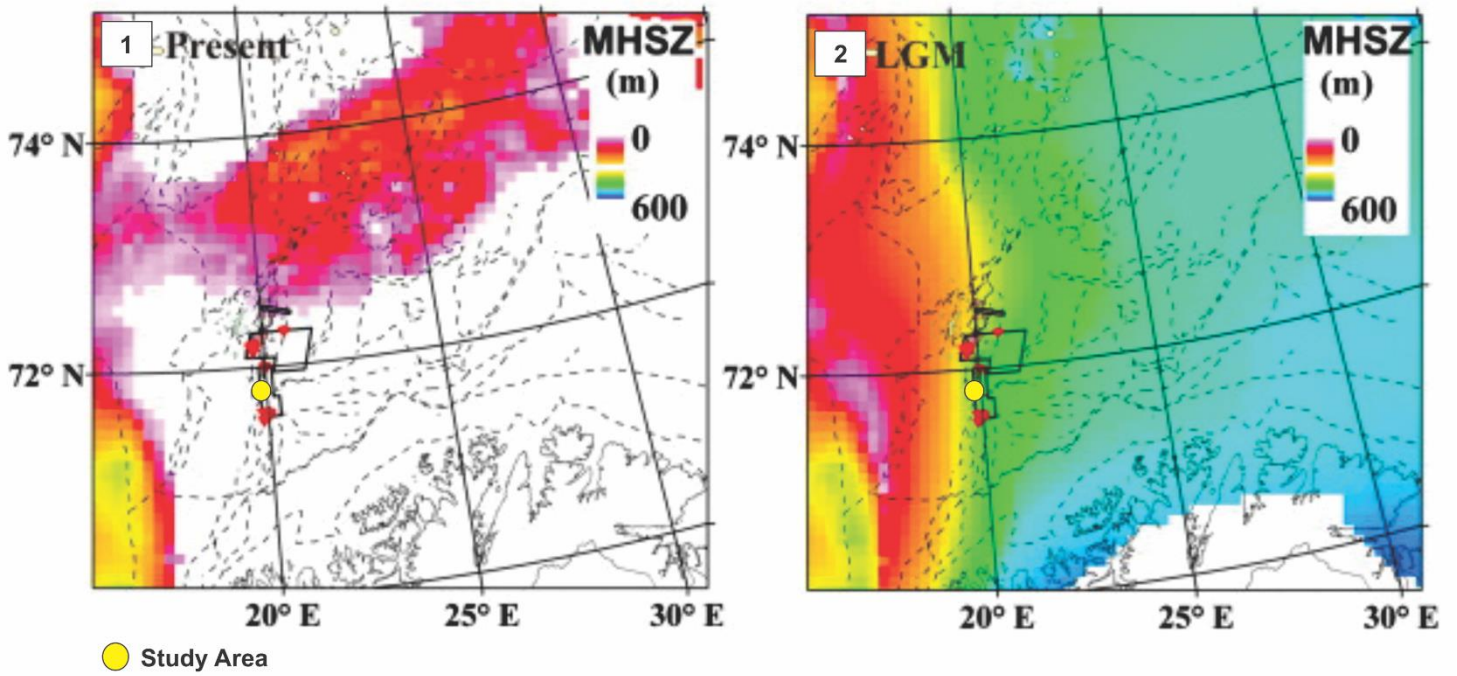


***Figure 2.4-4*** *Map showing 1) present day and 2) LGM thickness of methane hydrate stability zone (MHSZ) for the SW Barents Sea. Location of study area for this thesis is marked by yellow circle. Modified from (Chand, et al., 2012).*

Based on modelling of GHSZ in the SW Barents Sea the present thickness has been found to vary between 0-250m below the seafloor, rendering much of SW Barents Sea free of hydrates (Figure 2.5-4). In comparison, during the last glacial maximum (LGM) when an

approximately 1200m thick ice cap covered the area, the GHSZ was up to 600m below the present day seafloor (Chand, et al., 2008; Chand, et al., 2012).

## 2.5 Glacial erosion and glaciotectonic landforms

### 2.5.1 Glacial erosion

Glacial erosion give rise to characteristic forms and landforms that can tell us something about the past glacial environment. This chapter introduces some of the most common erosional features and glaciotectonic landforms.

Benn & Evans (2010) classify the erosional forms by scale, from small-scale forms to landscapes of glacial erosion. For this thesis, the intermediate-scale forms are of interest. Intermediate-scale forms comprise bedforms, depressions and channels. These forms are small compared to the ice flow unit making them, and reflect the relationship between geology, topography, and ice and water flow. Typical intermediate-scale erosional forms are roches moutonées, whale-backs and rock drumlins, crag and tails, and channels, where the latter being the focus for this chapter.

Nye channels (subglacial channels) are distinctive erosional features resulting from subglacial drainage, typically ranging from tens to thousands of meters in length, and up to a few tens of meters wide. Nye channels occur as dendritic networks, or as isolated features aligned parallel to ice flow direction. Tunnel *valleys* or *channels* (Figure 2.6-1) are deep channels cut into bedrock or sediments. They are much larger than Nye channels, and can get >1000km long and 4km wide. Furthermore, they occur as isolated features, or in anastomosing and dendritic systems. Tunnel valley are products of subglacial meltwater flowing under pressure and are characterised by wide and relatively flat bottoms and steep sides, often terminating in huge moraines. Eroded tunnel valleys may be entirely filled by glacial deposits, non-glacial deposits or sedimentary successions making them free of any surface expression, hence geophysical data is needed to study them (Benn & Evans, 2010).

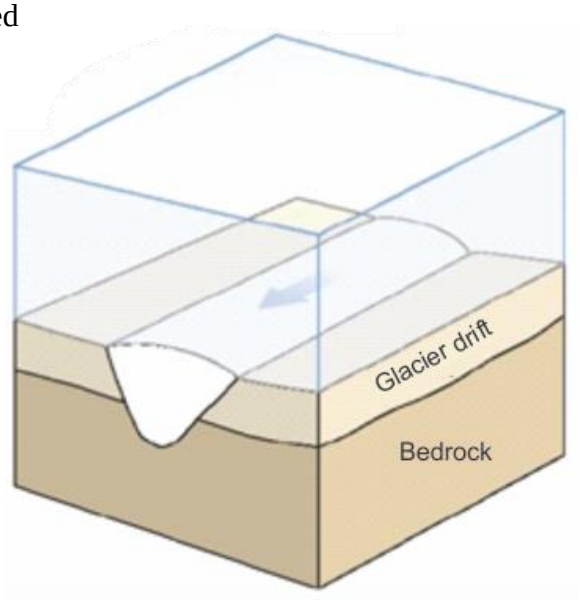


***Figure 2.5-1*** *Illustration of initial formation of a tunnel valley. From (Benn & Evans, 2010)*

### 2.5.2 Glacitectonic landforms

*''Glacitectonic landforms are the surface or morphologic expressions of subsurface structures resulting from glacial deformation of bedrock and glaciogenic strata''* (Aber & Ber, 2007).

This chapter will discuss some of the landforms related to the proglacial and sub-marginal areas of a moving glacier, mega-scale glacial lineations (MSGL), and the mechanics of glacitectonism. Benn & Evans (2010) classify the landforms using a fourfold scheme: 1) hill-hole pairs; 2) Composite ridges and thrust moraines; 3) cupola hills; and 4) mega-blocks and rafts (Figure 2.6-2).

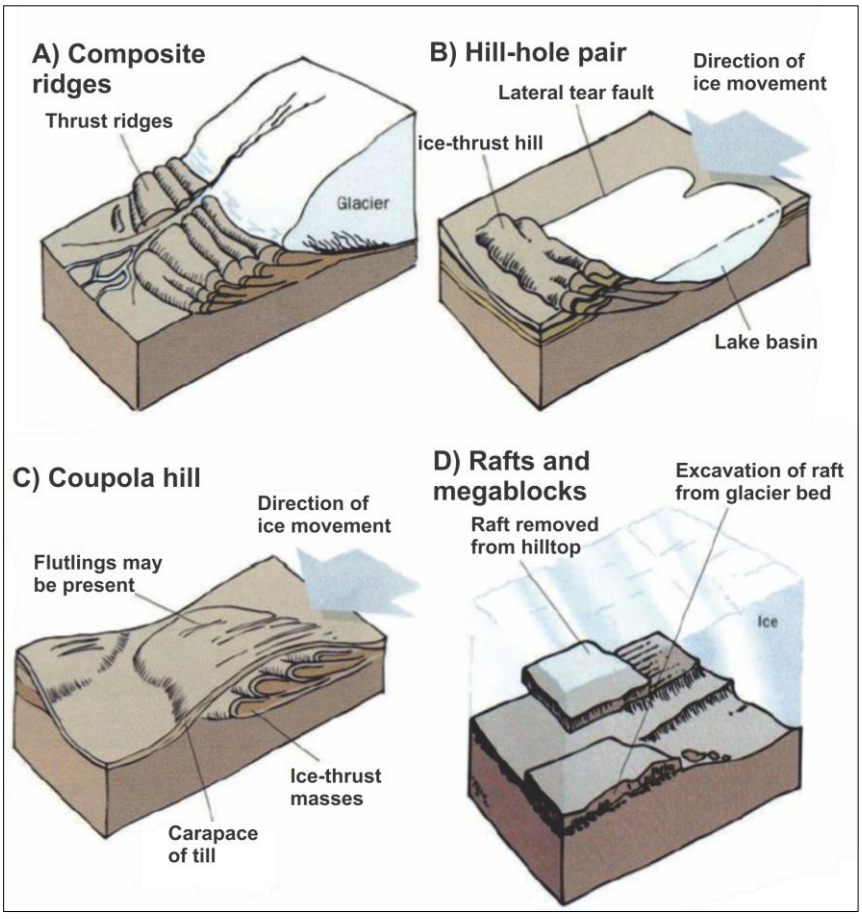


***Figure 2.5-2*** *Illustration of the four main glacitectonic landforms and their characteristics. See text for description of landform A),B), and D). Modified from (Benn & Evans, 2010)*

The expressions raft, megablock, scale and floe are all used to describe individual masses of dislocated bedrock and sediments making up ice-shoved hills. Rafts and megablocks are large, relatively thin bodies of sediments lying in more or less horizontal positions. The term floe describe any deformed and dislocated mass, and scales are thrust blocks in an imbricated or overlapping position (Aber & Ber, 2007).

A hill-hole pair consist of an ice-trust hill and a similar looking source depression. The ice-thrust hills are often located within short distance from the source depression, but they can be found up to a 5 km distance away from the depression. The source depressions may be infilled by sediments, limiting their surface expression. Glacitectonic depressions can also be found without any downglacier ice-thrust hill due to comprehensive subglacial erosion. Hill-hole pairs are characterized by 1) crescentic or arcuate shape, concave upglacier, 2) asymmetric cross profile with steep slopes and the highest point at the downglacier end, 3) series of traverse sub-parallel depressions and ridges. The pairs can cover an area of <1 to >100km$^{2,}$ and reach heights from 20 to 200m (Aber & Ber, 2007; Benn & Evans, 2010).

Composite ridges (thrust-block moraines) are the most common glacitectonic landform. They form where glacitectonic processes excavate and elevate proglacial material. They consist of napped or imbricated slices of up-thrust and distorted bedrock and sediments, often overlain and interlayered with glacifluvial and glacigenic materials. Small composite ridges vary in height from 20m to >100m, and cover an area of 1 to 100km$^2$, whereas large composite ridges vary respectively between 100-200m and 20 to >100km$^2$. The location of composite ridges are good indications of glacier position at stillstands or readvances (Benn & Evans, 2010).

MSGL are large streamlined ridge-groove features parallel to ice movement, which can get up to 100km long. Based on their distribution they are inferred to be a result from fast flowing ice streams or surges, and a product of sub glacial soft sediment deformation (Ottesen, et al., 2005; Andreassen, et al., 2008; Winsborrow, et al., 2009; Clark, et al., 2003).

Proglacial glacitectonic is defines as large-scale displacement of proglacial and sub-marginal sediments by glacier ice induced stress, involving ductile or brittle deformation, or a combination of the two. However, frozen sediments are much more prone to the latter. Brittle deformation will often result in thrusting of blocks along a basal failure plane. The mechanisms affecting failure and brittle deformation within sediments are temperature,

applied stress, strain rate, and pore-water pressure. Pore-water pressure at the glacial margin may be enhanced due to proglacial permafrost confining unfrozen water in underlying aquifers and impermeable sediments. Gas hydrates can also create a high pore-water pressure (Benn & Evans, 2010; Windsborrow, et al., 2016).

# 3 Study area

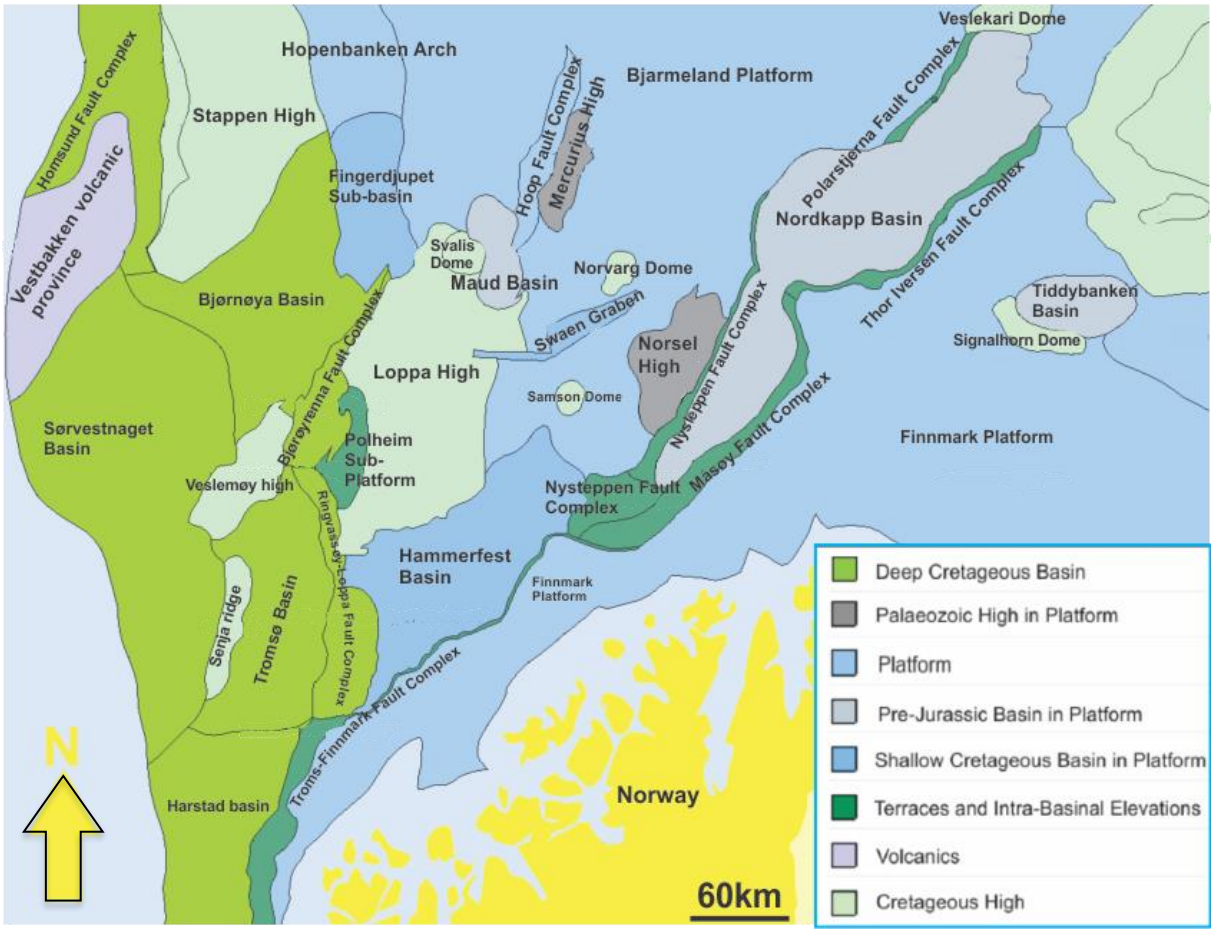


***Figure 3-1*** *Structural elements of the SW Barents Sea. Figure modified from NPD Fact Maps 2016.*

The greater Barents Sea is delimited by the shelf area between Norway and Svalbard in the west, and between Franz Joseph land and Russia to the east. Novaya Zemlya marks the eastern limit and the deep Norwegian Sea defines the western boundary (Henriksen, et al., 2011). The southern Barents Sea are separated into five main structural elements, the Hammerfest Basin, the Nordkapp Basin, the Finnmark and Bjarmeland Platforms, and the Loppa High. Several smaller structures delimits the main elements, these include the Troms-Finnmark, Ringvassøy-Loppa, Bjørøyrenna, Måsøy, Nysleppen and Asterias Fault Complexes (Figure 3-1) (Halland, et al., 2016).

## 3.1 Development of the SW Barents Sea

The basins in the western Barents Sea are characterized by thick Palaeozoic-Early Cretaceous strata (Figure 3.2-1). The westernmost areas towards the margin have thick units of Paleogene-Neogene deposits, differentiating them from the eastern areas on the shelf where Palaeozoic and Mesozoic deposits are located in major depocentres within the basins (Henriksen, et al., 2011).

During the Caledonian Orogeny in the region of the western Barents Sea, the Iapetus Ocean, which previously separated Eurasia from Laurentia, closed before deformation in the Middle Ordovician started. The deformation was at its peak in the Silurian. In the Late Palaeozoic half grabens developed due to crustal extension, and sag basins were formed in large parts of the Barents shelf. Succeeding uplift in the Uralide Orogeny, during the Devonian and Carboniferous-Permian plate collision, noticeable changed the basins to the east in late Palaeozoic to Early Triassic time. Later Post-Permian subsidence was concentrated to the eastern basins towards the Novaya Zemlya, although some subsidence occurred in the Nordkapp Basin. The Hammerfest Basin also formed a Post-Permian depocentre to the west. This top Permian surface slopes upwards to the northwest, where it ultimately outcrops on Svalbard (Henriksen, et al., 2011).

Whereas extensional rifting previously was dominant in the eastern region, a westward shift happened during the Middle to Late Jurassic. This rifting can be seen in the Hammerfest basin and the areas toward the western border. In addition, following subsidence in the Cretaceous is also primarily focused to this region. Moving further west to the region of the Sørvestnaget Basin and Vestbakken Volcanic Province, Cenozoic subsidence dominates (Henriksen, et al., 2011). The major Paleogene tectonism and uplift followed by Paleogene and Neogene erosion is an essential geological aspect of the Barents Sea. This tectonism is probably related to the Early Eocene onset of seafloor spreading of the Atlantic and Arctic Oceans. The erosion of most impact took place in the Quaternary due to the glacial settings (Halland, et al., 2016; Henriksen, et al., 2011).

## 3.2 Stratigraphy and environments

### 3.2.1 Mesozoic

Due to a significant hiatus in the late Permian, the Permian-Triassic transition is poorly understood (Worsley, 2008). Sediments from the Uralian highlands in the east, the Fennoscandian Shield in the south, and the uplifted Novaya Zembla were the main sediment sources in the early Triassic. In the eastern part of the Barents Shelf an alluvial plain developed, and in the N and NE of the Finnmark Platform a series of shelf margin progradations are recorded. The western Barents Sea region was during Triassic times characterized by little tectonic activity and passive subsidence. There was however, active faults along the western margin, and uplift and erosion of the Loppa High may have formed local sediment transport systems if exposed (Smelror, et al., 2009). Due to the non-siliceous fine clastics depositions, the timespan has been referred to as the "Early Triassic silica gap" (Worsley, 2008). During Mid-Triassic times, organic-rich mudstones accumulated in anoxic basins in the west, and non-marine deposits were replaced by near-shore sediments in the eastern region. Sediments in the southwestern shelf area where shed from Fennoscandian Shield and the Urals and deposited along a NE-SW trending coastline. Late Triassic times were characterized by extensive uplift and erosion in the eastern Barents Sea-Kara Sea region. This steered a westward costal progradation, developing continental and coastal-plains, and by Late Triassic- Early Jurassic times the Barents Sea shelf area comprised wide continental lowlands. Only smaller areas in the west had shallow marine environments (Smelror, et al., 2009).

In the late Early Jurassic, due to global sea-level rise, an extensive coastal plain transgression commenced, establishing shallow-marine environments in the eastern and western regions of the Barents Sea shelf (Smelror, et al., 2009). Depositional systems and structural regimes altered, and sedimentation rates and subsidence decreased dramatically compared to those in earlier Triassic times. The progradational systems from the Uralian highlands were no longer dominant in the western areas (Worsley, 2008). During the Middle Jurassic, regression reached its maximum at this time, and large parts of the central Barents shelf area was exposed, leaving marine environments only in the eastern and western areas and a possible seaway connecting them in the south. Due to the uplift, following erosion and winnowing of the central areas of the shelf, much of the Middle Jurassic sediments are absent in the western and central Barents Sea region. Late Jurassic transgression reached its maximum in the Tithonian creating an open marine shelf dominated by mudstones and shales deposited in

shallow to deep marine environments. High organic productivity and low sedimentation rates led to significant organic rich bottom sediments. Due to the Cimmerian movements, further uplift of the Loppa High and the Stappen High began, and uplift and following erosion of the Sentralbanken high, the Hopen High and the Hjalmar Johnsen Dome have been recorded (Worsley, 2008; Smelror, et al., 2009).

During Late Jurassic-Early Cretaceous sea level lowered. Regression continued during the Early Cretaceous, developing a more open marine environment (Worsley, 2008). Opening of the Amerasian Basin in the Arctic Ocean led to uplift and tilting of the northern shelf area, which again led to increased northern sediment supply. In the southwestern shelf region, thick units of clay deposits with thin layers of dolomite and limestone were deposited in the deep basins (i.e., Knurr and Kolje formations). Downflank of the Loppa High, thick sandy sub-marine fans were deposited. In the late Early Cretaceous, the Barents Sea consisted of marine shelves in the western and central parts and uplifted land in the north-eastern part, hence sediment prograded from NE to the beep basins in west (i.e., The Tromsø Basin). Thick Aptian-Albian sediment successions consisting of shale, siltstone and sandstone are found here (i.e., The Kolmule Formation) (Smelror, et al., 2009). Uplift of the northern shelf area and erosion continued during the Late Cretaceous and the only place of significant deposition occurred in the western basins (Worsley, 2008).

### 3.2.2 Cenozoic

During the Paleogene, the Barents Sea shelf development was characterized by tectonic activity along the western margin until the final opening of the Norwegian-Greenland Sea in the Eocene (Worsley, 2008). As a result of the opening of the Norwegian-Greenland Sea the northern and eastern parts of the shelf were uplifted, however the westernmost basins still were subsiding, and hence became clastic depocenters for the newly uplifted areas during Eocene times. Eocene sediments differ from the grey to olive-colored claystones of Paleocene times. The Eocene record show episodes of a significantly more active clastic deposition environment, with blocky sandstones originating from gravity flows. The Cenozoic succession is however absent in several areas on the shelf as on the Loppa High, the Finnmark and Bjarmeland platform, and in the northern Barents Sea region (Smelror, et al., 2009).

In Neogene times, the Barents Sea shelf underwent several glaciations resulting in subsidence when ice covered, and uplift during ice retreat. Findings from a previous study indicate that the ice-sheet reached the shelf edge at least 5 times during the Late Pliocene-Pleistocene (Faleide, et al., 1993). Sediments were deposited along the western shelf margin in major submarine depocenters (Worsley, 2008), and the southwestern shelf margin prograded 30-40 km westward during the Pliocene-Pleistocene (Andreassen, et al., 2007). In the southwestern part of the Barents Sea, substantial large amounts of glacigenic sediments are found in the Bjørnøyrenna trough mouth fan (Smelror, et al., 2009).

The late westward prograding Cenozoic succession has been divided in to three sediment packages (GI-GIII), consisting of seven regional reflectors (R1-R7) at the Barents Sea shelf margin. The lowermost reflector, R7, has been interpreted to represent the first glaciation on the Barents Sea shelf, and the onset of glacial deposition. R7 has an approximate age of 2.3Ma (Faleide, et al., 1996). The oldest sediment package, GI, is characterized by dipping clinoforms and reflectors of variable continuity, and has been interpreted to represent deltaic facies at the shelf margin. Units GII and GIII are characterized by chaotic reflection patterns, and interpreted to be a result of mass-movement deposits in relation to grounded glaciers (Andreassen, et al., 2007).

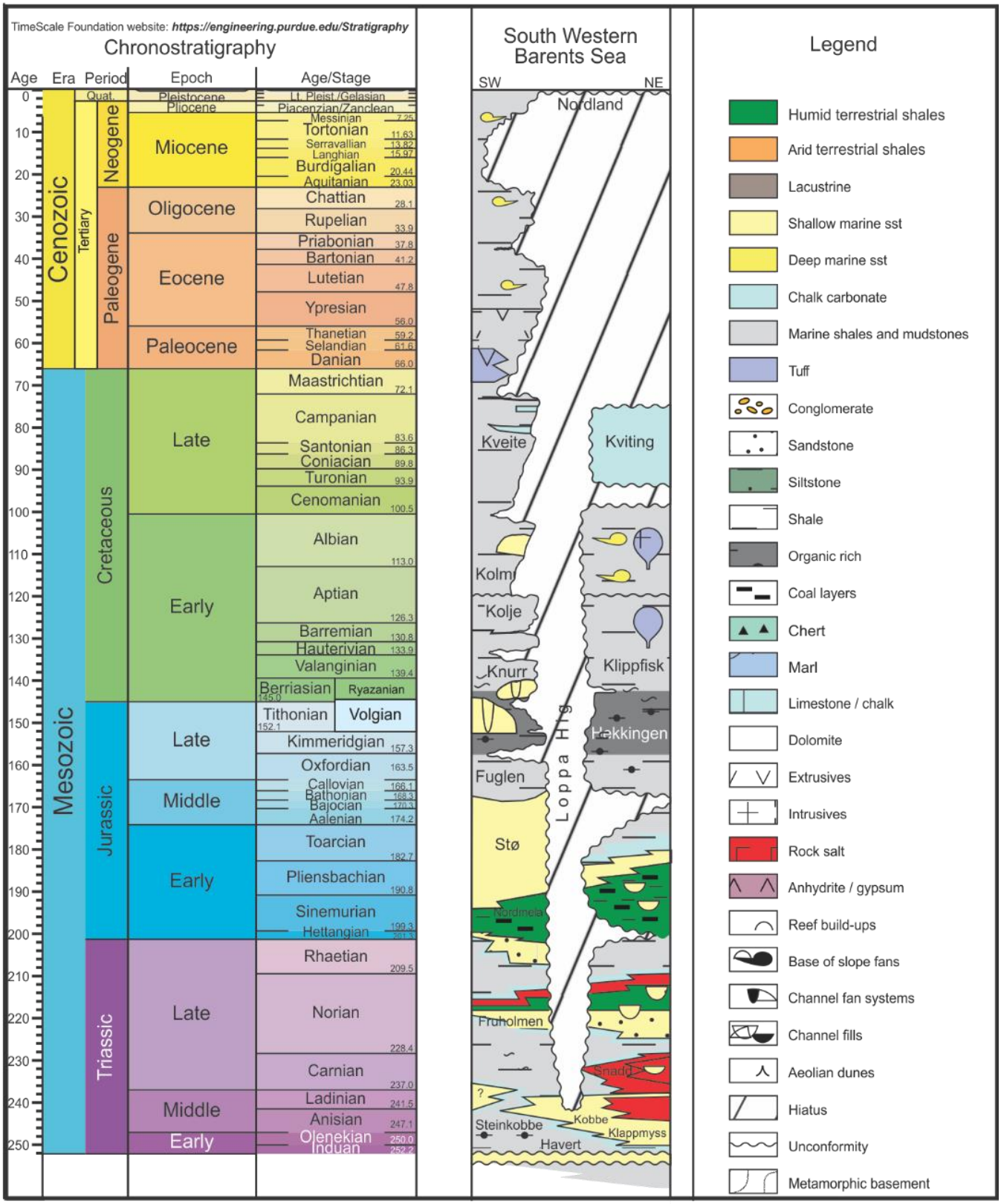


***Figure 3.2-1*** *Chart showing the litostratigraphy of the South Western Barents Sea. Modified from (Noreco, et al., 2013)*

## 3.3 Structural elements

The data used in this project paper is gathered from the survey CP11101, which mostly lies in the Ringvassøy-Loppa Fault Complex, separating the Tromsø basin and the Loppa High, (Figure 3.3-1).

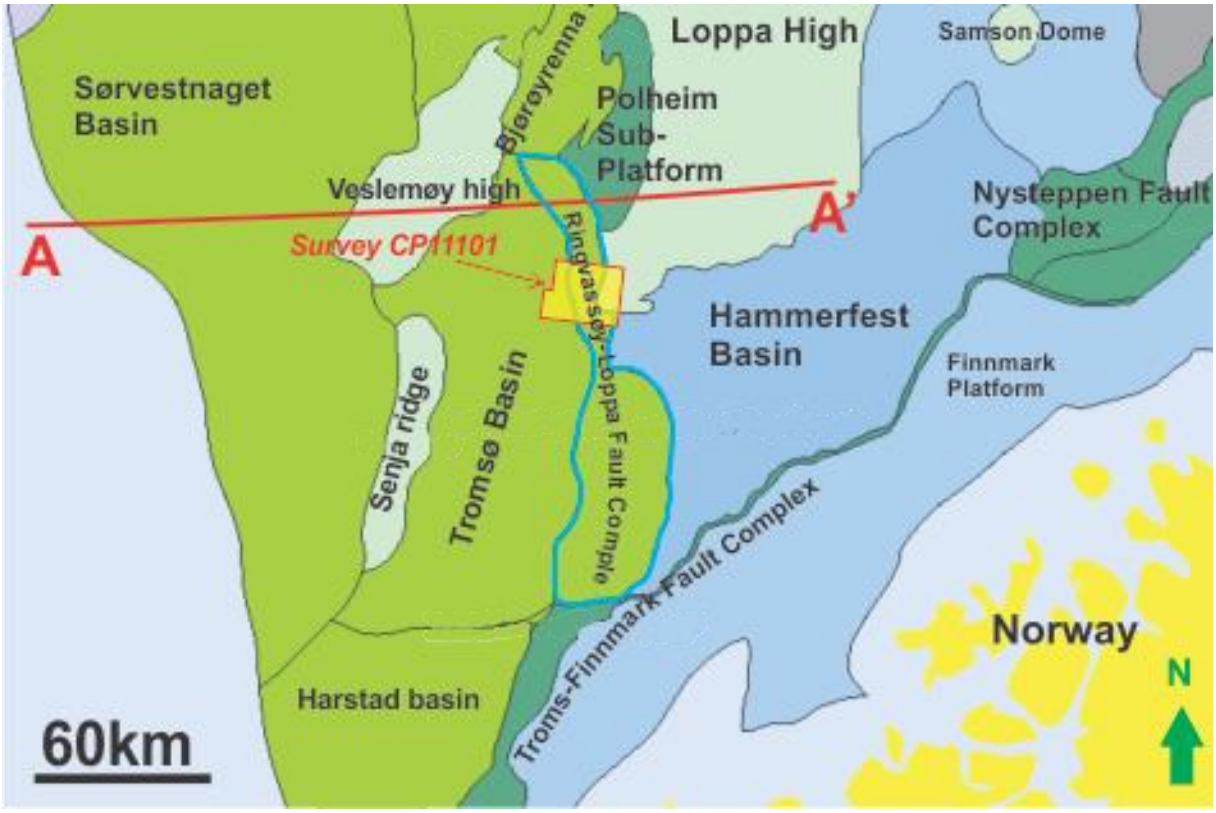


***Figure 3.3-1*** *Structural elements surrounding the area of study. Seismic 3D survey CP11101 is indicated by red polygon and cross-line (A-A') traversing Ringvassøy-Loppa Fault Complex is highlighted in red, see figure 3.3-2. Figure modified from NPD Fact Maps.*

### 3.3.1 Loppa High

The Loppa High consists of an eastern platform and a crestal western and northwestern margin. The high is located north of the Hammerfest Basin and south of the Bjarmeland Platform. In the west, the Loppa high is limited by two fault complexes, the Ringvassøy-Loppa fault complex and the Bjørnøyrenna fault complex. To the east, the high slopes gradually down to the Bjarmeland Platform. The Svalis salt dome and the Maud basin marks the northeastern extent of the Loppa High. From above the Loppa high has a diamond shaped outline (Gabrielsen, et al., 1990; Larssen, et al., 2002).

The area has been exposed to several periods of uplift/subsidence accompanied by erosion and tilting. The rift topography developed during the Late Carboniferous was infilled with Upper Paleozoic siliclastics, evaporites and carbonate. In the Late Permian to Early Triassic the Loppa Ridge was uplifted and tilted, followed by a gradual onlap in the Early and middle Triassic. In the Upper Triassic a thick sedimentary unit, the Snadd formation was deposited due to rapid subsidence. This Upper Triassic succession now subcrops the Quaternary (Halland, et al., 2016; Gabrielsen, et al., 1990).

### 3.3.2 Ringvassøy-Loppa Fault Complex

The Ringvassøy-Loppa Fault Complex (RLFC) is a north-south striking complex separating the Hammerfest Basin to the east and the deep Tromsø Basin to the west in the southern part of the complex. In the northwestern part it separates the Loppa High and Tromsø Basin. The Troms-Finnmark Fault Complex limits the southern extent of the complex, and the Bjørnøyrenna Fault complex defines the northern (Gabrielsen, et al., 1990). The RLFC and the Bjørnøyrenna Fault Complex marks a division of the southern Barents Sea. The western areas were very tectonically active during the late Mesozoic and Cenozoic, and thick depositions of Cretaceous, Paleogene and Neogene characterize the Harstad, Tromsø and Bjørnøya Basins. To the southeast, thick Upper Palaeozoic and Mesozoic sequences dominates, and faults with E-W, WNW-ESE to ENE-SSW orientation are found in comparison to the N-S to NNE-SSW trending faults in the western parts (Halland, et al., 2016).

The RLFC is a highly faulted region dominated by extensional structures and tilted fault blocks (Faleide, et al., 1984) where the faults strikes N-S, a trend best visible by the westerly faults. In plan view these fault traces appear as sublinear features. Crossing these faults, large throws can be identified, (Figure 3.3-2), lowering the Middle Jurassic reflector from 2.5 to approximately 5 seconds TWT. The easterly faults have a more concave outline facing towards the Tromsø Basin (Gabrielsen, et al., 1990).

The formation of the deep tilted fault blocks in the RLFC is probably related to the Late Kimmerian tectonic phase at the Jurassic-Cretaceous transition when a range of large normal faults was developed (Faleide, et al., 1984). During this period, the main subsidence also took

place along the southern segment of the RLFC. Later during the Late Cretaceous, the faults were reactivated affecting tertiary strata. There is also a possibility that the faults were active before the Mid Jurassic, but due to lack of seismic data in the deepest part of the Tromsø Basin this is not known (Gabrielsen, et al., 1990).

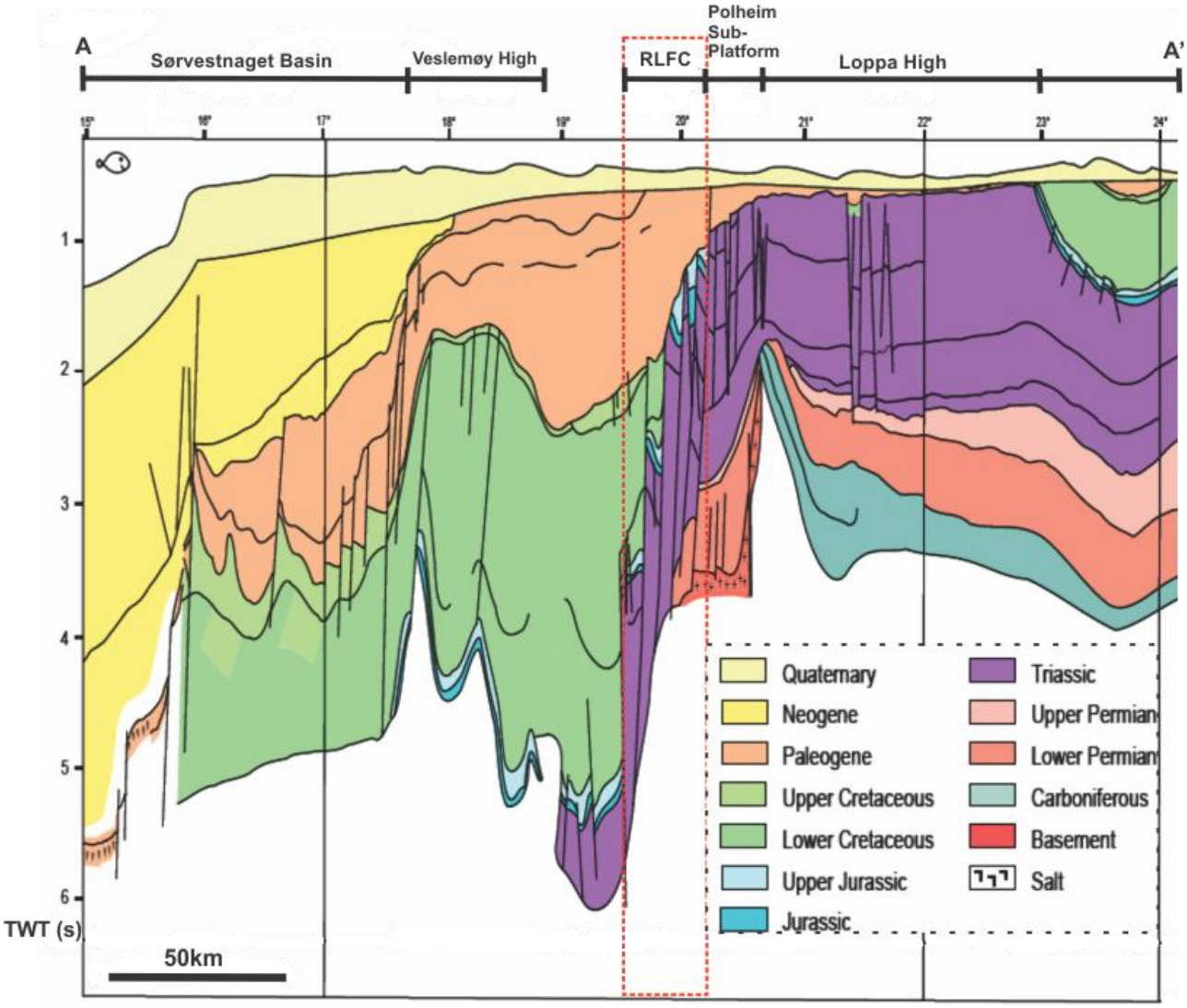


***Figure 3.3-2*** *Cross-section of line A-A' highlighted in Figure 3.3-1. Red dotted square indicate the main study area, the Ringvassøy-Loppa Fault Complex. Figure modified from (Halland, et al., 2016).*

### 3.3.3 Tromsø Basin

The Tromsø Basin is delimited to the east by the RLFC and the faulted structural high the Senja Ridge to the west (Faleide, et al., 1984). The northern extent of the basin is defined by the Bjørnøyrenna fault complex in the north east and the Veslemøy High in the North West. In the south, it terminated against the Harstad basin, and to the southeast, the Tromsø-Finnmark Fault Complex marks the extent (Gabrielsen, et al., 1990).

Salt diapirs occurring within the Tromsø Basin, probably developed from the Upper Carboniferous and lower Permian evaporate deposits, breaches the Mesozoic and lower Cenozoic sediments. The basin is delimited by north-south oriented fault complexes, the RLFC and the Senja Ridge Fault system. These fault complexes have been interpreted to have been active in both Mesozoic and Cenozoic time. This activity is interpreted to mirror the regional Cretaceous rift system that covered the basin (Knutsen, et al., 1992).

In the late Triassic to Early Jurassic time, the Tromsø, Bjørnøya and Hammerfest basins may have existed as a single basin, but faulting that started along the eastern margin of the Tromsø basin in the Middle Jurassic definitely separated the Tromsø basin from the Hammerfest basin. The Tromsø basin and the Bjørnøya basin probably did not separate until the late Cretaceous when lateral movement occurred in the Bjørnøyrenna Fault Complex (Gabrielsen, et al., 1990). As mentioned earlier, the western Barents Sea underwent much subsidence during the Cretaceous. This is especially evident in the Tromsø basin by an approximately 5 s TWT Cretaceous sediment sequence (Knutsen, et al., 1992).

## 3.4 Glacial evolution of the Barents Sea continental shelf

The Barents Sea continental shelf has experienced several glaciations during the Late Cenozoic, with ice advancing to the shelf break (vorren, et al., 2011). This chapter will describe a 5-stage reconstruction for the Late Weichselian maximum and later deglaciation, based on the work done by Winsborrow et al (2009) (Figure 3.4-2).

The south-western Barents Sea is characterized by multiple troughs, where the largest is the Bjørnøyrenna (Bear Island Trough) extending from Sentralbanken in the east to the shelf break in west traversing water depths from 300-500m. In the south the shallow Tromsøflaket and Nordkappbanken flank the Bjørnøyrenna. In the southernmost shelf area the two south-east to north-west lying Ingøydjupet trough and Djuprenna trough dominate the regional setting (Figure 3.4-1).

During the Late Weichselian maximum the Barents Sea continental shelf was glaciated by the Barents Sea Ice Sheet (BSIC) and the Fennoscandian Ice Sheet (FIS), and active ice streams operated on the shelf area. From mapping of glacial landforms, position, extent, and the behaviour of ice streams during deglaciation has been reconstructed for the southern Barents Sea (Winsborrow, et al., 2009).

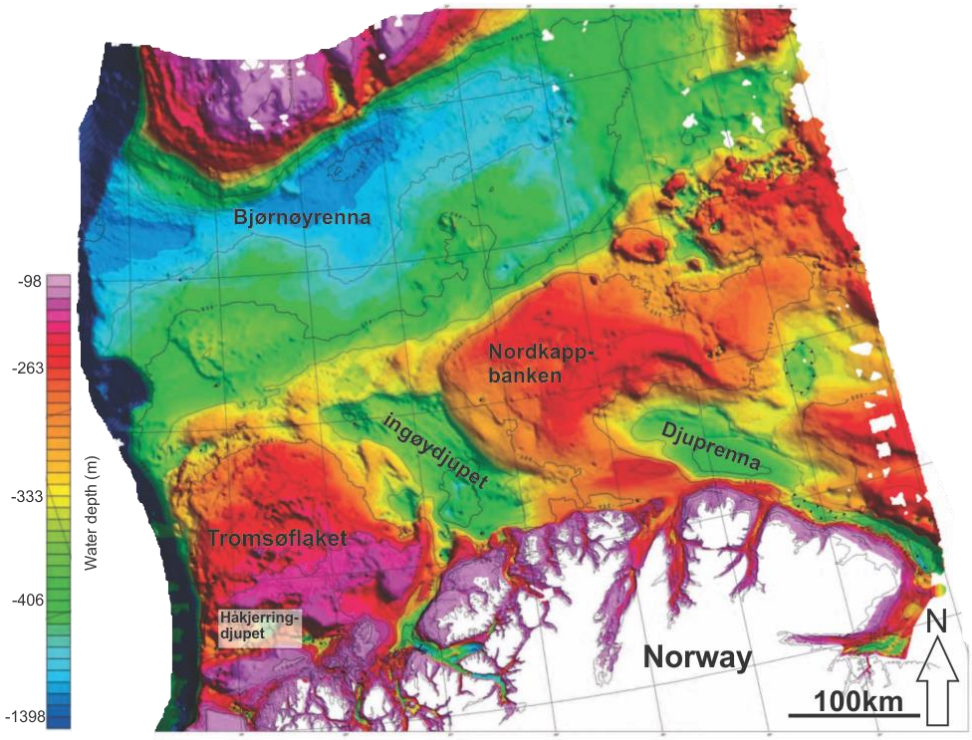


***Figure 3.4-1*** Bathymetry map of the southwestern Barents Sea. Modified from *(Smelror, et al., 2009)*

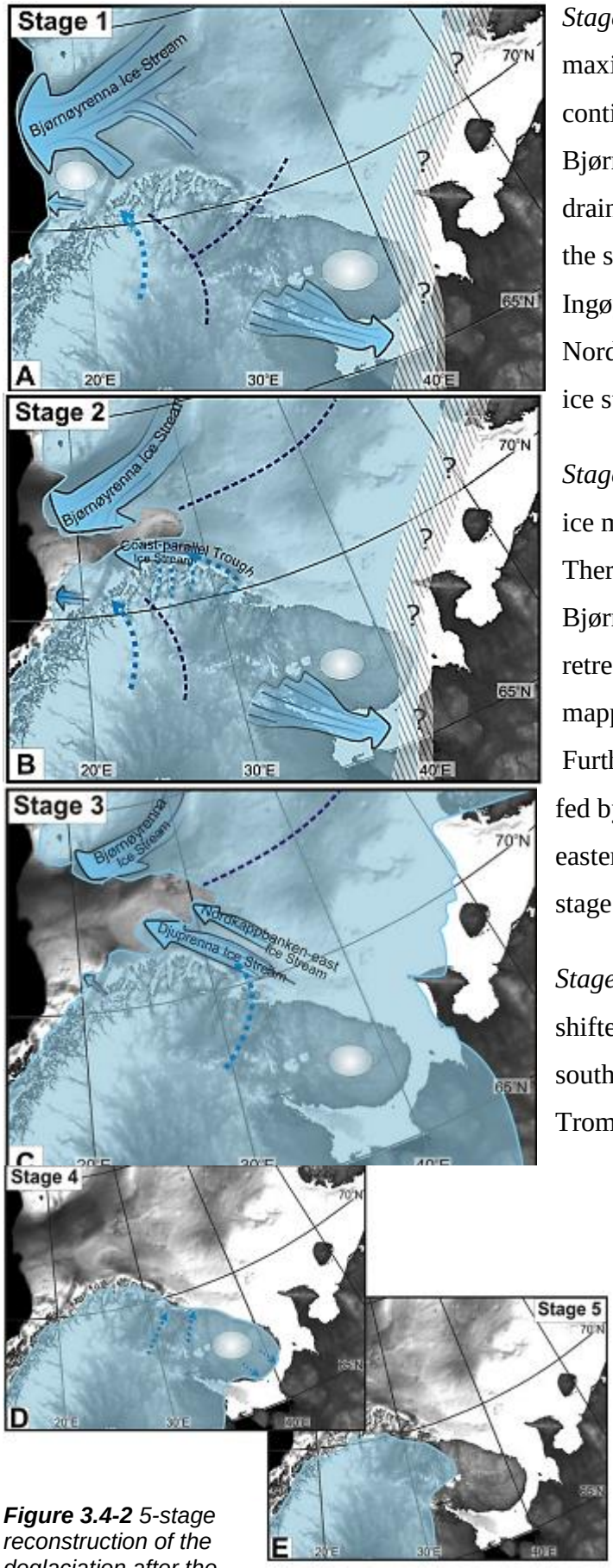


***Figure 3.4-2*** *5-stage reconstruction of the deglaciation after the Late Weichselian maximum in the southern Barents Sea. White circle indicate cold-based ice. From (Winsborrow, et al., 2009).*

*Stage 1)* During the Late Weichselian maximum the entire Barents Sea continental shelf were covered by ice. The Bjørnøyrenna ice stream acted as the main drainage system in the north, whereas in the south, the ice streams within the Ingøydjupet and in the present day Nordkappbanken operated. There was also ice streams in the Håkjærringdjupet.

*Stage 2)* Deglaciation commenced and the ice margin underwent a substantial retreat. There is evidence for the ice streams in the Bjørnøyrenna and Håkjærringsdjupet retreating and readvancing based on mapped grounding zone wedges. Furthermore, a coast-parallel ice stream, fed by areas inland, developed. In the eastern regions the ice-sheet remained as in stage one.

*Stage 3)* the center of maximum ice volume shifted towards east, leaving much of the southern Barents Sea ice-free, including Tromsøflaket and the deepest parts of Bjørnøyrenna.

*Stage 4) and 5)* by this stage the southern Barents Sea had no ice-cover and the ice margin was localized within the outer-fjord areas (Winsborrow, et al., 2009).

Exact age dating for the 5-stage reconstruction is not given, but by comparison with literature Winsborrow et al (2009) have given a suggested timeline. Dates presented are calibrated to calendar year before present. Stage 1 is interpreted to be of an age of 19 cal. ka. BP when the ice stream in Bjørnøyrenna reach the shelf edge. Stage 2 is assigned the approximate age of 17 cal. ka. BP, stage 3 - 16 cal. ka. BP, stage 4 - 15 cal. ka. BP and stage 5 - 12.5 cal. ka. BP (Winsborrow, et al., 2009).

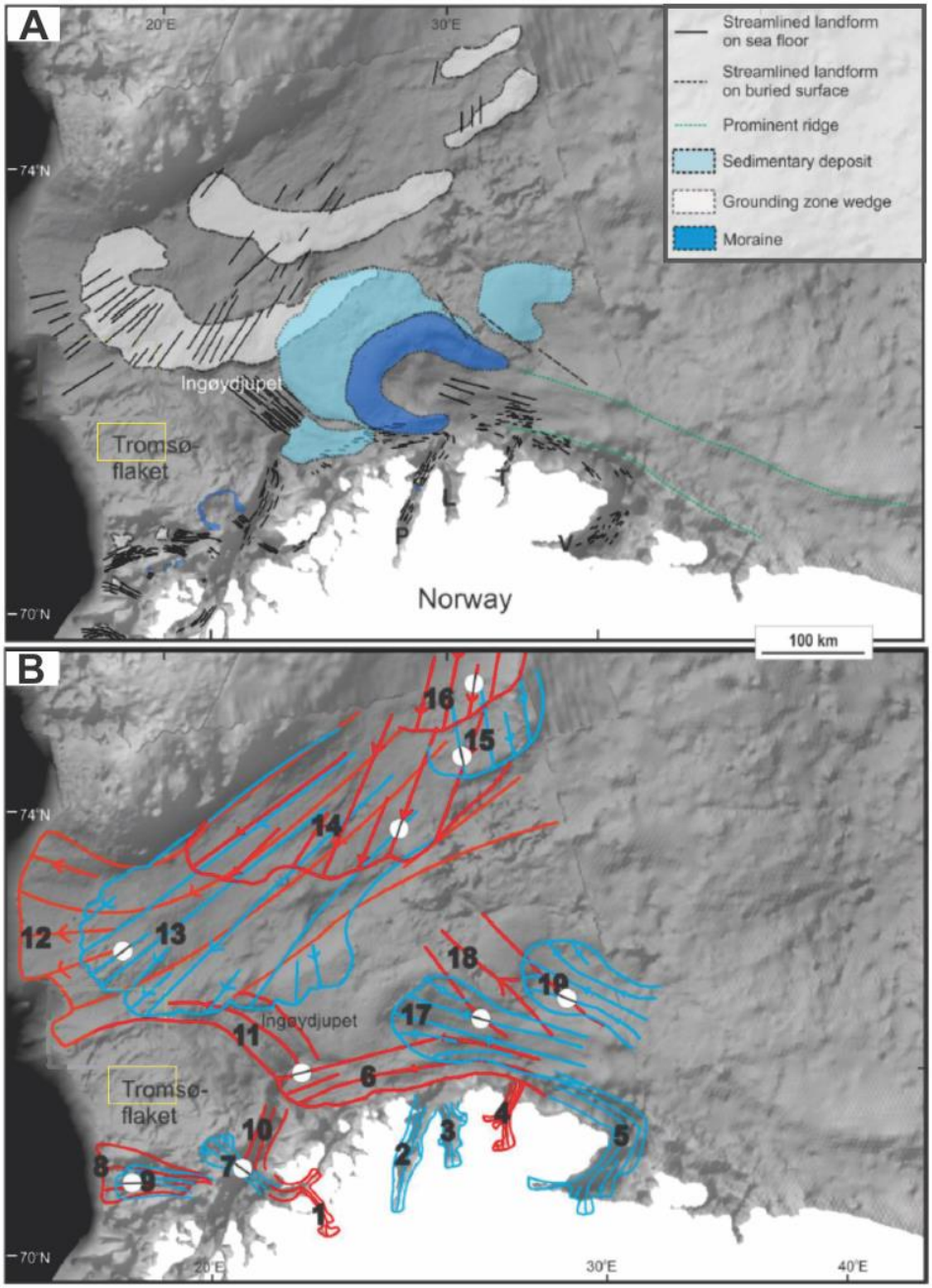


***Figure 3.4-3*** *A) Map illustrating the glacial landforms in the southern Barents Sea. B) Map showing flow-sets representing different glacial events in the southern Barents Sea. Approximate position of study area is indicated by yellow box. Modified from (Winsborrow, et al., 2009)*

The study area for this thesis, indicated in Figure 3.4-3, is located on the Tromsøflaket, a shallow bank area with water depths around 200m. Winsborrow, et al (2009) have mapped several glacitectonic landforms and streamlined flow sets flanking the Tromsøflaket. South-east to north-west oriented MSGL, flow set 7, are however the only streamlined features found on Tromsøflaket. The inner parts of Tromsøflaket, are interpreted to be based in a cold ice setting and therefore lack the characteristic fast flowing warm based ice stream landforms (Winsborrow, et al., 2009). Nevertheless, glacitectonic hill-hole pairs have been identified on the bank, south of the study area. These glacitectonic landforms are usually related to slower moving ice and deglaciation (Ottesen, et al., 2005).

# 4 Data and methods

## 4.1 Seismic data

The seismic data used in this thesis is located in Tromsø Basin, RLFC, Loppa High and partly in the Hammerfest basin (figure 4.1-1). The study is based on one 3D seismic survey, the Caliente 3D. Two sets of 2D seismic lines and two wells in the area have been used for correlation of units and formation tops.

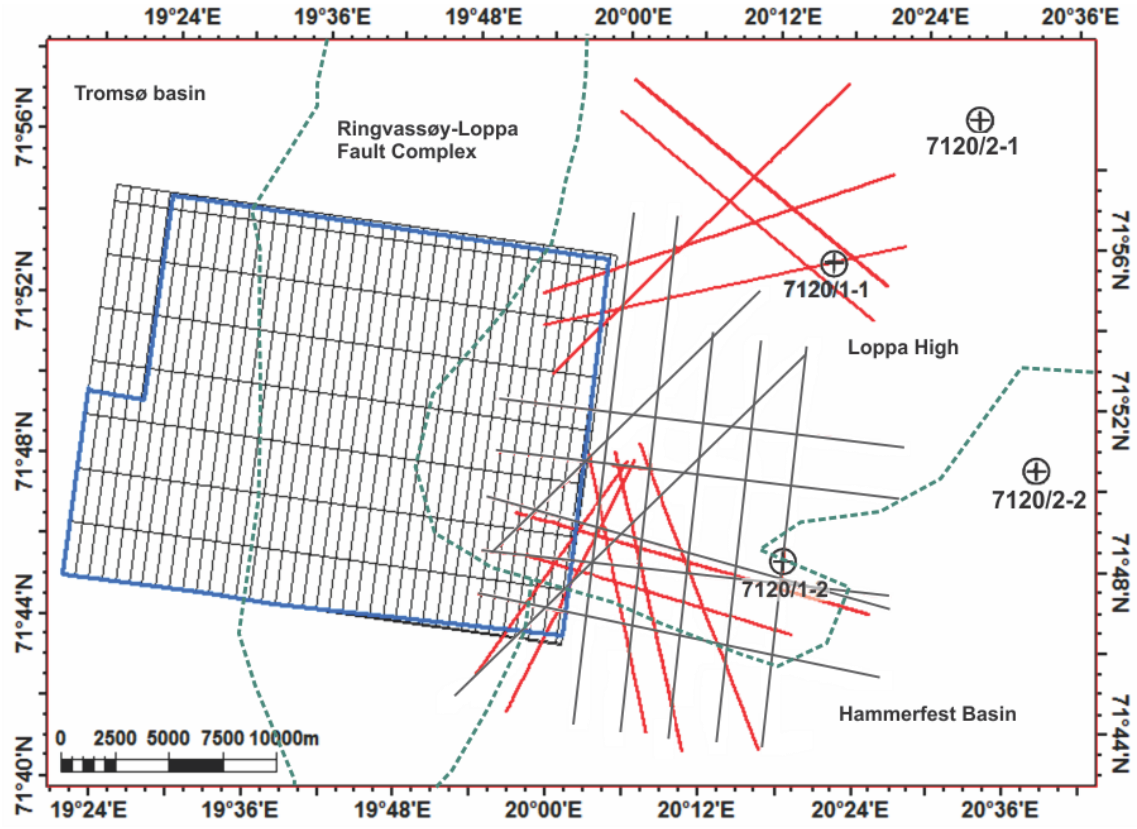


***Figure 4.1-1*** *Map showing position of 3D data, 2D lines and wells. 3D seismic survey CP11101 is indicated by black gridded box, blue box within indicate the surface polygon where interpretation is made. Red and grey lines show location of respectively SH-9103 and SH-8601 2D lines. Green dotted lines marks the basin boundaries.*

The polarity standard used for this study is the SEG (Society of Exploration Geophysicist) of Sheriff (2006). For a zero-phase wavelet, with normal polarity, black peaks represent positive reflection coefficients. For a minimum-phase wavelet with normal polarity on the other hand, an initial white trough followed by a black peak represents an increase in acoustic impedance. Reversed polarity shows the opposite representation in seismic data, and negative reflection

coefficients are represented as peaks for zero-phase wavelets, and initiated by troughs followed by peaks for minimum-phase wavelets, (Figure 4.1-2).

In this study, positive reflection coefficients are given a blue color, and negative coefficients a red/yellow color. Some of the 2D lines used for correlation exhibited a reversed polarity, these were phase reversed in Petrel to ease correlation with 3D survey.

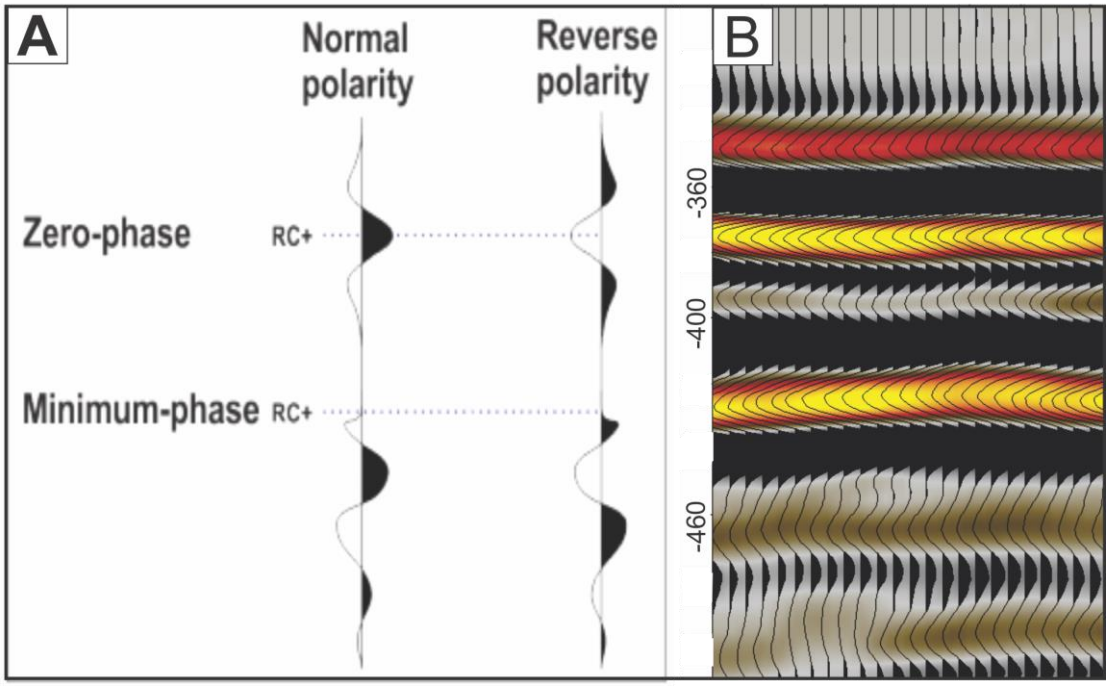


***Figure 4.1-2*** *A) Polarity convention used in this thesis, SEG. Figure modified from sheriff 2006. B) Zero-phase wavelet with normal polarity showing the positive seabed reflection coefficient at approximately -360ms TWT.*

### 4.1.1 Caliente 3D (CP11101)

The 3D seismic dataset Caliente 3D, (Figure 4.1-1), was acquired from 12$^{th}$ September 2011 to the 10$^{th}$ of November 2011 by Polarcus Seismic Limited on behalf of ConocoPhillips Skandinavia AS. The survey is located in the southern Barents Sea on the boundary between the Loppa High and the Tromsø Basin, in the Ringvassøy-Loppa Fault Complex with a total net area of 519,61 km$^2$ (NPD, 2016).

***Table 4.1-1*** *Summary of survey CP11101 seismic character and geometry.*

| Polarity | Phase | Dominating frequency (Hz) | Area ($Km^2$) | Inlines | Crosslines | Inline orientation |
|---|---|---|---|---|---|---|
| Normal | Zero-phase | 10-55 | 519,61 | 730 | 3748 | E-W |

### 4.1.2 2D seismic lines

The 2D seismic lines used in this thesis are the SH-8601 and SH-9103, both located in block 7120/1 (Figure 4.1-1). These lines have been required from the NPD's Petrobank, however no further documentation are given.

### 4.1.3 Well data

There has been given well data from four wells located in Loppa High, east of the Caliente 3D. Wells 7120/1-1 and 7120/1-2 are located within the range of the 2D lines, and thereby provide stratigraphic correlation with the 3D survey. General information about the two wells are given in Table 4.1-2.

Well 7120/1-1 is located on the western flank of the Loppa High, and the objective was to test Palaeozoic carbonates and Early Triassic sandstones in a fault-bounded/truncated dip closure. Weak hydrocarbon shows were identified from 800-2200m and oil shows in Late Permian carbonates. No reservoir quality was detected in Tertiary or Triassic sequences and the Paleozoic carbonates showed low porosities. The well was decommissioned in July 1986, and classified as a dry well with hydrocarbon shows.

Well 7120/1-2 is located on the southern border of the Loppa High. The well was drilled with the purpose to map two Aptian seismostratigraphically wedges in a fault-bound closure against the high. Oil shows were detected in several units below 1931m and a 90m oil column was recorded in the second wedge of Ryazanian/ Early Valanginian age. Testing revealed that reservoir quality was poor, and most of the oil was immovable. No shallow gas shows were identified. The well was decommissioned in March 1989 as an oil discovery (NPD, 2016).

***Table 4.1-2*** *General information about well 7120/1-1 and 7120/1-2. Table content gathered from (NPD, 2016).*

| Wellbore name | Drilling operator | Entered date | Content | Total depth (m) |
|---|---|---|---|---|
| 7120/1-1 | A/S Norske Shell | 16.08.1985 | OIL/GAS SHOWS | 4003 |
| 7120/1-2 | A/S Norske Shell | 01.01.1989 | OIL | 2630 |

## 4.2 Seismic resolution

"*Resolution is the ability to distinguish separate features, and is commonly expressed as the minimum distance between two features, such that two can be defined rather than one* (Sheriff, 1985)*".*

When interpreting seismic data the resolution of the seismic reflections is key for extraction of stratigraphic detail (Chopra, et al., 2006). Detection of seismic reflections are however limited by the sensitivity of the seismic acquisition and processing system (Andreassen, 2009) as well as their magnitude compared with wavelength. Equation 6 show the relationship between wavelength, velocity and frequency (Sheriff, 1985).

$$\lambda = v/f \tag{6}$$

Where λ= wavelength (m), v= velocity (m/s) and f=frequency (Hz)

Since velocity generally increases with depth, and frequency decreases, wavelengths become larger, and as wavelength limits resolvability, deep features need to be much larger to be sufficiently resolved (Figure 4.2-1). The resolution of seismic data concerns two aspects: vertical (time or depth) and horizontal (from trace to trace) resolution (Sheriff, 1985).

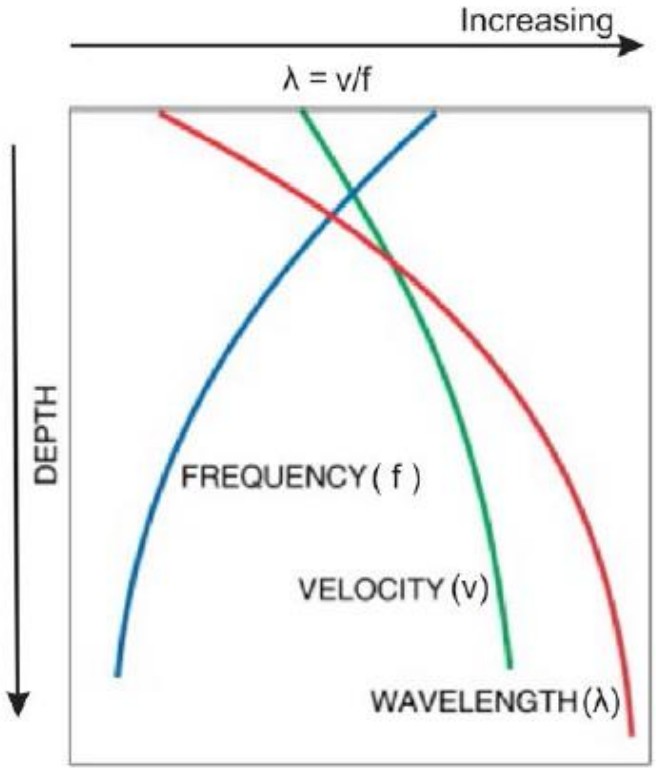


***Figure 4.2-1*** *Illustration of how frequency, velocity and wavelength change with depth. Figure from (Brown, 2003)*

## 4.2.1 Vertical resolution

Vertical resolution refers to the limit of separability, the minimum separation between two reflectors where both are visible as single events corresponding to different depths. This limit is equal to ¼ of the wavelength (equation 7) (Andreassen, 2009; Sheriff, 1985; Rafaelsen, 2006).

$$Vr = \lambda/4 \quad (7)$$

Where $V_r$=vertical resolution (m), λ= wavelength (m)

Figure 4.2-2 illustrates the concept of vertical resolution. As long as the thickness of the limestone wedge is larger than ½ of the wavelength, the wavelets from the top and bottom interface will not interfere, hence we can distinguish them from one another. Below this point constructive interference occurs, forming a single wavelet trace with anomalously high

amplitude. This interference is at its maximum when the thickness of the wedge reaches ¼ of the wavelength, also known as the tuning thickness. When the thickness of the wedge becomes less than that of the tuning thickness, destructive interference comences until the theoretical detection limit of 1/30 wavelength is reached, and the wavelets wil appear as one single interface (Andreassen, 2009; Badley, 1985).

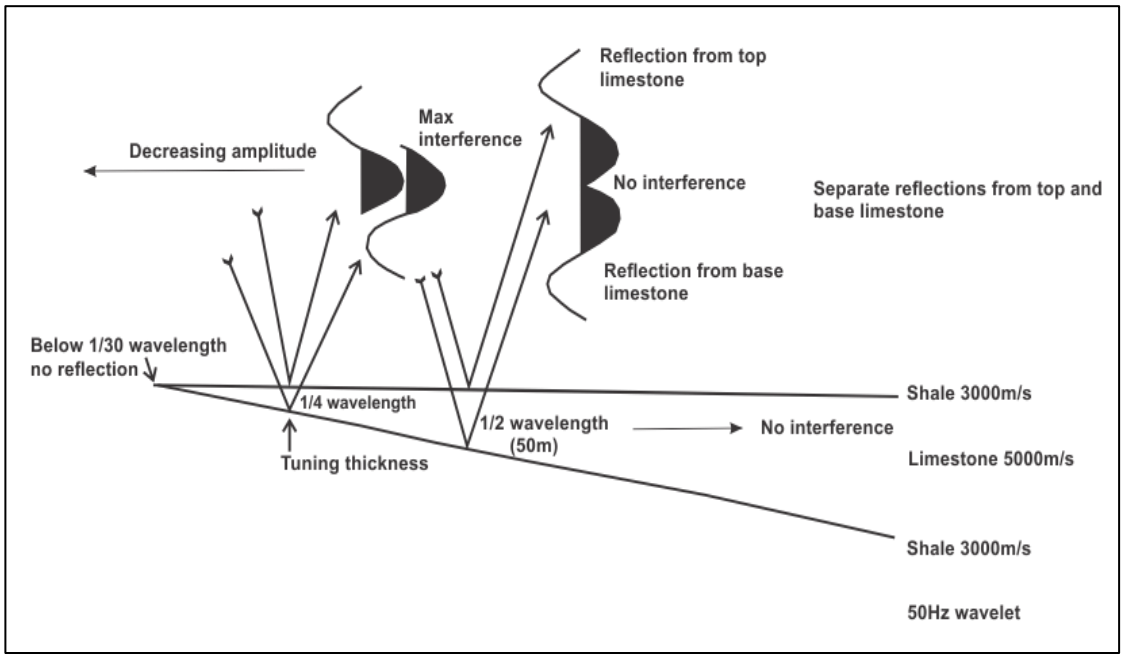


***Figure 4.2-2*** *Illustration of interference effects occurring for a high velocity wedge and its implications for vertical resolution. Wavelet in figure is a minimum phase wavelet. Figure modified from (Andreassen, 2009) and (Badley, 1985).*

## 4.2.2 Horizontal resolution

Horizontal or lateral resolution refers to the minimum distance between two lateral located reflectors, where both are still distinguishable from each other. It also determines the minimum size for feature detection. The horizontal resolution for unmigrated seismic data is determined by the width of the first Fresnel Zone. Since seismic reflections travels as a wave front and not as single rays, the resulting reflection is generated from a circular zone. This zone is limited by the area that the wave front arriving ¼ wavelength later than the first wave front, makes with the reflector. This zone is known as the first Fresnel zone (Figure 4.2-3).

The Fresnel zone can be approximated from the following relationship:

$$rf = \frac{v}{2}\sqrt{\frac{t}{f}} \tag{8}$$

Where rf= radius of the Fresnel zone (m), V= average velocity (m/s), t= two-way travel time (s) and f=dominant frequency (Hz).

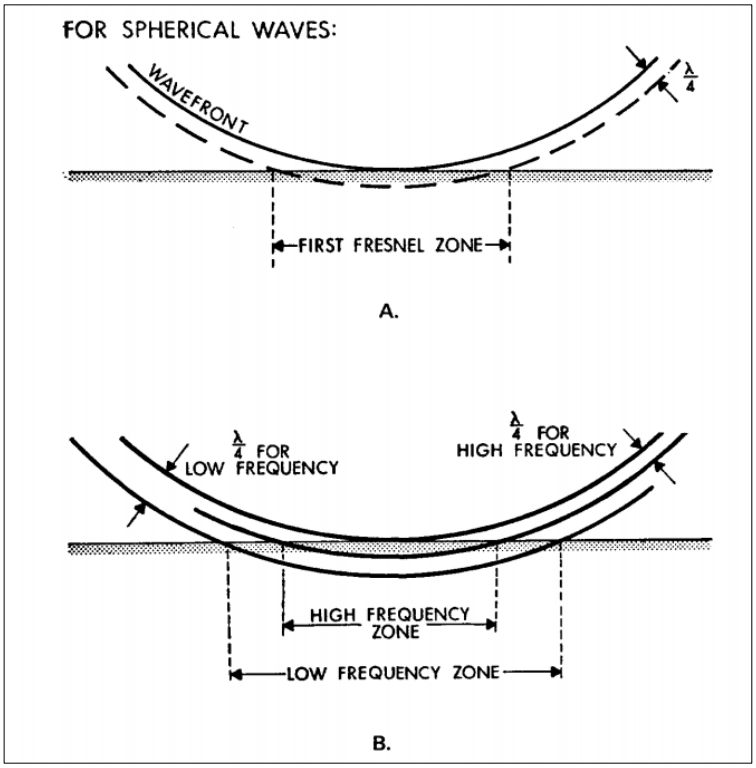


***Figure 4.2-3*** *Illustration of the Fresnel zone. A: area limited by the first wavefront tangent to the plane reflector and the wavefront arriving ¼ wavelength later makes up the first Fresnel zone. B: the Fresnel zone will be larger for low-frequency waves than for high- frequency ones, hence high-frequency components will have higher spatial resolution (Sheriff, 1985).*

From equation 8, we can see that the radius of the Fresnel zone increases with depth, lower frequencies, and increasing velocity, hence lowering horizontal resolution. To increase horizontal resolution the size of the Fresnel zone needs reducing. This is done by a seismic processing technique called migration. 2D Migration will collapse the Fresnel zone to an ellipse perpendicular to the seismic line direction, while 3D migration will reduce the size of the Fresnel zone to a small circle, allowing more detailed spatial resolution (Figure 4.2-4). The limit for horizontal resolution in 3D migrated data is given by the diameter of the Fresnel

zone, being one quarter of the wavelength (Andreassen, 2009; Sheriff, 1985; Rafaelsen, 2006; Brown, 2003).

$$Fd = \frac{\lambda}{4} \tag{9}$$

Where Fd= diameter of the Fresnel zone (m) and λ= wavelength (m).

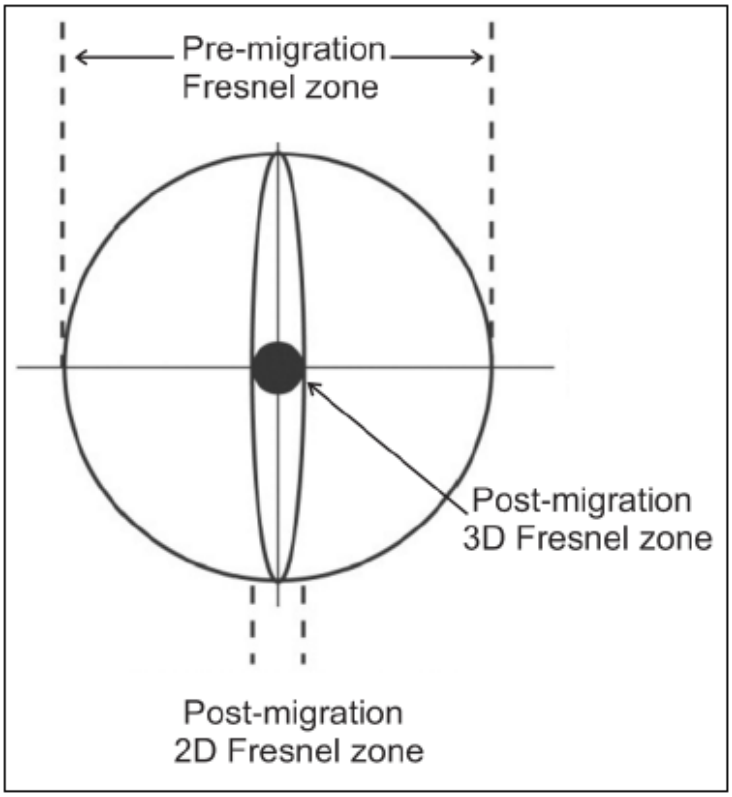


***Figure 4.2-4*** *Illustration of the effects of 2D and 3D migration. 2D migration will collapse the Fresnel zone to an ellipse in inline direction while 3D migration reduces the Fresnel zone to a small circle. Figure modified from (Andreassen, 2009)*

### 4.2.3 Vertical and horizontal resolution for 3D survey CP11101

Vertical and horizontal resolution for survey CP11101 has been calculated using equation 7, 8 and 9. Table 4.2-1 shows the results. An average p-wave velocity of 2700 m/s is used to calculate the resolution. Velocity is gathered from well log data (well 7120/1-2) and taken as the average p-wave velocity in the upper 1600ms TWT (2700m/s) above the Kojle Formation. t from eq. 8 is sat to 1s, as most of the features interpreted lies around this time (TWT). Frequency is taken from the frequency spectral analysis (Figure 4.2-5), as the peak frequency 27Hz

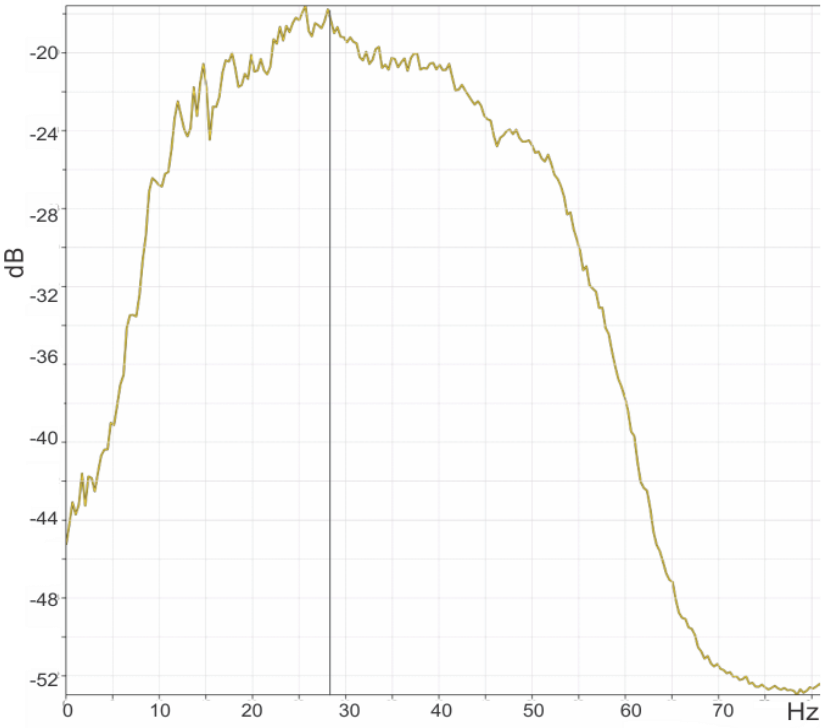


***Figure 4.2-5**: Frequency Spectral analysis form petrel. Dominating frequency 10-55 Hz, peak frequency 27Hz*

***Table 4.2-1** table showing the dominant frequency for survey CP11101 and the horizontal and vertical resolution. An average velocity of ….*

| Survey name | Dominant frequency (Hz) | Wavelength (m) ($V_p$= 2700m/s) | Horizontal resolution, pre-migration (m) | Horizontal resolution, post-migration (m) | Vertical resolution (m) |
|---|---|---|---|---|---|
| CP11101 | 27 | 100 | 259.8 | 25 | 25 |

## 4.3 Artefacts

The 3D survey used in this thesis exhibit artefacts in the form of survey footprints. Survey footprints are systematic noise aligned with acquisition geometry, and occur as parallel lines with the same orientation as the seismic inlines. Survey footprints can complicate identification of seabed and subsurface geological features (Bulat, 2005). In Figure 4.3-1, the survey footprints appear as dim amplitude zones, which can be mistaken as gas anomalies.

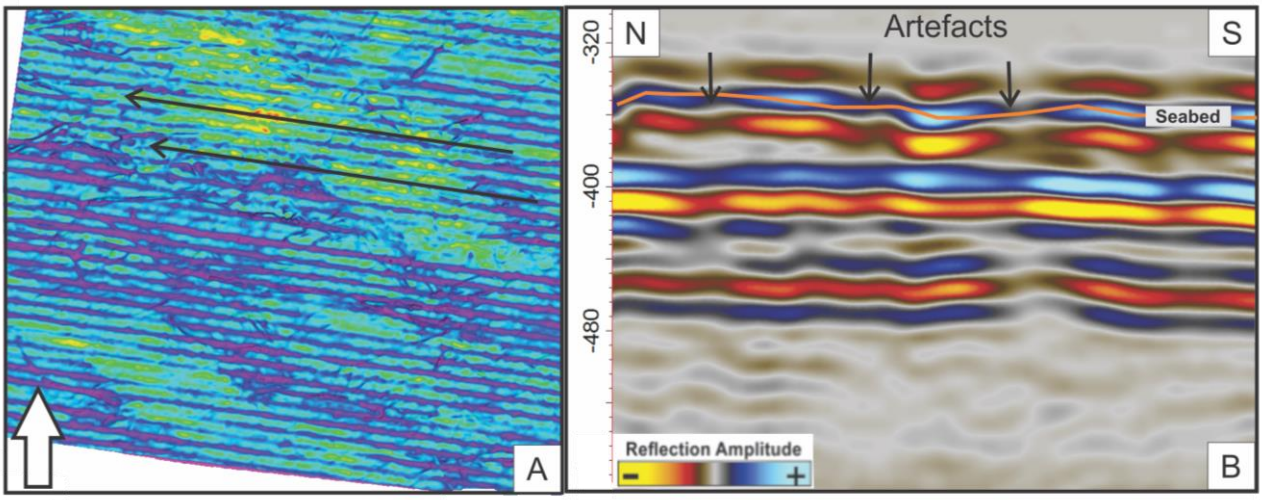


***Figure 4.3-1*** *A) continuous parallel lines with same orientation as the seismic inlines of survey CP11101. RMS attribute map of the seabed has been used to emphasize the appearance of the survey footprints. B) Seismic line perpendicular to the artefacts showing the footprints dim amplitude character.*

## 4.4 Interpretation tools and methods

For this thesis the main interpretation and visualization tool was the Petrel 2015.4 software from Schlumberger. Petrel provide several tools and attributes that have been used for seismic interpretation of horizons, volumes, and for well correlation. The depth of the seismic data is given in TWT. Figures were created and modified using the CorelDraw X6 software from Corel Corporation.

### 4.4.1 Seismic attributes

A seismic attribute is defined as a quantitative measure of a seismic characteristic of interest (Chopra & Marfurt, 2005). Attributes are valuable for their ability to enhance geological understanding of interpretations. In Petrel attributes can be applied to interpreted surfaces or specified volumes in the seismic cube, respectively surface attributes and volume attributes.

Seismic horizons were created using 2D seeded autotracking, 3D seeded autotracking and the paintbrush tool in Petrel. Initially seeds were picked on every 10-50 inline, crossline or arbitrary line using the 2D seeded autotracking tool until a general comprehension of the surface were obtained, then the 3D seeded autotracking were used with a high seed confidence. Areas still blank were then filled using the paintbrush tool.

Structural smoothing is a volume attribute which increases the continuity of seismic reflectors (Schlumberger, 2011). This attribute can be useful when tracking horizons with little continuity, saving much tedious work. Smoothing of individual surfaces were also used in this study, mainly to eliminate miss picks in difficult areas.

To map amplitude anomalies in the survey, the RMS amplitude attribute were utilized. The RMS amplitude attribute calculates the root mean square of the sum of trace samples in a specific window. RMS amplitude surfaces are useful for mapping out features arising from high amplitude responses (positive or negative RC) such as gas accumulations and sediment blocks etc. (Schlumberger, 2011).

By creating a variance attribute cube, one emphasizes discontinuities in the horizontal continuity of amplitudes. In this thesis, variance attribute maps were used to identify both large- and small-scale faults at specific depths.

# 5 Results

This chapter present findings and interpretations done for the Caliente 3D. The focus has been to map vertical and lateral amplitude anomalies to study fluid migration within the study area, and to identify and describe geomorphological features. Several key seismic horizons have been interpreted for this purpose, and make up the regional understanding of the study area.

## 5.1 Seismic stratigraphy and faults

The focus of this study comprises the geological sequences from Cretaceous to present, hence deeper stratigraphy are given limited consideration. The seismic stratigraphy within the 3D seismic study area is determined by use of two wells, 7120/1-1 and 7120/1-2, located respectively NE and SE of the survey (Figure 4.1-1) on the Loppa High. 2D seismic lines provide connection between the survey and the wells. Due to the complex faulted geology on the western flank of the Loppa High, acoustic masking, and little overlap between the 2D lines and the 3D seismic survey, well tie is difficult. Additionally, continuity of the seismic reflectors within the study area are of variable extent, hence interpreted surfaces exhibit much uncertainty.

Surface six (S6) is characterized by a weak negative reflection coefficient with poor continuity (Fig. 5.1-1). From well correlation S6 is interpreted to be of Early Triassic age, corresponding to a seismic reflection close to the Fruholmen Formation. S6 can be mapped through most of the study area, except in the south-eastern part where it is delimited by the depth of the seismic cube. The surface is affected by multiple Triassic faults with great throws. The depth of S6 varies considerably from 5 s TWT in the Tromsø basin in the southwest to 1.5 s TWT on the Loppa High in the northeast.

Surface five (S5) exists in the entire study area, except for the northeastern parts where it terminates against the Triassic surface S6 in a large normal fault (fig.5.1-1). S5 is characterized by a weak positive reflection coefficient with limited continuity. Well correlation indicate Early Cretaceous age, corresponding to a seismic reflector close to the Knurr Formation. As S6, S5 is affected to the same extent by the faults. Depth increases towards west, with a depth of 4.75 s TWT in the Tromsø Basin, and 1.75s TWT on the Loppa High.

Surface four (S4) is interpreted to be of Cretaceous age, and correlate close to the top of the intra Cretaceous Kolje Formation (fig.5.1-1). S4 is mainly affected by two normal N-S striking faults (F1 and F2). F1 affects sediments from Triassic to Tertiary age. S4 is characterized by a positive reflection coefficient. The continuity and strength of S4 is good and strong west of F1. However, east of F1, both strength and continuity weakens. Like S5, S4 terminates against Triassic strata in the eastern part of the study area limiting the extent. Depth measures show the same trend as S6 and S5, increasing from 1.7 s TWT on the Loppa High to 3.55s TWT towards the Tromsø basin.

Surface three (S3) is mapped for the whole study area, and is interpreted to represent the base Tertiary, top Kveite Formation (fig. 5.1-1). The surface appear as a strong discontinuous reflector with a positive reflection coefficient. S3 is affected by F1 and F2 along with many small faults west of F1. Contrary to S6-S4 the surface has a less significant dip, and depth varies from 1.5 s TWT on the Loppa High, to 2.3 s TWT in the south-eastern study area. The throw across F1 and F2 is also much less than for the underlying surfaces.

Surface two (S2) is found throughout the study area. S2 is characterized by a discontinuous reflector with a negative reflection coefficient (fig.5.1-1). Amplitude strength varies noticeably all over the surface, appearing as series of bright spots. The surface correlates to Tertiary age, but no well tie lies in close proximity, and S2 is incorporated due to its many amplitude anomalies. The depth of the surface varies from 1.4 s TWT in the deepest southwestern area to 0.55s TWT in the northeastern area where it truncates the surface 1.

Surface one (S1) is mapped for the entire study area and is characterized by a strong continuous, negative reflection coefficient. S1 is interpreted to represent the reflection just above the Upper Regional Unconformity, the URU. The URU itself is not mapped as it mimic S1 over the whole area, and their close spacing makes it unnecessary. For convenience, S1 is referred to as the URU in this thesis. The seabed (S0) has also been mapped throughout the study area and it is characterized by a strong continuous, negative reflection coefficient.

All stratigraphic layers show the same trend of shallowing towards the Loppa High

S3, S2 and S1 are key seismic horizons for this study, and are given much attention in the following sections.

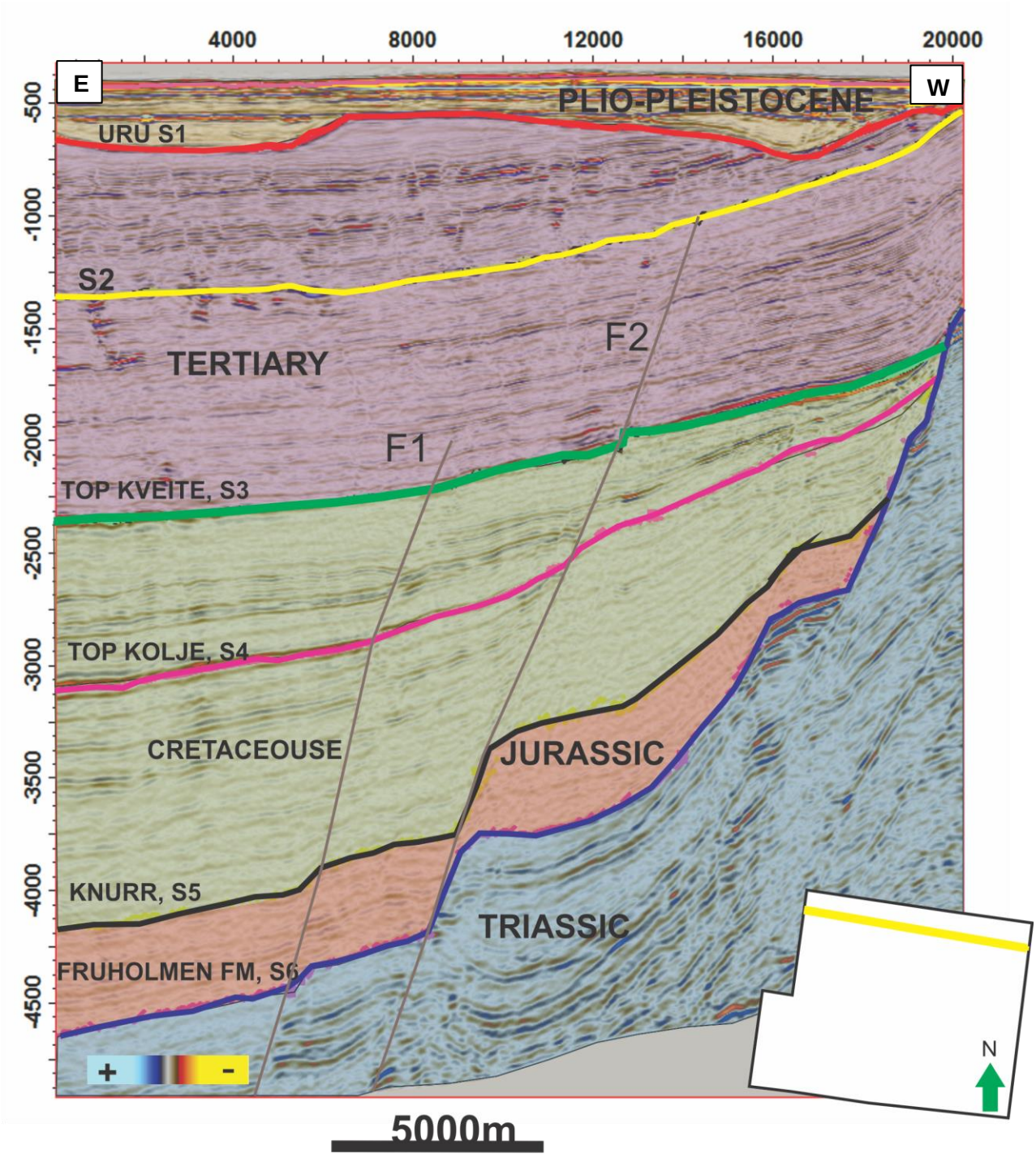


***Figure 5.1-1*** *seismic section showing the stratigraphic division within the study area. Surface S6-S4 are annotated with formation-top names from well 7120/1-1 and 7120/1-2. However, these are not accurate but due to their close proximity to the actual well picks, they are used to better get an overview of the stratigraphy. Location of seismic line is indicated in the lower left corner.*

### 5.1.1 Faults

Two large normal faults dominate the study area, F1 and F2 (figure 5.1-2). The faults affect stratigraphic levels from Triassic to Tertiary. F1 and F2 have a N-S strike orientation and dips towards the Loppa High in East. The fault throws vary in both strike and dip direction, increasing with depth. F1 is identified over the whole study area and curves towards west. In the southern part the fault plane is recorded to terminate in the URU. F2 is located in the northeastern region of the study area, and like F1, it curves towards west. The southern extent of F2 cannot be determinated due to the poor quality of the seismic in this region.

Other small-scale faults are identified west of F1, these affect, in varying degree, stratigraphic levels from S4, the Top Kolje Formation, to shallow Tertiaty units below the URU. However most of the faults are found in the interval from surface S4-S2. The faults have a NW-SE strike orientation and dips towards east and west. In Figure 5.1-2C, they can easily be identified.

F1 and F2 are interpreted to represent the tilted fault blocks in the RLFC. These probably relate to the Late Kimmerian tectonic phase at the Jurassic-Cretaceous transition and the later reactivation in Late Cretaceous when the faults affected tertiary strata (Faleide, et al., 1984; Gabrielsen, et al., 1990). All faults terminate below the URU, implying a pre-glacial origin.

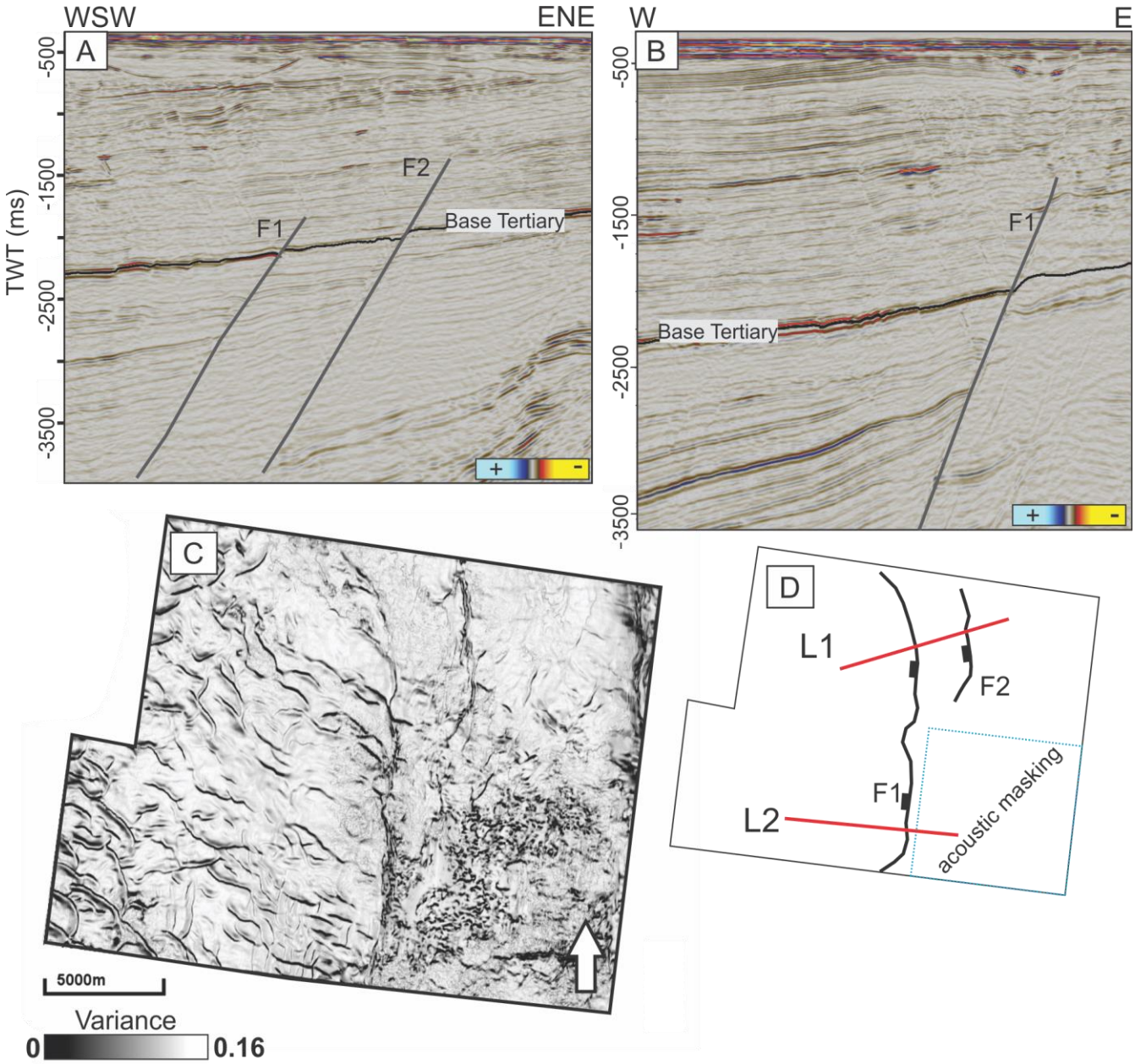


***Figure 5.1-2:*** *A) seismic profile (L1) crossing over both the deep-seated faults F1 and F2 in the norther part of the study area, Position of line is indicated in D). B) seismic profile (L2) crossing over F1 in the southern region of the study area. Position of line is indicated in D). C) variance map of the seismic reflector S3, the base Tertiary reflector, here the small-scale fault are clearly visible in the western region of the study area. D) position of seismic profile, L1 and L2.*

## 5.2 Morphological features

The study area is located on the Tromsøflaket, a shallow bank area, assumed to exhibit the characteristics of cold-based ice sheets. During this study several morphological features have been identified and mapped on the seafloor and URU. These show the present day and paleo continental shelf appearance.

### 5.2.1 Surface S0, the seabed

The seabed (figure 5.2-1), is mildly dipping towards north-north-east. The water depth varies between 3.4 - 4.3s TWT, which corresponds to 255 – 322m assuming a water velocity of 1500m/s.

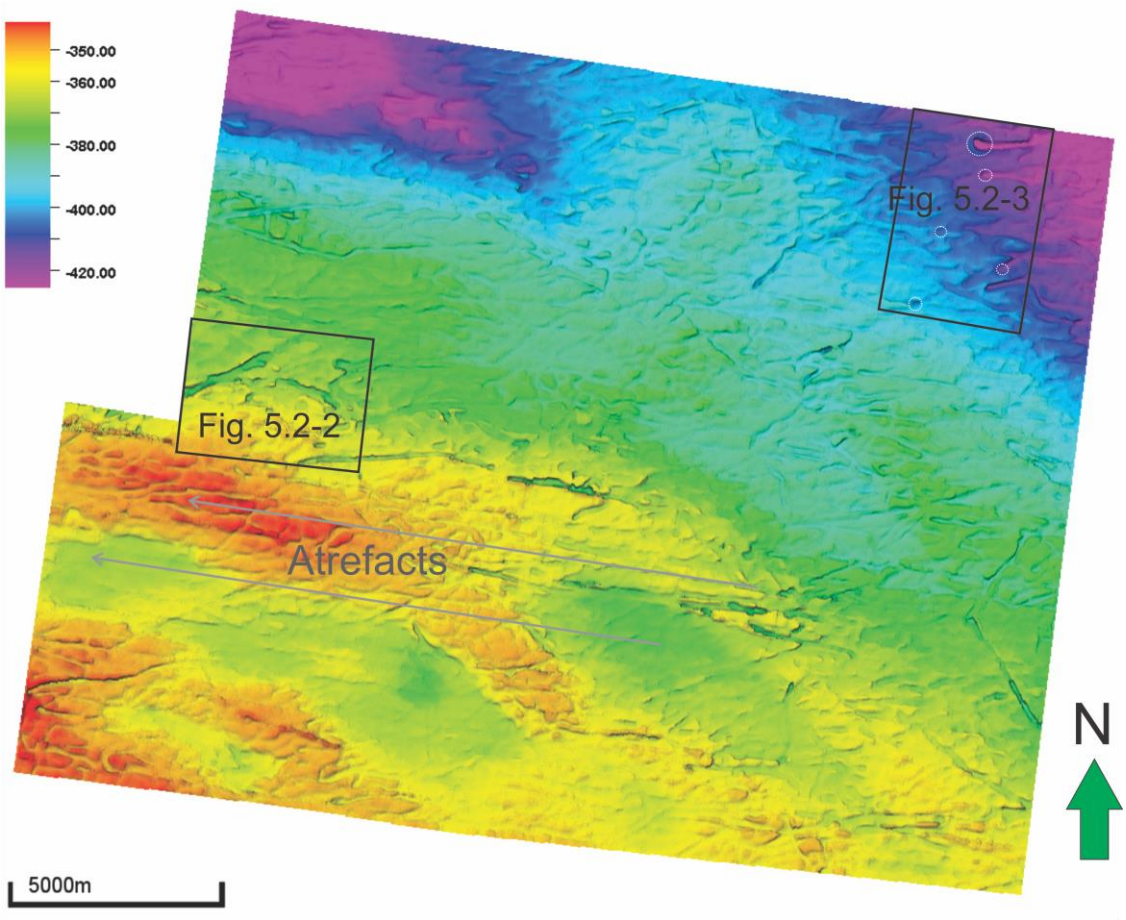


***Figure 5.2-1*** *Time relief map of the interpreted seabed horizon. Black boxes indicate position of figure 5.1-2 and 5.1-3. Direction of survey footprints highlighted by arrows. Elevation is given in TWT (ms).*

Two areas on the seabed have been selected in order to show two of the morphological features occurring on the seafloor, curvilinear furrows and sub-circular depressions.

Curvilinear furrows dominate the seabed. The orientation of the larger furrows show a slight E-W trend while the smaller ones appear random. The furrows are typically U- or V-shaped and the length varies from <1- 6km. However, due to large amount of them, their crisscrossing pattern, and the resolution of the seismic data the total length is hard to determinate. Additionally, the artefacts have the same E-W orientation and make interpretation harder. The depth ranges from <1-6m and the width from 50-225m. Figure 5.2-2 shows an example of several such features.

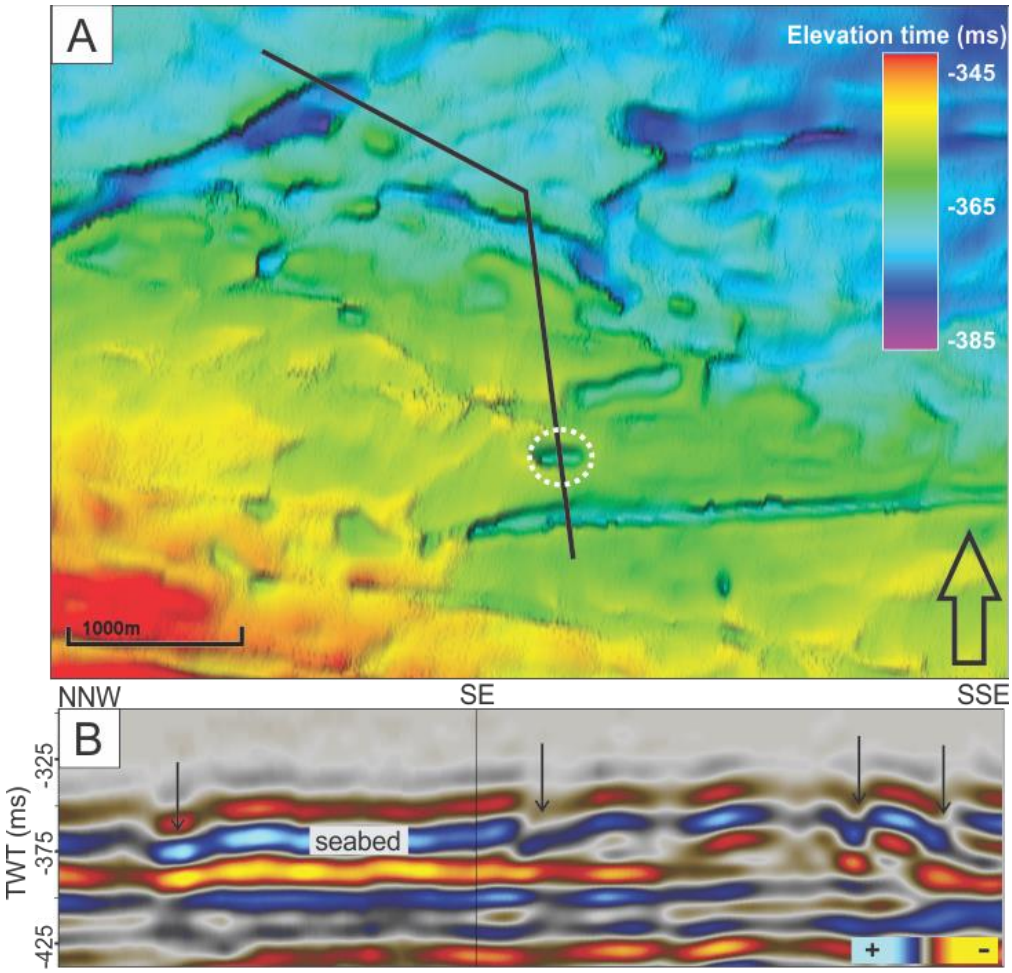


***Figure 5.2-2 A****) Map of seabed showing the elongated curved furrows. Position of A is indicated in figure 5.1-1.* ***B****) Seismic profile crossing three furrows and one circular depression indicated by arrows, the depression is highlighted with a white dotted circle in A, and similar features are discussed later in text.*

The furrows are interpreted to represent iceberg plough marks. Plough marks are formed when iceberg keels plough through seafloor sediments and are common erosional features on glaciated shelfs indicating a glaciomarine environment. The crisscrossing nature of the plough marks represent several phases of ploughing. The largest plough marks with their more linear orientation are interpreted to represent early deglaciation when movement was more constraint. Furthermore, the more randomly oriented and smaller plough marks probably relates to a later stage in deglaciation in more open-water conditions when keels were affected by wind and currents (Rafaelsen, et al., 2002; Vadakkepuliyambatta, et al., 2016).

Small circular to sub-circular depressions are identified on the seabed, these sometimes appear as isolated features, but are mostly found within the plough marks. The depth

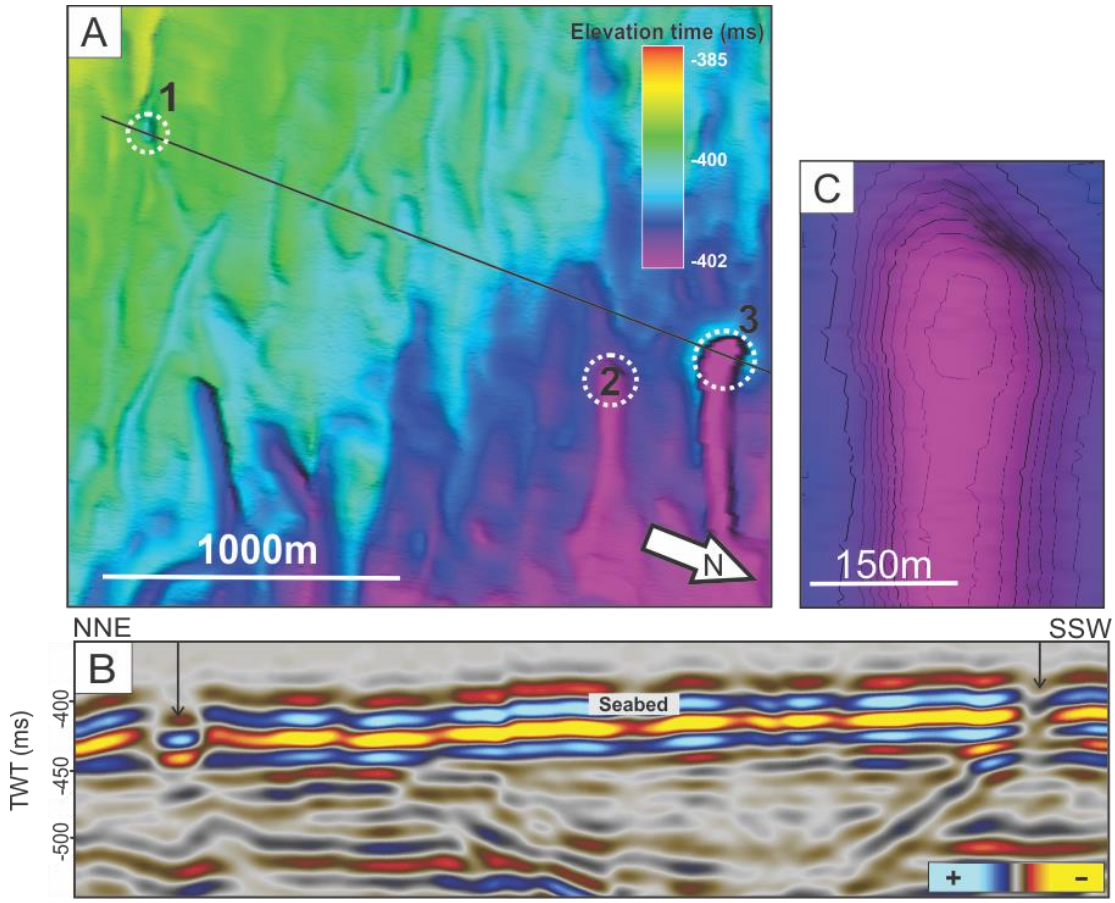


***Figure 5.2-3 A**) map of seabed plough marks and pockmarks, 3 pock marks are indicated by white dotted circles. Position of A is indicated in figure 5.1-1. **B**) Seismic line traversing pockmark 1 and 2 located within iceberg plough marks, seismic line is indicated in A. **C**) close up of pockmark 2 showing its sub-circular elongated geometry.*

generally varies between 1-10m and the width from 70-300m. Figure 5.1-3 show an example of three such features.

Similar features are located throughout the Barents Sea and the study area. These are interpreted to represent pockmarks (Løseth, et al., 2009; Chand, et al., 2012). Pockmarks are surface expressions of fluid escape, most often gas. Due to the pockmarks comparable size to the plough marks and that they mostly occur within them, age distinguishing is difficult.

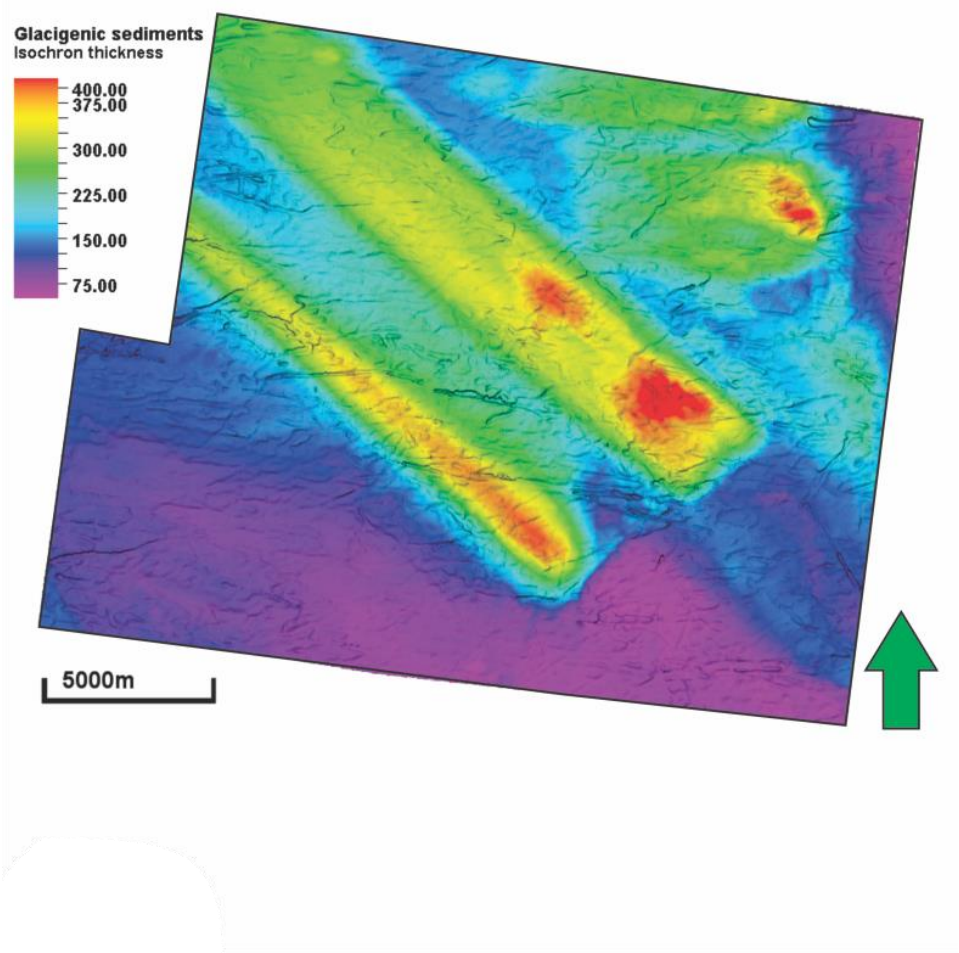


***Figure 5.2-4*** *Isochronal thickness map showing the distribution of glacigenic deposits within the study area (the thickness between the seabed and the URU). Color legend is given in ms TWT. Notice the four areas of increased deposition.*

### 5.2.2 Surface S1, the URU

The upper regional unconformity, URU, has been mapped for the whole study area (Figure 5.2-4), and is characterized by a positive reflection coefficient with varying strength and continuity. The URU is shallowest in the S-SE region of the study area where it is located at 425ms TWT and oriented parallel to the seafloor. In the southern region of the study area the URU gradually increases in depth westwards to 475ms TWT. Four elongated deep depressions are located on the URU. Within these the URU reaches depths of 800ms TWT. The depressions are the focus of the following section 5.3.

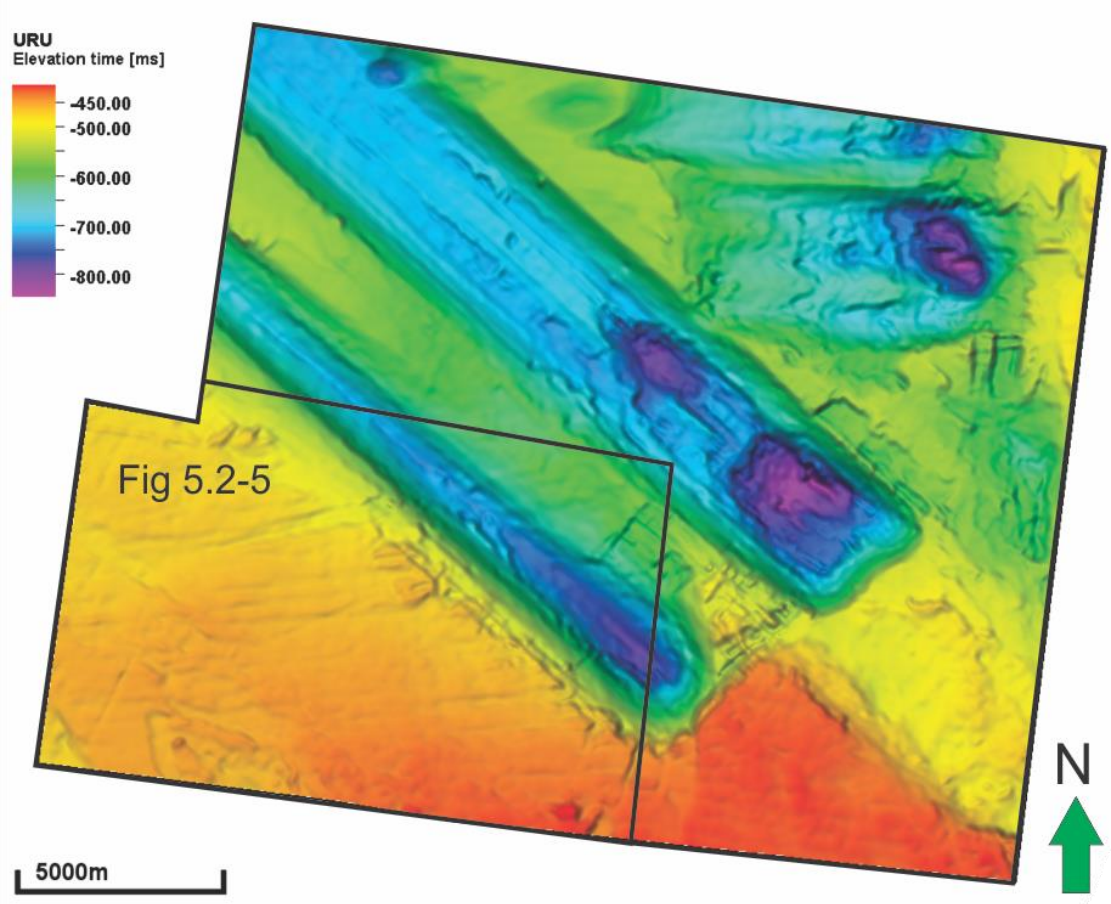


***Figure 5.2-5*** *Map of surface S1, the URU, in the study area. Figure 5.2-5 is indicated by black box. Elevation time is given in TWT (ms).*

Elongate curvilinear furrows are present in the southwestern region of the study area, (figure 5.2-5). Most of the furrows show an ENE-WSW orientation, while others appear random. The furrows can be followed up to 7km, but the seismic survey limits the measurable extent. The depth varies between 4-8ms TWT, corresponding to 3.5-7m (v=1750m/s), and the width from 100-400m. These features are similar to those on the seabed, and interpreted as furrows.

Notice the different orientation between the plough marks and the large elongated depressions.

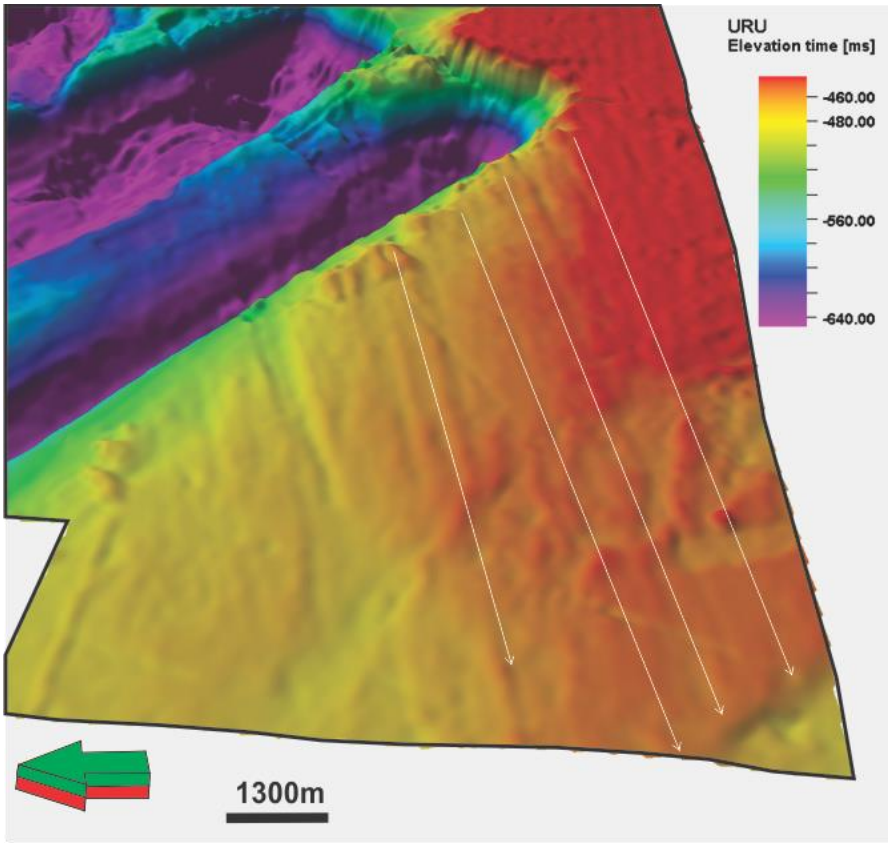


***Figure 5.2-6*** *Plough marks on the URU, 3D view. White arrows indicate the orientation of the geomorphologic features. Location of figure is indicated in figure 5.2-4.*

The URU represent the boundary between glacigenic deposits of Pliocene-Pleistocene age, and underlying sediment of Tertiary age and older. An isochron thickness map (Figure 5.2-6) illustrate the thickness of glacigenic deposition within the study area. In the areas where the URU is closely parallel to the seabed the thickness of the glacigenic sediments varies between 75-150ms TWT, corresponding to a thickness of 65.63-262.5m (Vp= 1750m/s). Within the depressions, the thickness is far greater.

## 5.3 Elongated depression on the URU

Four large elongated depressions are located on the interpreted URU within the study area

(Figure 5.3-1). Figure 5.3-2 illustrates the interpreted URU surface, and the annotation for the depressions. The following sections will describe their size, geometry and infill.

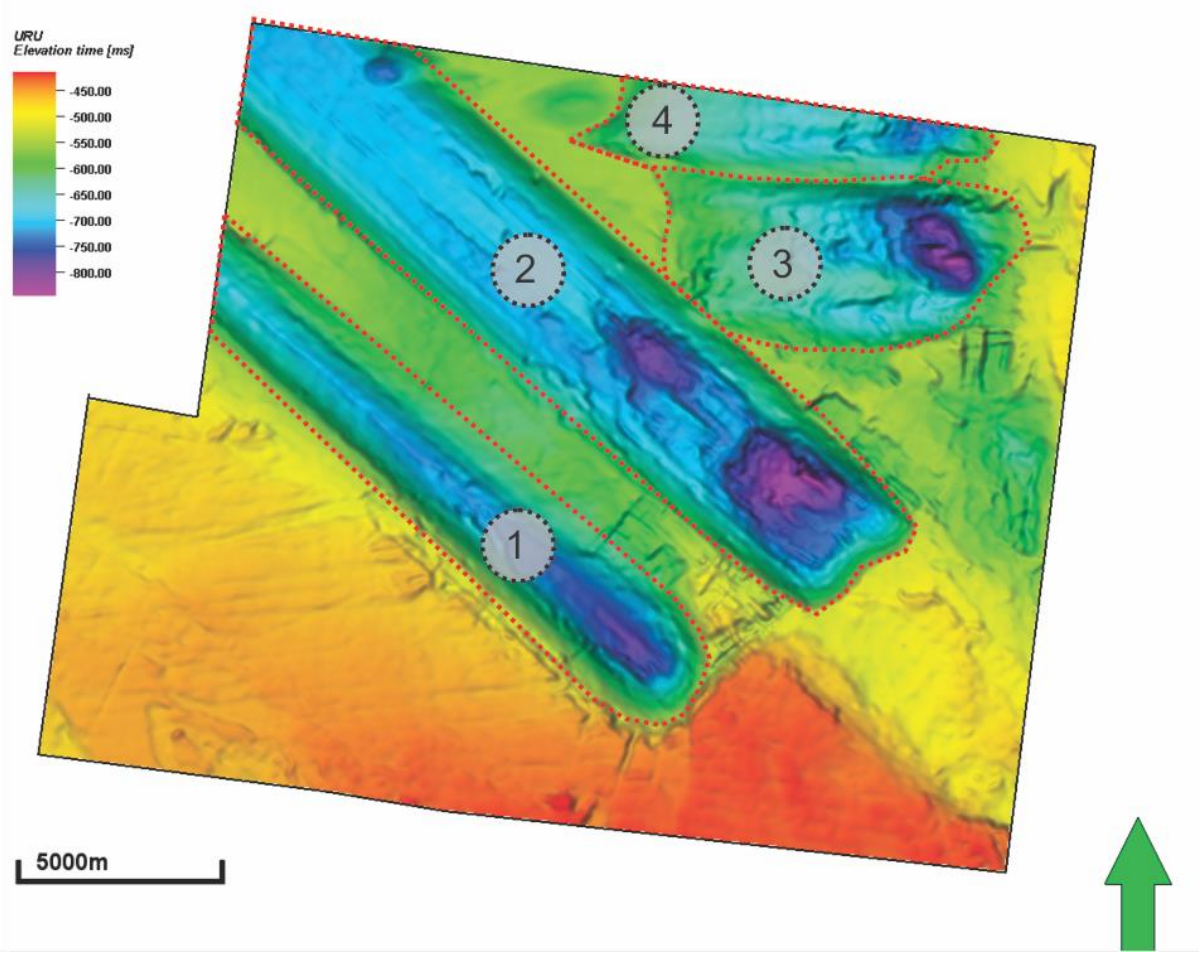


***Figure 5.3-1*** *Map showing the interpretation of surface S1 and four elongated deep depressions. Numbers indicates annotation used for the following sections.*

## 5.3.1 Depression 1

Depression 1 has a total length of 15256m and has a NW-SE orientation. However, the total length is limited by the 3D seismic data. The depression deepens and thickens towards SE. The depth varies between 302.452ms TWT in the west to 445.909 ms TWT in the east, corresponding to a depth decrease from 264.64-390m below seafloor, and a drop of 133.4-259m from the surrounding more parallel URU. Moreover, the depression is widest in the east with 3800 m and narrows westwards to 2832m. In total the depression covers an area of 37.7039km$^2$.

The depression is characterized by a strong reflection, with a well-developed floor and flanks resembling a U-shape. The southwestern flank is the steepest while the northeastern has a gentler slope towards depression 2. In addition, the elongated depression show a clear linear trend. The southeastern end of the depression is marked by an abrupt steep slope, whereas the other end of the depression is not within the study area. The floor appears as a relatively smooth surface, but becomes more irregular towards the deepest point. Amplitude appear stronger on the floor compared to the flanks, and anomalies are recorded (Figure5.3-2).

The infilled Plio-Pleistocene sediments seem to be divided into three different units based on two strong reflections identified (figure 5.3-3). Unit 1 is characterized by weak/chaotic reflections dipping from the southeastern end-flank towards the depression floor. The upper limit of unit 1 shows a strong negative amplitude. Unit 2 is closely parallel to the floor and mostly exhibit a chaotic reflection configuration. However, layered sediments can be recognized in the northwestern region where the seismic data limits the depression. Unit 2 onlaps unit 1 in southeast. The upper boundary of unit 2 is a strong reflection with a negative reflection coefficient. It is highly discontinuous and irregular, and has a step-like form. Unit 3 has the same structureless facies as unit 2, and its upper boundary marks the extent of the infilled sediments. The total thickness of infilled sediments is approximately 300m at the deepest point within depression 1.

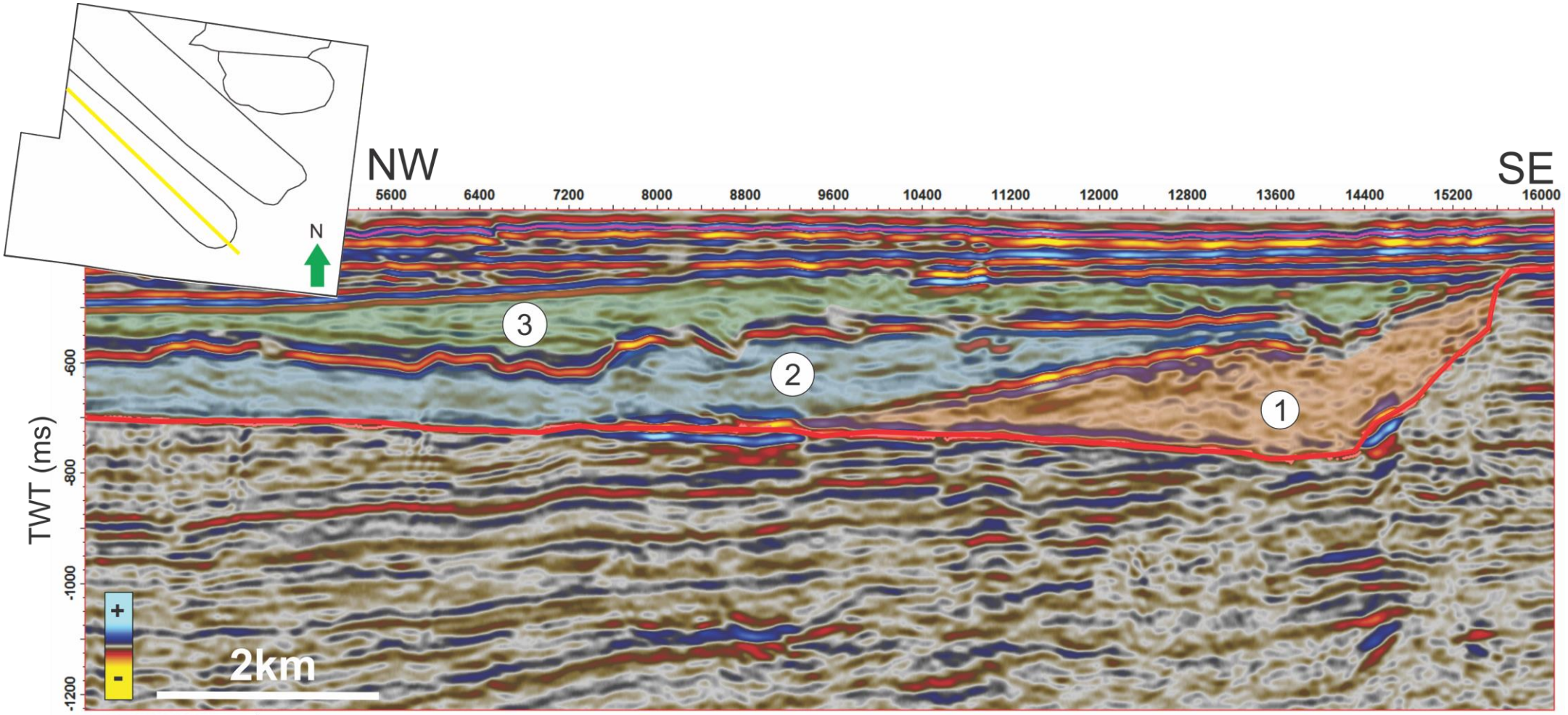


***Figure 5.3-2*** *Seismic line showing the side view of depression 1. The depression seem to be divided into three units, all have a chaotic reflection configuration, notice the highly irregular boundary between unit 2 and 3 and the abrupt steep end-flank in SE. The red line indicate the interpreted URU horizon. Location of seismic line is indicated in the upper left corner.*

### 5.3.2 Depression 2

Depression 2 covers an area of 67.8001 $km^2$ and is the largest feature. The width is relatively constant along the depression with 4249m, and the length is 195000m. As with depression 1, depression 2 has the same NW-SE orientation, and the total length of the feature is limited by the available data. The depth shows the same trend as depression 1, and gradually decreases from 270-404.685ms TWT (236.25-390m) below the seabed. Within the depression two sub circular areas of increased depth is recorded. The north westernmost reaches 357m below the seafloor, and the south eastern 390m.

The depression is located parallel to depression 1, shows the same straight geometry in map view, and has well-developed floor and flanks. In contrast to depression 1, the floor in depression 2 is flatter and wider. Along the floor, two overdeepened basins are recorded, and the floor becomes more irregular in this region compared to the smooth surface in the northwestern region. As with depression 1, the southeastern extent is marked with an abrupt steep slope.

The Plio-Pleistocene succession within depression 2 is divided into two units, where the lowermost, unit 1, by far is the largest (figure 5.3-3). Unit 1 shows the same facies appearances as unit 2 within depression 1. It is highly chaotic and seem structureless where the floor is deepest. Further to the northwest weak stratification is observed. Unit 2 is located near the southeastern end of the depression and is of limited extent. The infill do not show any apparent trends. The upper limit of unit 1 is represented by a negative reflection coefficient and varies greatly in strength. In the areas where it separated unit 1 and 2 the amplitude is strong, otherwise it is weak. Where the amplitude is strong a similar step-like appearance as the reflection separating unit 1 and 2 in depression 1, can be recognized. The total sedimentary infill has a maximum thickness of 272.4 m in the southeastern region of the depression

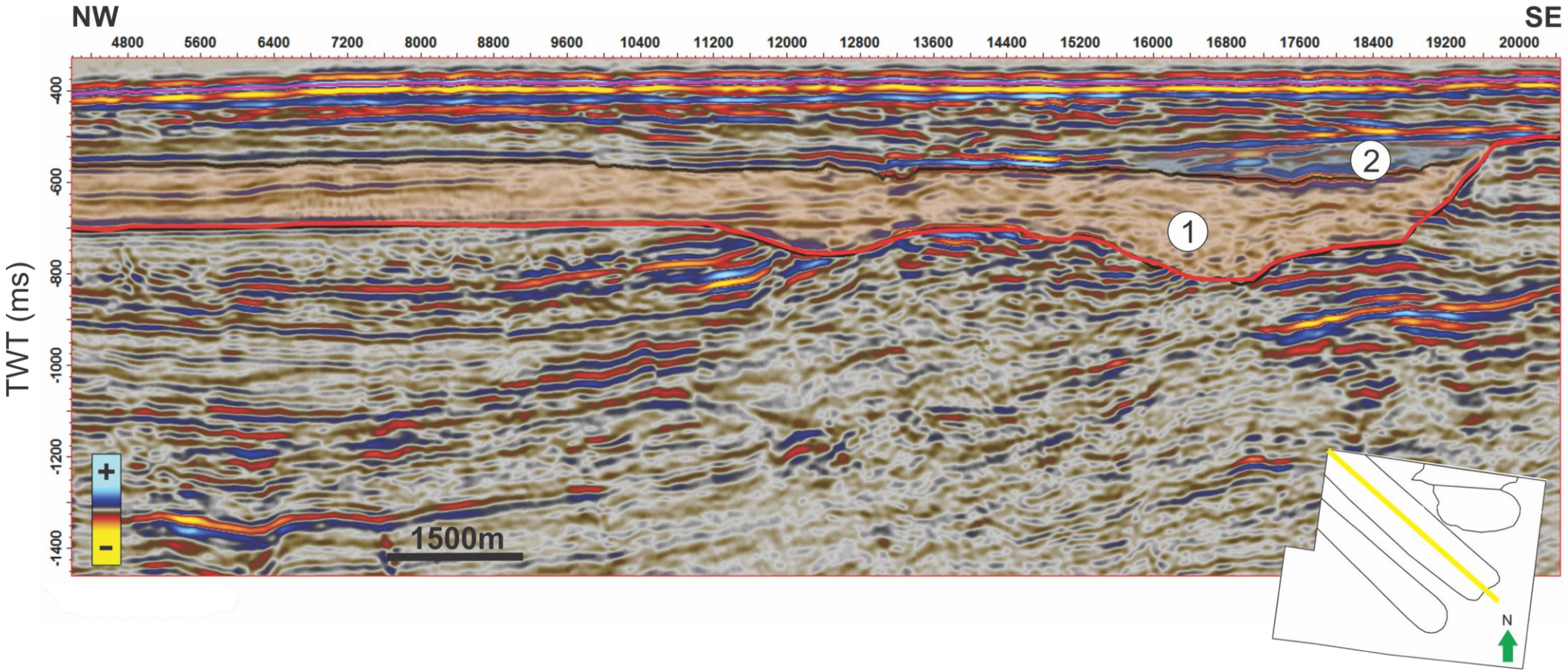


***Figure 5.3-3*** *Seismic line showing the side-view of depression 2 and its sedimentary units. The red line marks the interpreted URU horizon, and the black line the boundary between unit 1 and 2. The transparent color in the units do not relate to the colors used for describing the other depressions in previous and following figures. Location of seismic line is indicated in lower right corner.*

### 5.3.3 Depression 3 and 4

Depression 3 and 4 are located in the northeast region of the study area. These are closely spaced but a prominent ridge separates the two, and thereby they are interpreted as individual features. The full extent of depression 4 is limited by the available 3D survey, and recorded measures only tell us something about the feature's shape and size within the study area, and not its geological true expression. Depression 3 and 4 covers an area of respectively 23.2541km$^2$ and 12.2623km$^2$, has a maximum width of 3954m and 1852m, and a length of 8658m and 9160m.

In contrast to depression 1 and 2, these have an E-W orientation and a much shorter length. They also have a more sub-circular shape, hence larger width to length ratio. See table 5.3-1 for summary of the characteristics for all four depressions. Depression 3 and 4 have well-developed irregular floors and flanks, and deepen towards east. The eastern extent is, as with the other depressions, marked with an abrupt steep slope. The western termination is marked with a gentler slope (figure 5.3-4).

The sedimentary infill show the same chaotic/transparent reflection configuration identified within depression 1 and 2 and two units are identified. The lowermost unit, unit 1, is mostly found within depression 3, where it is located in the deepest part. Within depression 4, unit 1 is relatively thin and has a constant thickness. Unit 2 show the same trend as all the other units described within the depressions and thickens towards deepest point along the depressions. Maximum thickness of sediment infill in depression 3 is 217 m and in depression 4 reaches 157.5m. The boundary separating unit 1 and 2 is characterized by a continuous weak reflection with a negative reflection coefficient.

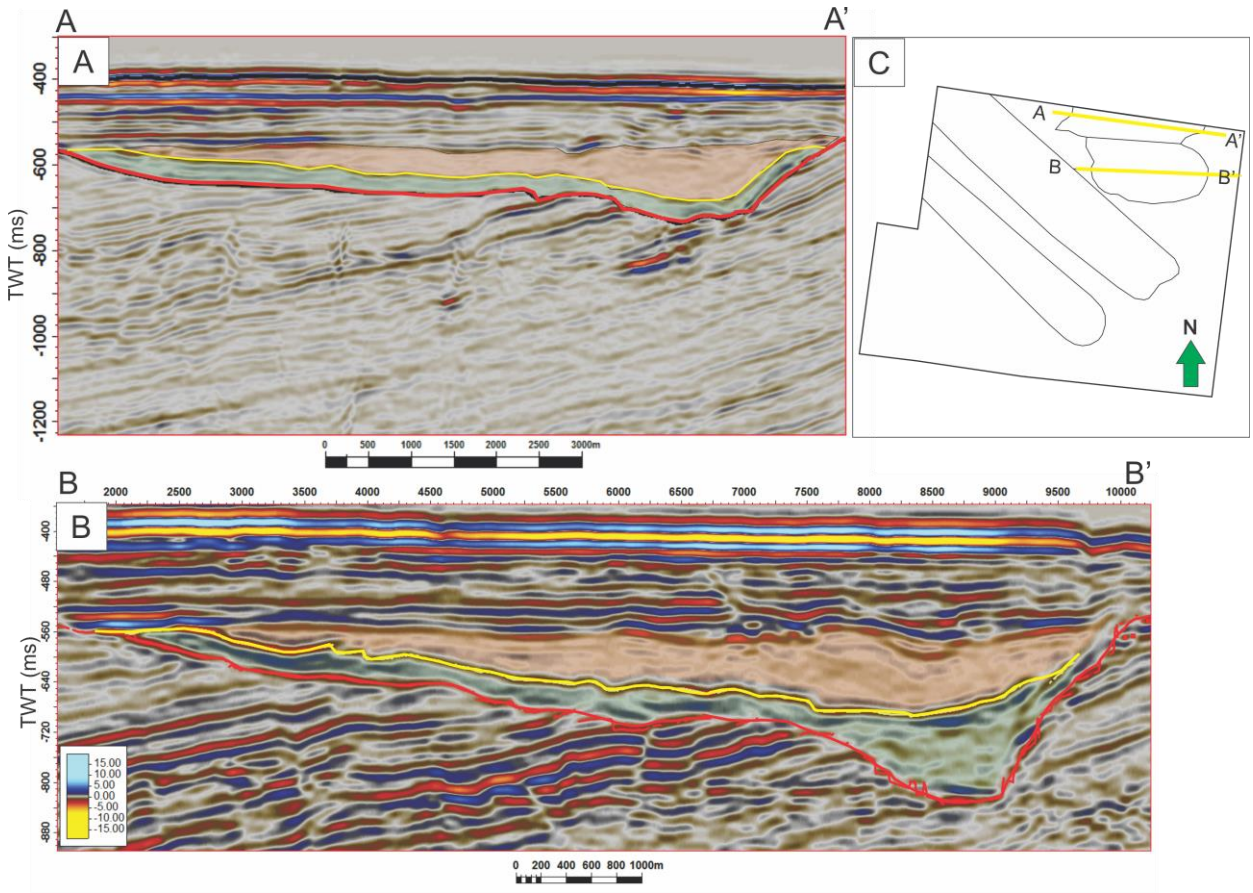


***Figure 5.3-4*** *A) seismic line traversing depression 4. B) seismic line traversing depression 3. Unit 1 is highlighted with green transparency and unit 2 with orange. Depression floor/URU is marked by red line, and boundary separating unit 1 and 2 by yellow line. Location and orientation of seismic lines is indicated in C).*

### 5.3.4 Summary

The measurable depression features have been gathered in Table 5.3-1.

All of the described depressions show similar characteristics. They all have well-developed floors and flanks, an abrupt steep slope in the SE-E end, and show deepening towards this end. Depression 3 and 4 however differs in orientation and size. Since the northwestern extent of depression 1 and 2 is located out of the 3D seismic survey, comparison of the NW-W terminations are impossible.

None of the identified depressions show any topographic expression on the seabed (figure 5.2-1), hence they are completely infilled. Two seismic infill-facies are identified. The most abundant, occurring in all depressions, is describable as transparent/chaotic with low amplitude reflections. For depression 1 and 2, a change in seismic character from chaotic to weakly stratified low amplitude reflections are observed in the northwestern area. The infilled sediments are easily distinguishable from the overlying high-amplitude stratified sediments and the underlying truncating strata.

***Table 5.3-1*** *Summary of the main measurable characteristics for the four depressions identified on the URU.*
**measurements for depression 4 are not directly relatable to the other depressions since its extent is limited by the seismic data available.*

| **Depression** | **Length (m)** | **Width/long axis (m)** | **Area ($km^2$)** | **Max depth below seabed (ms TWT)** | **Depth (m, $V_p$ =1750)** | **Orientation** | **Width/length** |
|---|---|---|---|---|---|---|---|
| 1 | 15256 | 3800 | 37.7039 | 445.909 | 390 | NW-SE | 0.25 |
| 2 | 19500 | 4249 | 67.8001 | 404.685 | 354 | NW-SE | 0.22 |
| 3 | 8658 | 3954 | 23.2541 | 418.289 | 366 | E-W | 0.45 |
| 4 | 9160* | 1852* | 12.2623* | 324.476* | 283* | E-W | 0.2* |

## 5.4 Amplitude anomalies

Several amplitude anomalies are recorded at different stratigraphic levels within the study area. However, the most apparent ones are observed along the Tertiary surface S2 and in the proximity to the URU depressions.

Description and extent of the amplitude anomalies are based on RMS attribute maps and seismic cross-sections. The observed anomalies serve the purpose of illustrating possible fluid migration paths within the study area.

### 5.4.1 Tertiary amplitude anomalies along S2

S2 is characterised by a negative reflection coefficient with varying amplitude strength. Figure 5.4-1 illustrates the lateral extent of the amplitude anomalies, by use of the RMS amplitude attribute. Three seismic crosslines have been chosen to study the anomalies further.

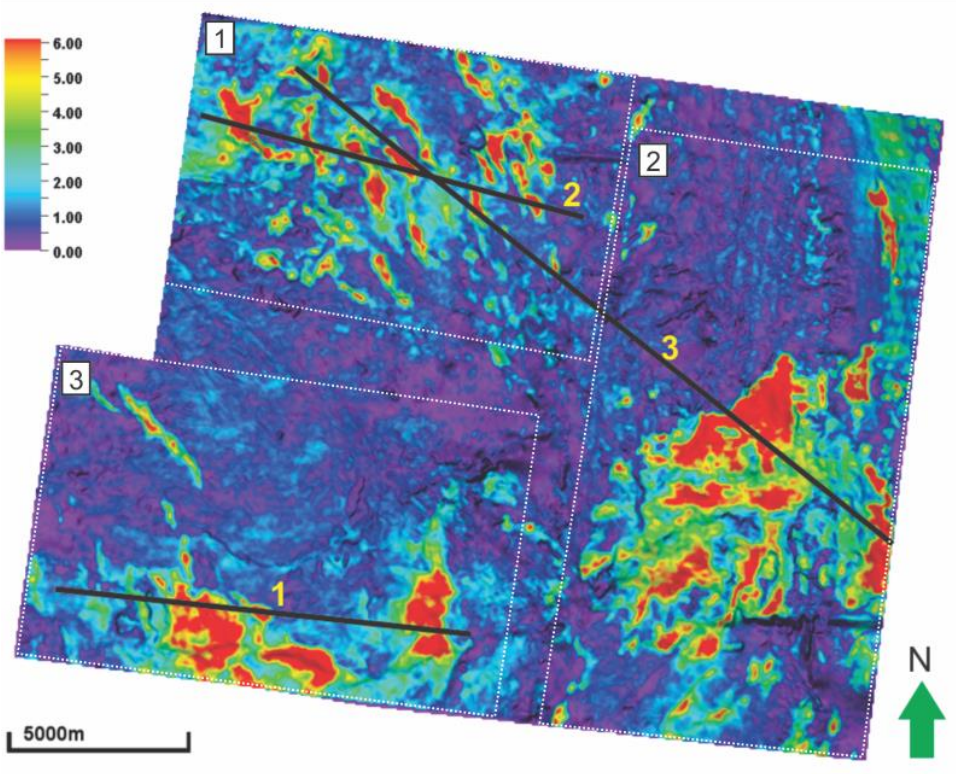


***Figure 5.4-1*** *RMS amplitude map of surface S2 (horizon offset and search window both zero). three seismic lines are highlighted by black lines and yellow numbers. Regions indicated by white boxes with numbers. Southwestern – 3, Northwestern – 1, and Southeastern – 2.*

To document the distribution and characteristics of the amplitude anomalies, the study area is divided into three regions: southwestern, northwestern and southeastern.

#### 5.4.1.1 Southwestern region

In the southwestern region of the study area large sub-circular amplitude anomalies dominate. These anomalies are characterised by a strong negative amplitude. The longest axis measures 2300-4000m and the shortest varies from 1050-1762m, figure 5.4-1. In addition to the sub-circular anomalies an elongated anomaly are also identified is the westernmost extent of the region. The elongated anomaly have the same geometry and characteristics as those identified in the northwestern region. These are interpreted in the following section, 5.4.1.2.

Seismic line 1, indicated in figure 5.4-1, travers the largest of the anomalies (Figure 5.4-2). Above the anomaly some of the reflectors exhibit increased amplitude strength, but not to the same extent as the mapped anomaly. Beneath the bright anomaly, an area with enhanced reflectivity is identified within the Tertiary unit. Below this, a vertical zone of acoustic masking is recorded. This zone can be followed down to the underlying S4, Top Kolje Formation, and is without difficulty identified along the faulted base Tertiary reflector, S3. Pull-downs can be identified from the upper zone of enhanced reflectors all the way down to the Top Kolje Formation. Depths below the Top Kolje Formation have increasingly bad resolution, making total vertical extent of the feature hard to determinate.

Based on the identified vertical zone of acoustic masking, the pull-downs and the bright upper reflection, the anomaly is interpreted to represent a gas chimney. The vertical zone of acoustic masking represents gas migrating vertically from stratigraphic levels beneath the Top Kolje reflector through the faulted base Tertiary reflector and into Tertiary strata. This theory is further enhanced by the identified pull-downs. The upper zone with heightened reflection strength is thought to signify gas accumulating close to S2 and further migration laterally in permeable carrier beds towards east. However, continued vertical migration through S2 cannot be disregarded.

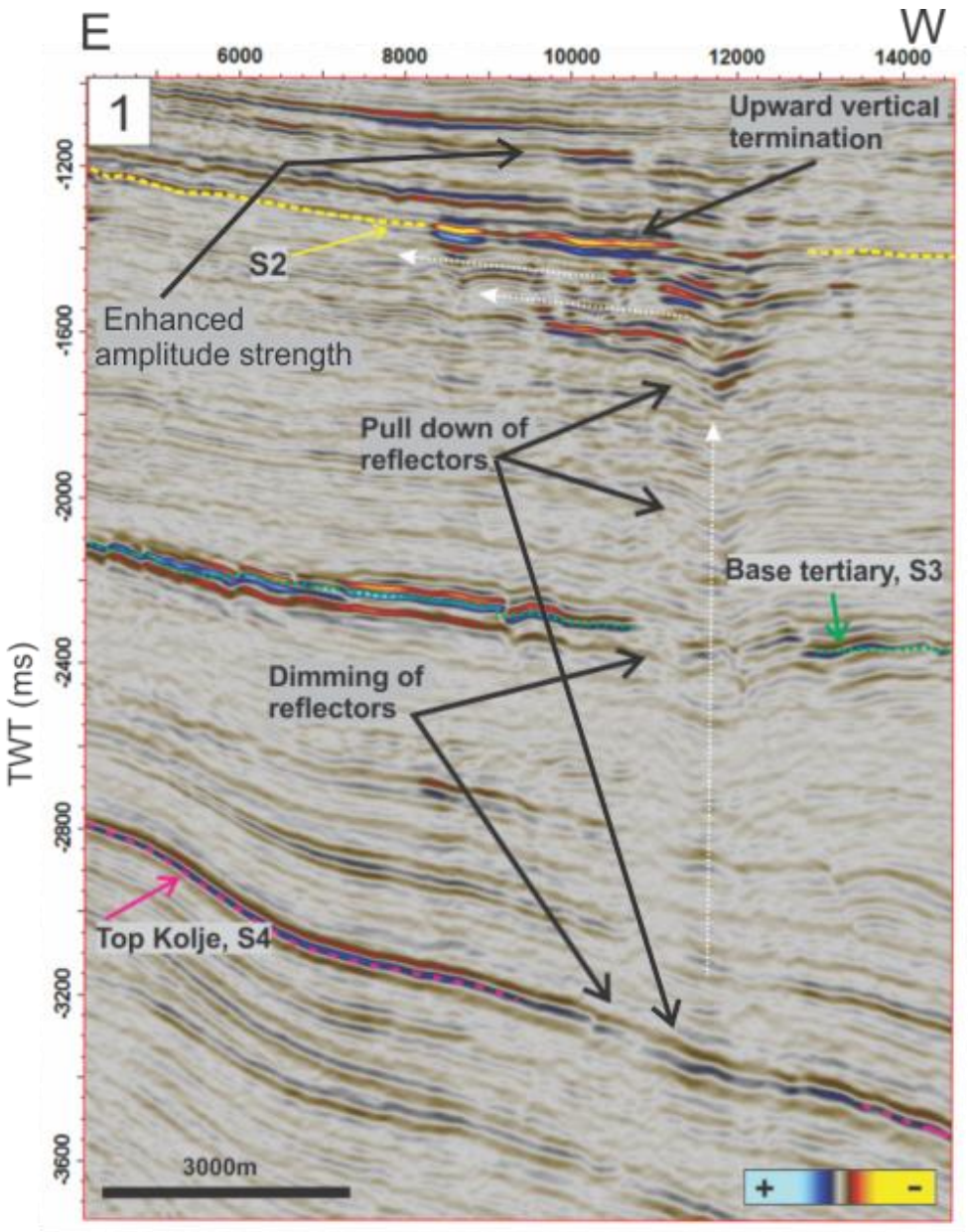


***Figure 5.4-2*** *seismic profile crossing over the amplitude anomaly within the southwester region. Location profile is indicated in figure 5.4-1. White arrows suggest fluid migration pathway. See text for detailed description.*

### 5.4.1.2 Nortwestern region

The northwestern region of the study area is characterized by elongated NW-SE striking negative amplitude anomalies and smaller sub-circular individual features. Some of the elongated anomalies have curved expressions. The longest axis of the elongated anomalies measure 0.85-3km. The shortest axis varies from 300-700m. The smaller more oval shaped anomalies have lengths varying from 300-400m and their width varies between 150-380m.

Seismic line 2, indicated in Figure 5.4-1, crosses over five of the anomalies (figure 5.4-3). Beneath four of the anomalies, stacked reflections with apparent pull-downs are observed in the Tertiary unit. These reflections have a strong vertical amplitude response leading up to the termination in S2. Laterally the strength diminishes quickly towards northwest. However, continued upslope prolongation to southeast is identified. The southeasternmost anomaly is represented by an individual bright spot, and do not have stacked strong reflection leading up to it. Further down in the Tertiary sequence the stacked reflections loses all its strength and along the base Tertiary reflector, S3, dimming occurs. Above the strong negative anomalies sparse enhancement of the reflectors can be identified.

Based on the anomalies geometry, the stacked strong reflectors, observed pull-downs and dimming located in deeper stratigraphic units the amplitude anomalies are interpreted to be gas migrating through tertiary faults terminating in S2. The stacked amplitude anomalies represent fluid migration through the fault plane, and into permeable carrier beds besides it. S2 represent the upper vertical termination of the migrating gas. Since S2 shallows towards southeast buoyancy will direct migration in this direction. The stand-alone bright spot is interpreted to be a result of this lateral migration. Dimming along the base Tertiary reflector, S3, could represent gas being sourced from deeper stratigraphic levels, and the faulted nature of S3 enhance the theory that fault planes in this region act as conduits for fluid migration.

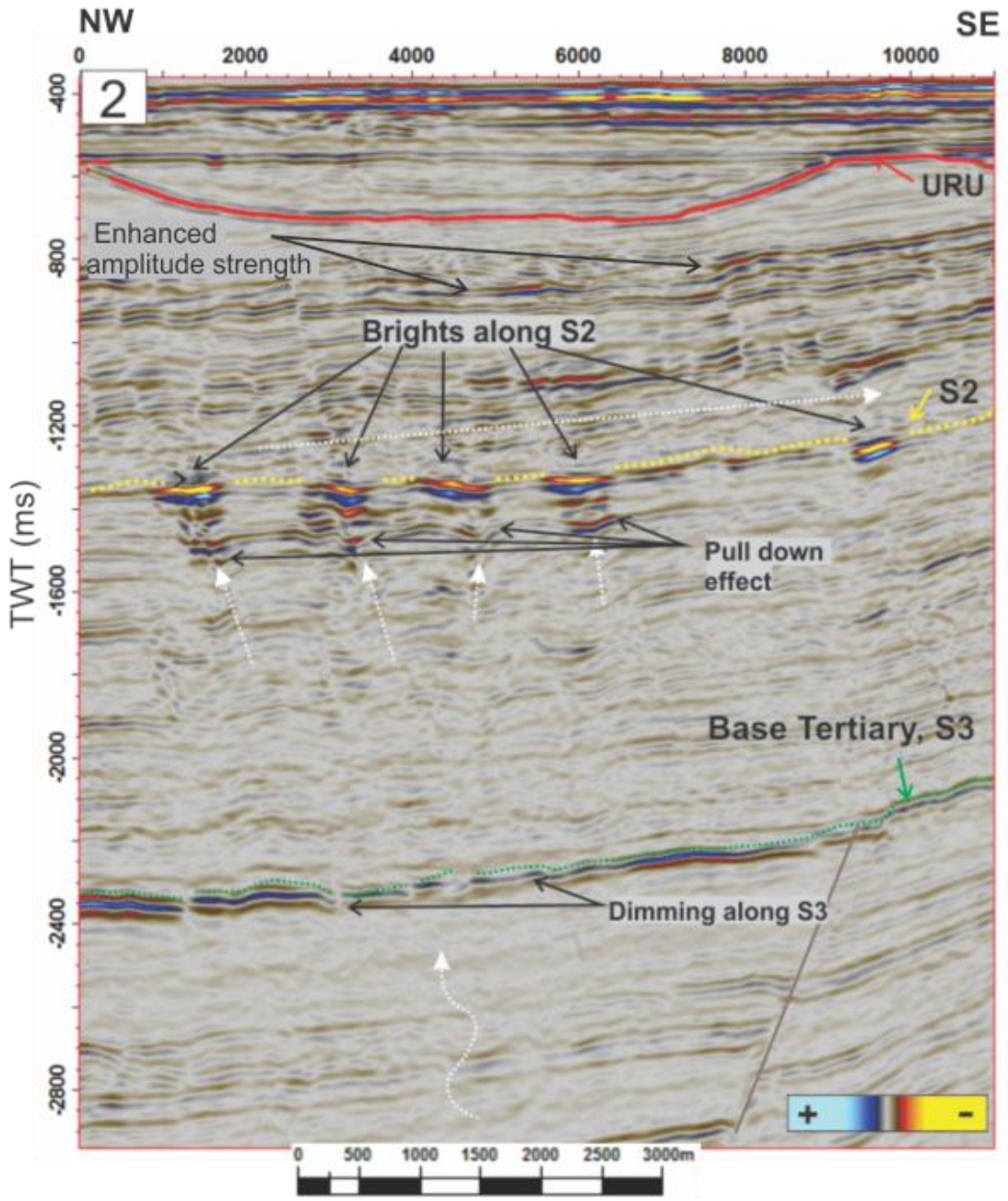


***Figure 5.4-3*** *seismic profile crossing over the amplitude anomalies within the northwestern region. Location profile is indicated in figure 5.4-1. White arrows suggest fluid migration pathway. See text for detailed description.*

### 5.4.1.3 Southeastern region

In the southeastern region of the study area negative amplitude anomalies occur in various shape and sizes. Some are elongated and show an N-S orientation, while others are sub-circular. The longest axis varies between 200-4000m, and the short axis between 130-1600m.

Seismic line 2, as seen from figure 5.4-1, crosses the largest of the southwestern anomalies (figure 5.4-4). The anomaly is characterized by a relatively wide lateral zone of stacked reflectors with enhanced strength. Beneath the anomaly, an area of acoustic masking is identified. An interesting observation is its location directly beneath depression 2.

Interpretation of the anomaly is difficult due to the poor quality of the seismic data west of fault F1. This makes it hard to determine the faults extent in the Tertiary sequence, and possible amplitude anomalies in relation to the faults. However, based on the amplitudes bright expression similar to the other anomalies located within the study area, it is interpreted to be a result of migrating gas. The north westernmost bright spots in figure 5.4-4 have previously been interpreted to be gas migrating through Tertiary faults and laterally towards east (figure 5.4-3). The anomaly in the southeastern region could hence represent a continuation of this lateral migration. Surface S2 shallows towards east and in the region where the anomaly is located, the slope has a smaller gradient. This reduction in up-dip angle could be enough to increase the critical hydrocarbon column needed for continued migration, and create a gas accumulation. It is also possible that the deep-seated faults, F1 and F2 act as

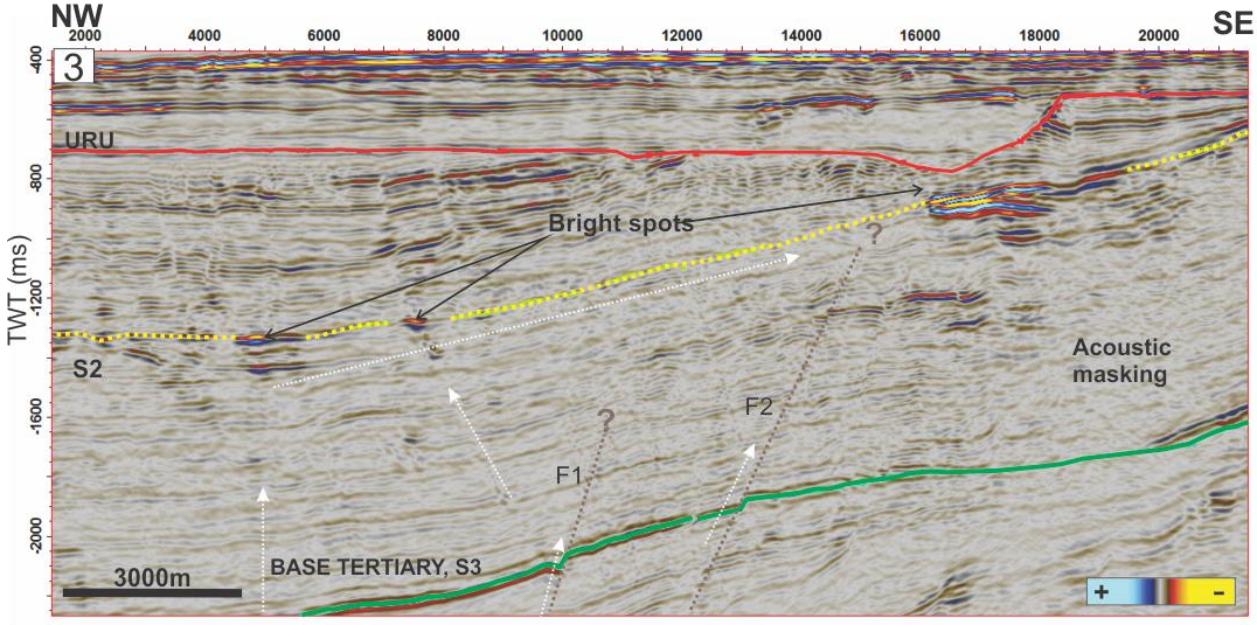


***Figure 5.4-4*** *seismic profile crossing over the amplitude anomalies within the southeastern region. Location profile is indicated in figure 5.4-1. White arrows suggest fluid migration pathway. See text for detailed description.*

vertical conduits for gas entering tertiary strata, and the anomalies location just east of F2 could indicate this.

### 5.4.2 Amplitude anomalies below the URU depressions

To study potential amplitude anomalies related to the identified depressions in section 5.3, a RMS map extracting amplitudes from the URU to a horizontal surface 480ms TWT below the interpreted seabed have been made (figure 5.4-5). Amplitude anomalies below the URU appear in groups but show no apparent orientation or distinct shape. The largest anomalies have long axis varying from 1400m to 6300m for the longest anomaly observed within depression 1, whereas the short axis for these anomalies range from 450-1900m. The highest density of anomalies is located in the eastern region of the study area and within the depressions. Amplitude anomalies appearing as vertical parallel lines with an S-E orientation

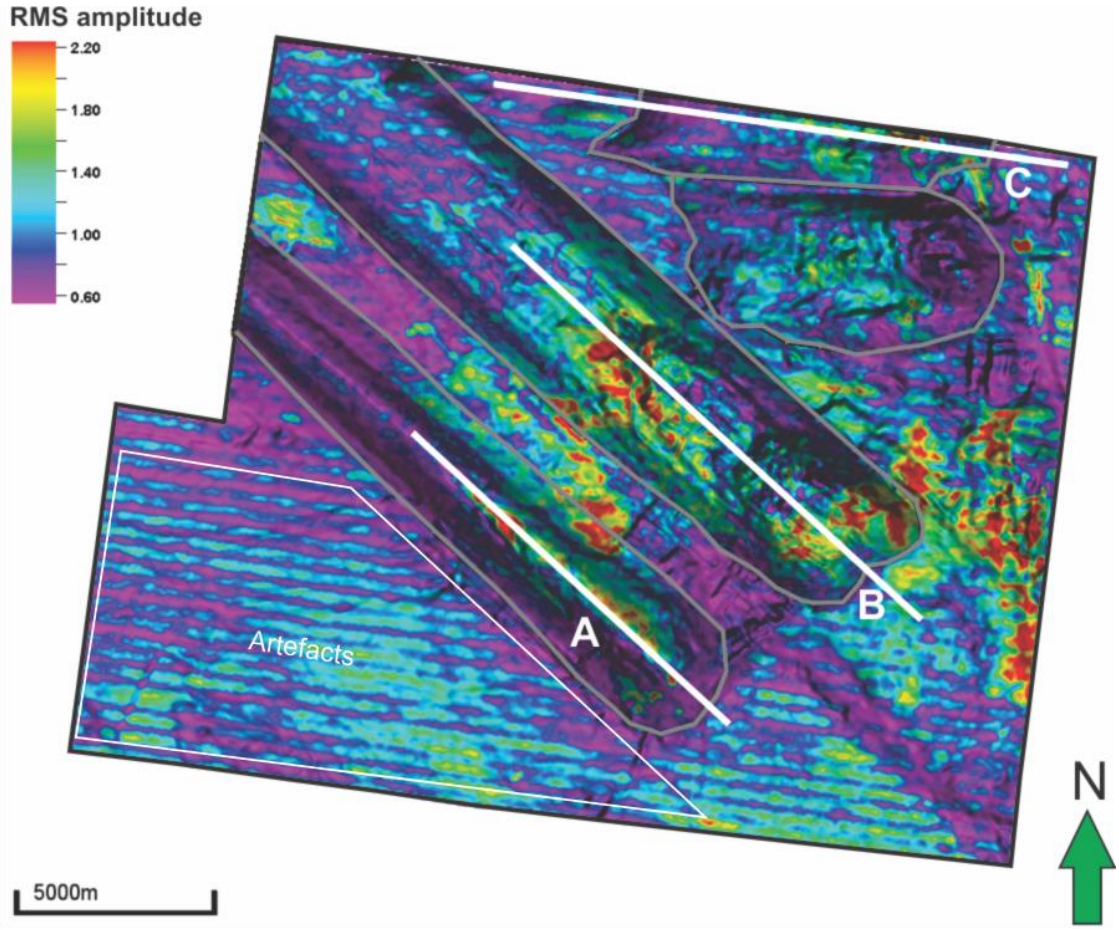


***Figure 5.4-5*** *RMS amplitude map, amplitude values extracted from interval between the URU to a horizontal surface 480ms TWT below the seabed. Grey polygons indicate the interpreted extent of depression 1,2,3 and 4. White lines (A,B and C) indicate position of seismic profiles in figure 5.4-6. Artefact are indicated in the lower left corner.*

is identified throughout the map, these are interpreted to be artefacts and excluded from the study.

Three seismic cross-sections A,B and C, position indicated in figure 5.4-5, are used to investigate the anomalies further.

Seismic cross-line A is located within depression 1, and traverse the longest anomaly recorded on the RMS map. This anomaly is positioned along the depression floor, and characterized by a strong negative reflection coefficient. In the deepest part of the depression, a single bright spot appear in front of the elongated anomaly. Below the bright spot, within tertiary strata, pull-downs are observed and the fault plane of fault F1 can be traced up to this point. Between the pull-downs and the bright spot, a vertical trend of increased reflectivity is identified, see figure 5.4-6 (A).

Seismic cross-line B is located within depression 2, and crosses the two small basins along the depression floor. Seismic profile C cross depression 4. In both of the profiles amplitude anomalies are located west of the deepest parts of the depressions. The amplitude anomalies is associated with stata subcropping the erosional unconformity, and is characterized by a negative reflection coefficient, figure 5.4-6 (B,C).

The elongated negative anomaly along the floor of depression 1 could represent a lithological boundary between glacitectonic hard material and softer sediments in the upper tertiary succession. Another possible explanation for the negative anomaly could be gas migrating laterally upwards in permeable carrier beds which truncates the deepest parts of the depression. The location if the isolated bright spot vertically above the fault, the observed pull-downs and enhanced reflectivity indicate gas migration along fault F1 from deeper strata. However, due to limiting quality of the seismic data, the vertical extent of fault F1 is hard to determinate hence interpretation becomes uncertain.

The amplitude anomalies occurring within depression 2 and 4 is interpreted to represent gas migrating laterally towards east in the upper tertiary sequence. The URU would represent a surface with sealing capability, hence trapping gas in the beds truncating the depressions.

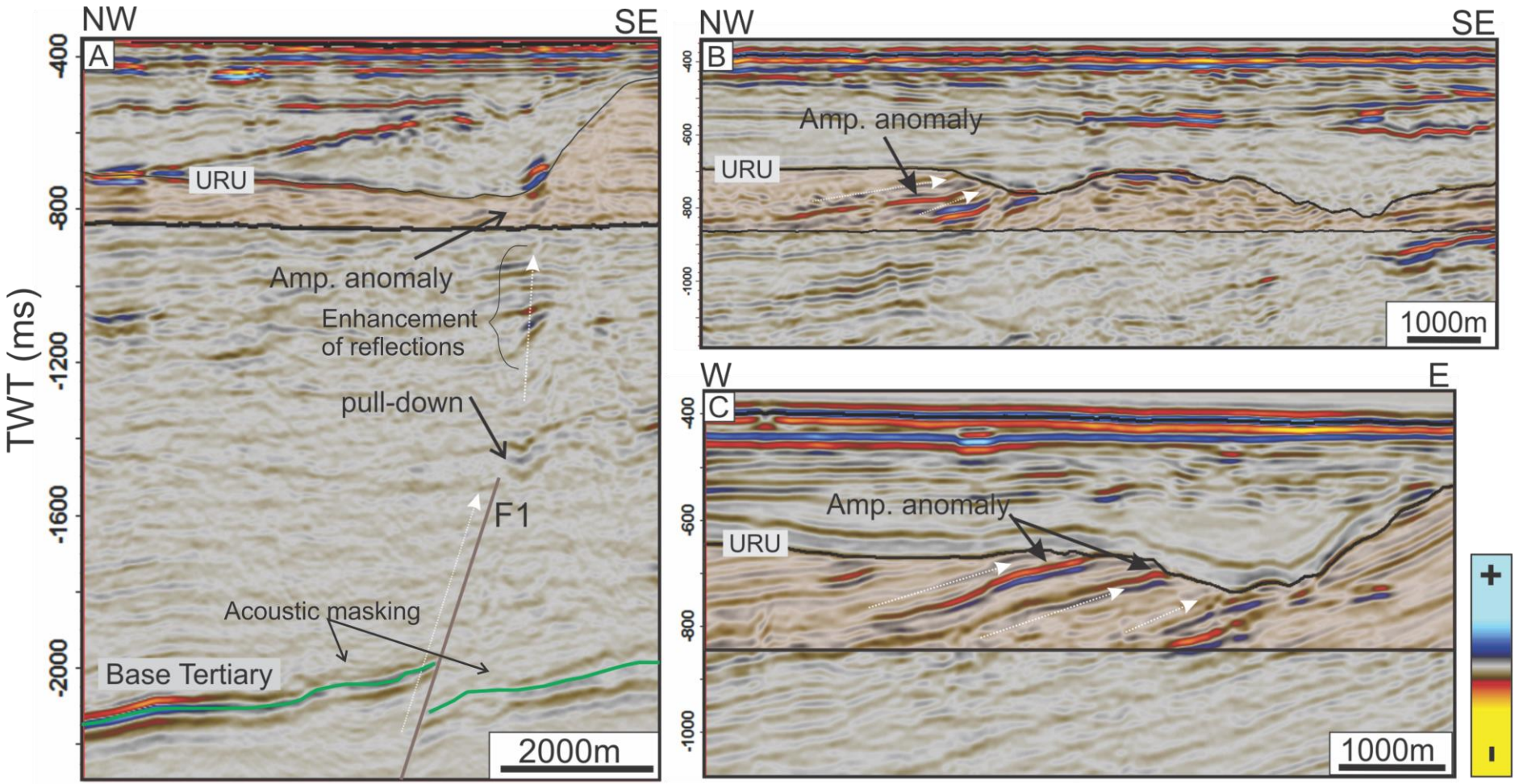


***Figure 5.4-6*** *Three seismic sections (A, B and C) crossing through amplitude anomalies below the URU, location of lines are given in figure 5.4-5. Orange shaded area represent the RMS interval between the URU and the horizontal surface 480ms TWT below the seabed. White arrows indicate suggested fluid migration pathways.*

## 5.5 Summary results

The main results produced for this thesis are gathered in figure 5.5-1. The deep-seated faults F1 and F2, the western small-scale faults, amplitude anomalies within the Tertiary succession and the four depression on the URU make up the basis for further discussion related to fluid migration within the study area and possible mechanisms responsible for formation of the depressio

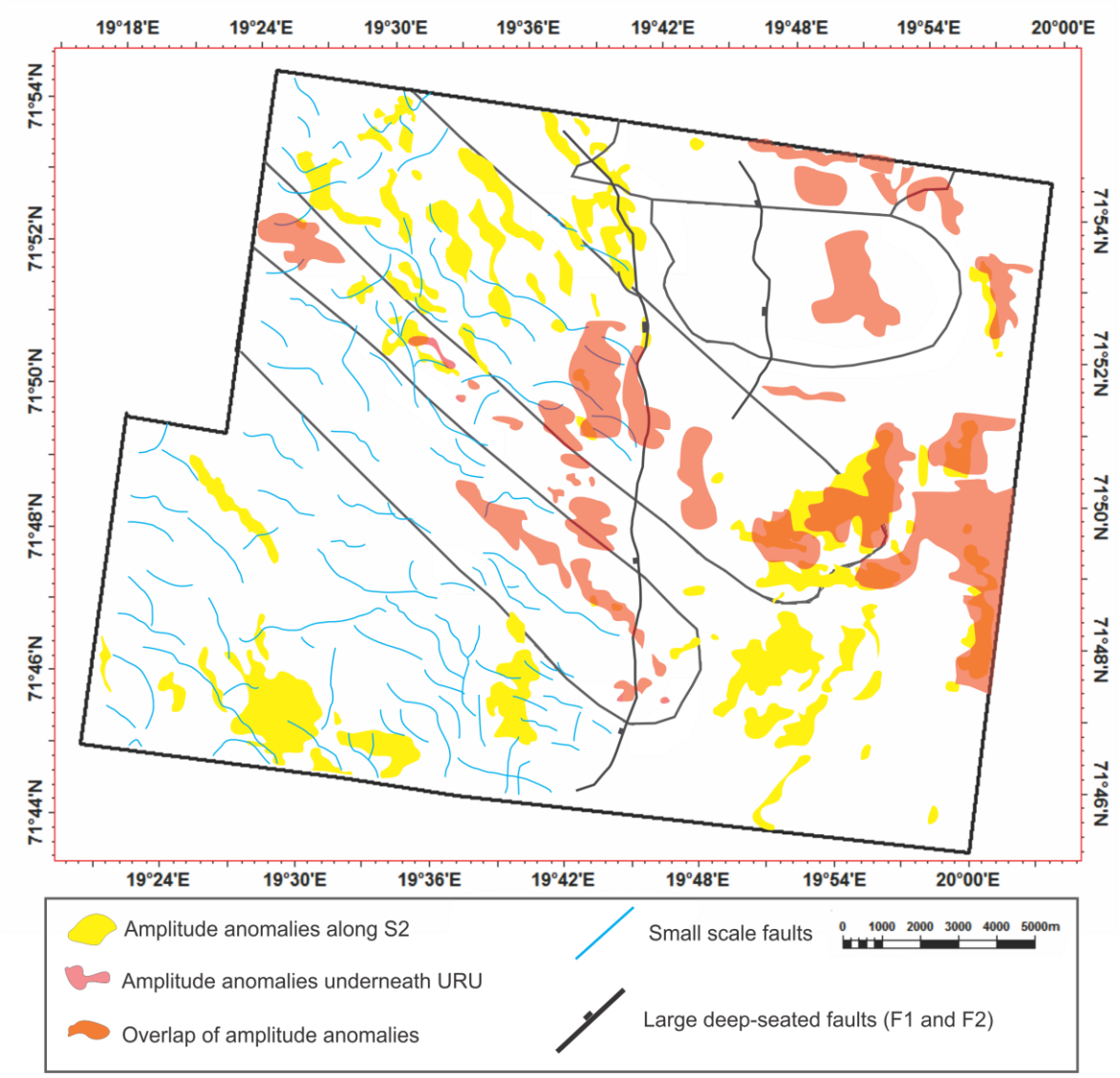


***Figure 5.5-1*** *Summary of the main interpreted features within the Caliente 3D. Yellow shapes indicate amplitude anomalies along the intra-tertiary surface S2 gathered from a RMS amplitude map with zero offset and search window (fig. 5.4-1). Red transparent shapes indicate amplitude anomalies from a RMS map extracting amplitudes from the URU to a horizontal surface 480ms TWT below the seabed (fig. 5.4-5). Orange shapes indicate areas where the amplitude anomalies from the different units overlap each other. Blue lines represent the small scale-faults affecting stratigraphic units from S4-S1, and black bold lines indicate the N-S striking deep-seated faults, F1 and F2. Faults are illustrated based on a variance attribute map along the base tertiary reflector S3 (fig. 5.1-2).Black polygons indicate the lateral extent of the URU depression 1, 2, 3 and 4.*

# 6 Discussion

## 6.1 Fluid migration within the Caliente 3D

The previous result chapter revealed that the amplitude anomalies occur in proximity to faults, acoustic chimneys, zones of acoustic masking, and where upper tertiary strata is truncated by the URU.

This section aim to discuss the fluid migration related features, and to present a conceptual model for the migration pathways within the study area. The conceptual model is based on the gathered results in this thesis and work done by several other authors describing fluid migration and its accompanying seismic features in the southwestern Barents Sea (e.g Chand, et al., 2012; Vadakkepuliyambatta, et al., 2013; Rajan, et al., 2013; Ostanin, et al., 2013).

### 6.1.1 Vertical fluid migration

Indication of vertical fluid migration within the study area are found in relation to faults and zones of acoustic masking.

#### 6.1.1.1 Fluid migration along faults

Faults are the largest group of the seal bypass systems and the fault zones permeability is critical for vertical and lateral migration. Two deep-seated faults with a N-S strike orientation and several small-scale faults were presented in section 5.1.1.

In the northwestern region of the study area several NW-SE oriented elongated amplitude anomalies were identified along surface S2 within the Tertiary sequence (fig. 5.4-3). The majority of these anomalies were identified as gas migrating along faults terminating at this surface. This is based on their seismic expression and the fact that the anomalies and the faults, west of the deep-seated fault F1, has the same orientation (fig. 5.1-2). Enhanced reflectivity between the anomalies were also identified, indicating that the westerly faults both act as vertical and lateral conduits.

The small-scale faults affect stratigraphic levels from surface S4, the Top Kolje Formation, to surface S1 in varying degree and the faults intersects at several location, however the majority

of the faults are recorded within the interval from S4-S2. The identified anomalies along S2 hence indicate gas charged from depths below surface S4. Some of the faults terminates above surface S2, these may act as conduits allowing gas to migrate to shallower levels in the Tertiary sequence. However, no amplitude anomalies have been recorded in association to small-scale faults above S2, but this is probably a result of poor seismic resolution and not the absence of gas.

The deep-seated faults F1 and F2 have limited expression in the seismic data, and their extent is hard to determine. Acoustic masking and dimming of the Base Tertiary reflector (fig.5.4-6 ) are observed along the fault plane of fault F1. Zones of acoustic masking are often related to vertical fluid migration, as for gas chimneys, but there has to be some collaborating evidence to support this theory. Amplitude anomalies mapped below the URU are observed in stratigraphic levels east of fault F1's upper termination (fig. 5.4-6, A), this observation could suggest that the deep-seated faults are/have to some degree been acting as migration paths from the faults lower termination in Triassic strata to it upper extent in the Tertiary unit.

Leakage along faults occur in nearly all parts of the southwestern Barents Sea, especially on the Loppa High and the western fault complexes surrounding it. Large fluid flow features located above deep-seated faults suggest their occurrence is largely fault-dominated (Vadakkepuliyambatta, et al., 2013; Ostanin, et al., 2013). Faults are highly sensitive to stress and their ability to act as conduits for fluids may severely alter as a result of regional tectonic events such as rifting, uplift, erosion and glacial cycles. Along the SE-NW trending faults on the western flank of the Loppa High networks of gas chimneys are identified. These are inferred to represent vertical conduits for fluids developed during the Cenozoic when uplift and erosion affected the southwestern Barents Sea or during the Plio-Pleistocene when glacial uplift or/and erosion reactivated the faults (Rajan, et al., 2013; Vadakkepuliyambatta, et al., 2013). Based on the observation of fluid flow features and their connection to deep-seated fault made by other authors, and the findings in this thesis, a fair assumption that the deep-seated faults F1 and F2 are/or have at some point been acting as vertical conduits is made.

#### 6.1.1.2 Vertical fluid migration along chimneys

Vertical zones of reduced amplitude below high amplitude anomalies are indications of upward focused fluid flow.

In the southwestern region of the study area, an acoustic chimney is identified from an amplitude anomaly along surface S2 (fig.5.4-2). This chimney is interpreted to represent a gas leakage pathway, where the lower termination of the acoustic masking zone is located at approximately at 3400 ms TWT at surface S4, the Top Kolje Formation. Determination of the lower boundary of the chimney is vital to understand the origin of the gas, however the resolution below the Top Kolje formation limits investigation. In addition will gas within the chimney attenuate seismic energy, making the zone of acoustic masking appear deeper than the actual gas charged sediments (Rajan, et al., 2013).

The upper termination of the gas chimney is interpreted to represent a boundary with sufficient sealing capability hindering vertical migration. Based on the large lateral extent of the bright upper termination compared to the more narrow zone of acoustic masking, this boundary also represent a shift from vertical to lateral eastward migration. The presence of enhanced reflections above the chimneys upper termination indicate that the sealing capability of S2 is varying. Vertical leakage though the barrier will occur when the driving forces of the hydrocarbon column exceeds the resisting forces of the seal. This could possibly happen when large amounts of gas is supplied from below and lateral migration do not sufficiently reduce the upward driving force. This mechanism would occasionally release gas to the upper Tertiary levels.

The fact that the gas chimney lies within the same interval as the small-scale faults (S4-S1) suggest that the occurrence of this anomaly appear to be fault controlled. However, no seismically recoverable throws are recorded within in the chimney zone except for along the base Tertiary reflection (fig. 5.4-2 and 5.5-1).

### 6.1.2 Lateral migration

Lateral migration appear to be focussed along the intra Tertiary surface S2 and in the shallow tertiary units above S2. The seismic stratigraphy indicate shallowing towards the Loppa High at all stratigraphic levels (fig. 5.1-1), implying lateral migration towards east. The amplitude anomalies located at S2 (fig.5.4-1) have higher reflection strength compared to those beneath the URU (fig. 5.4-5), suggesting that the intra-tertiary surface exhibit some vertical sealing capability, focussing lateral migration along this surface. Gas accumulating along S2 is suggested to occur where slope gradient decreases (fig. 5.4-4). However as mentioned earlier, the sealing capability of S2 is varying due to the small-scale faults located in this interval and possible leaking though the barrier where fluid supply is large.

Amplitude anomalies in the upper tertiary sequence are observed in stratigraphic units truncated by the URU and above the upper termination of fault F1 (fig. 5.4-6). These anomalies are located in the proximity to the deepest parts of the depressions and along the floors and flanks. Gas entering this unit is inferred to migrate laterally in permeable carrier beds until they the subcrop the URU. The URU represent a lithological barrier between the glacigenic sediments and the Tertiary strata, trapping gas within the beds.

The source of the fluids migrating laterally along S2 and in the upper Tertiary units might be three-fold. They either originate from the fault-dominated area west of the two deep-seated fault where multiple vertical migration paths are identified, or they have migrated laterally upward along permeable beds from west in the Tromsø basin. Vertical migration along the fault F1 is also mentioned as a source for gas at this level.

### 6.1.3 Conceptual model for fluid migration

Based on the discussion in the previous sections a conceptual model have been made, see figure 6.1-1. Vertical migration appear to be dominated by the faulted nature of the study area and fluids migrate along the westerly small scale-fault in stratigraphic units from the Top Kolje Formation, surface S4, into shallow Tertiary strata. Vertical migration along the deep-seated N-S striking faults is also indicated. A change from vertical to lateral migration appears in proximity to the intra Tertiary surface S2.

S2 act as a vertical sealing barrier in large parts of the study area, focusing fluid migration east towards the Loppa high in the shallowing stratigraphic levels. However, leakage trough the barrier resulting from build-up of fluids and faults crossing the barrier, distribute fluids to the shallow Tertiary units. Fluids entering the upper Tertiary units migrate laterally up-dip in permeable carrier beds and accumulate against the erosional unconformity in four deep depressions.

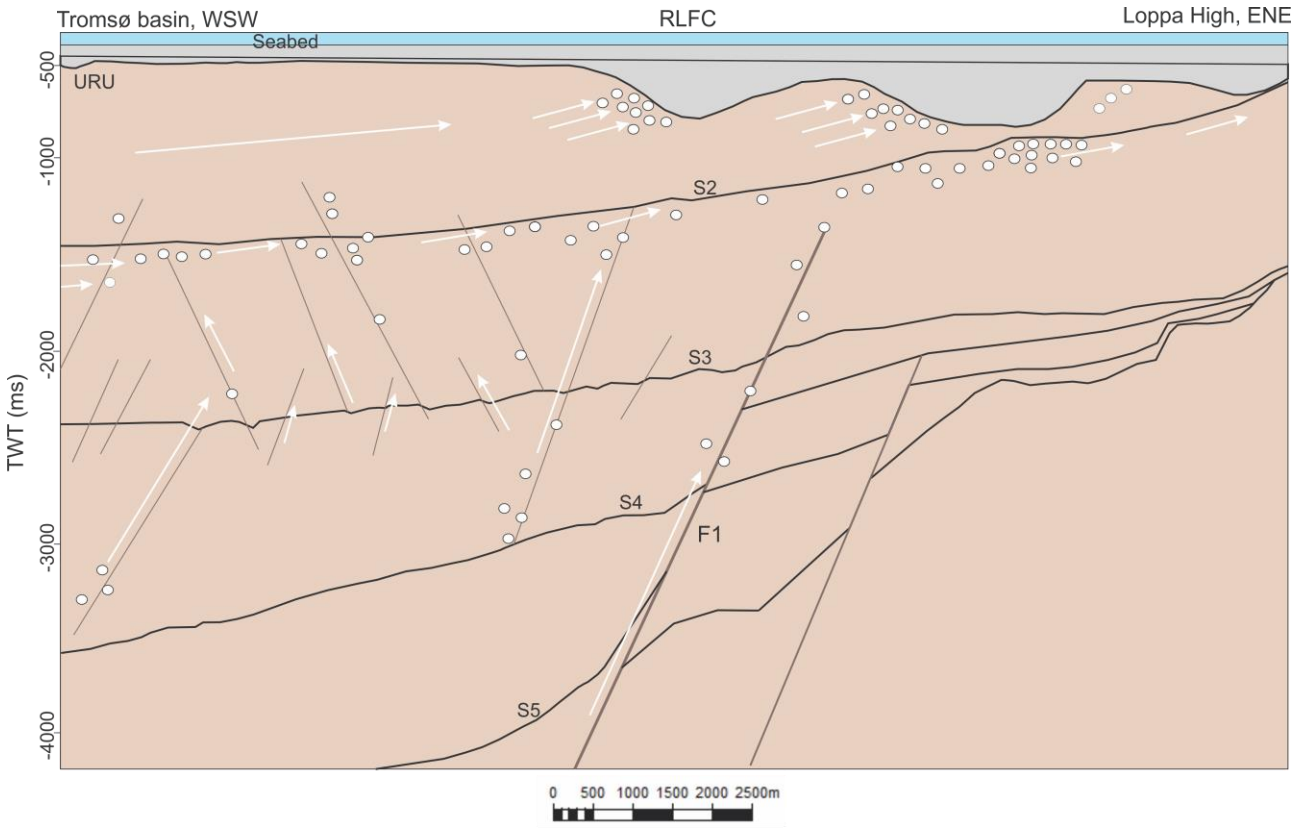


***Figure 6.1-1*** *Conceptual model describing the thought migration pathways within the study area. See text for detailed description. White arrows indicate direction of migration and white bubbles migrating gas.*

## 6.2 URU depressions

Four large depressions were identified on the URU. The following section will discuss possible mechanism related to their formation, linking them to fluid migration and glacitectonic processes.

### 6.2.1 Glacial erosion

Glacial erosion give rise to characteristic form that can tell us something about the past glacier environment. The Barents Sea continental shelf has experienced several glaciations during the Late Cenozoic with ice advancing to the shelf break, thus the hypothesis of glacial erosion being part of the formation of the depressions is warranted.

Depression 1 and 2 differ in size and orientation to depression 3 and 4, and their origin is initially discussed separately.

#### 6.2.1.1 Depression 1 and 2

Depression 1 and 2 are characterized by elongated depressions with well-developed floors, flanks and a steep abrupt slope in the southeastern end (fig. XXX). Based on their appearance and the particularly large size, they fall into the category of intermediate-scale erosional landforms (Benn & Evans, 2010), were tunnel valleys appear to be the feature best describing the depressions.

Tunnel valleys are characterized by steep sides, closed endings and wide undulating floors were overdeepened basis often occur,. They are largely believed to be formed by subglacial meltwater flowing under pressure at the glacial margin (Jørgensen & Sandersen, 2006; Kristensen, et al., 2007; Benn & Evans, 2010; MacRae & Christians, 2013), but their origin is poorly understood. One of the main problems explaining their formation, is the large amount of water needed, which is far in excess of what steady-state basal melting could produce (Benn & Evans, 2010). Three theories are suggested to explain the formation of tunnel valleys.

The first two relate to the theory of sub-glacial meltwater erosion. (1) steady-state meltwater drainage over subglacial deforming sediments, (2) Catastrophic releases of sub-glacial stored meltwater (jökulhlaups). The former explain tunnel valley generation from progressive

excavation of sediments by normal meltwater expulsion in combination with deformation of subglacial beds. The deformed sediments progressively drains, and if this process prolongs tunnel valleys form. Valleys forms by this mechanism are characterized by shallow anastomosing channel systems. The latter is related to sudden catastrophic drainage events, were valleys are excavated by fast headward erosion. These tunnel valleys are recognized by boulder accumulations in out-wash fans, bedforms indicative of subglacial floods, and an anastomosing valley pattern (Kristensen, et al., 2007; Benn & Evans, 2010).

The second theory purpose that the tunnel valleys are products of direct glacier erosion, in the form of quarrying and abrasion and that meltwater erosion play a secondary role. Smed (1998) argue that direct glacial erosion only occur when projected outlet glacier re-sculpture wide pre-existing valleys and create open tunnel valleys. In addition to features resulting from projected outlet glacier, other signs indicate selective linear erosion. Tunnel valleys formed by selective linear erosion requires the valleys to have been ice-filled during formation. Glaciotectonized sediments and subglacial till in the valley infill sequences characterize previously ice-filled valleys. The thicker ice-coverage over the valleys might also alter the basal melting rate, increasing erosion (Jørgensen & Sandersen, 2006). Wide tunnel valleys found in Poland (Niewiarowski, 1995) are inferred to originate from ice tongues and ice stream erosion in pre-exiting smaller tunnel valleys. Niewiarowski (1995) classify the tunnel valleys formed by glacial erosion by size, and argue that these generally range form 1-4km, much wider than those carved by subglacial meltwater (>1km). It is generally thought that direct glacial erosion will affect the tunnel valley flanks, widening the tunnel, and that meltwater erosion deepens it, and that both processes take place when individual wide tunnel valleys are generated (Jørgensen & Sandersen, 2006).

Depression 1 and 2 are respectively 3800m/4249m wide and 15256m/19500m long, making them comparable to the largest subsurface tunnel valleys formed under the European Pleistocene ice sheets, including North America, northern Germany, Poland and on the floor of the North Sea (Benn & Evans, 2010). Their length is not directly comparable, neither is their termination, since the seismic data limits their extent. Their size suggest that, if classified as conventional tunnel valleys, selective linear erosion definitely played a role in their formation.

In map view, tunnel valleys generally are described as slightly sinuous features, and sometimes anastomosing networks occur. The valleys are carved parallel to ice flow direction, making them good indicators of ice sheet direction during their formation. Depression 1 and 2 would hence indicate ice advancement towards west, which is in accordance with the Barents Sea ice sheet behaviour, and the abrupt closed ending in southeast would further represent their onset (fig XX). The depressions in the study area however, do not show any sinuous trends. They appear as parallel straight segments, a trend not common for tunnel valleys. Figure 6.2-1 show an example of two North Sea tunnel valleys. Compared to the depression in the study area, they exhibit clear similarities, but the floors and flanks of the North Sea valleys have clearly undulating floors and flanks, a characteristic indicative for tunnel valleys. The smooth well-developed floor and flanks of the depression in the study area could therefore act to reject the theory of tunnel valley origin, but it could also represent valley re-usage over several glaciations, eroding the depression over and over again resulting in their smooth appearance.  Seismic data acquisition and resolution is also a factors that could smooth their appearance.

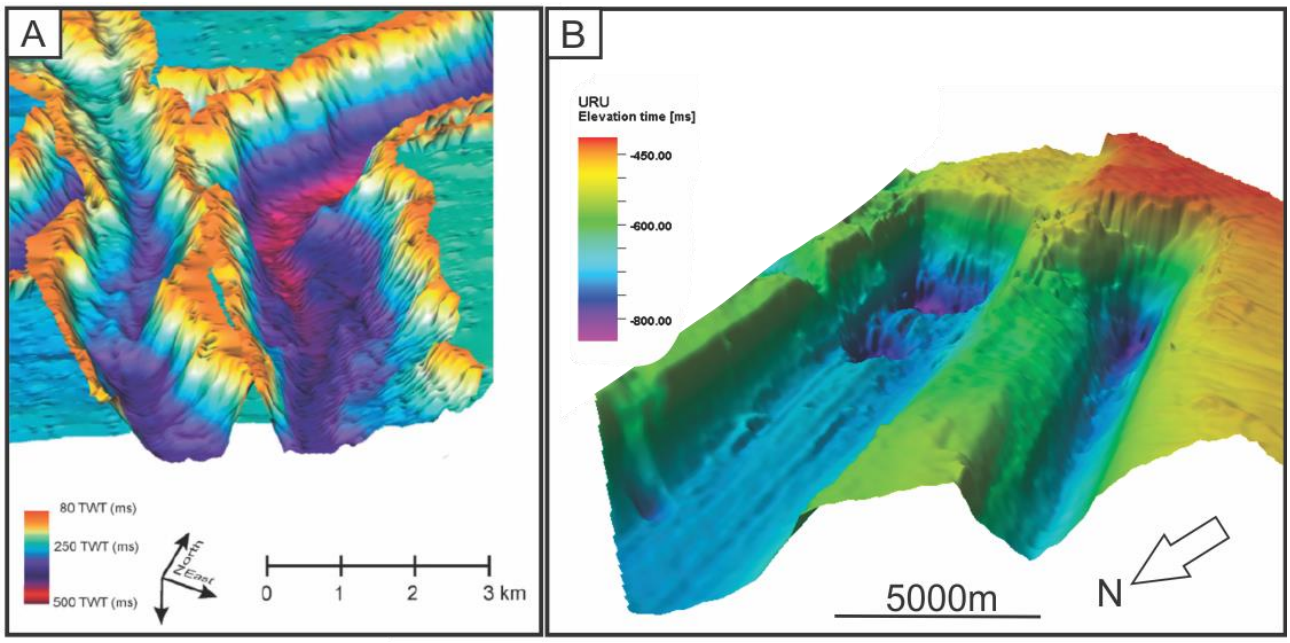


***Figure 6.2-1*** *A) Perspective view of two tunnel valleys in the eastern North Sea. Notice the highly undulating floor and flanks of the valley. Figure gathered from (Kristensen, et al., 2007) B) perspective view of depression 1 and 2 on the URU, notice the more smooth appearance of the floor and flanks compared to the North Sea ones.*

The theory of tunnel valley origin is further questioned based on the regional setting of the study area. The depressions are located on the Tromsøflaket, a shallow bank area in the SW Barents Sea situated in a cold-based ice setting. Such an environment would lack the characteristics of warm fast flowing ice and meltwater drainage and selective linear erosion would probably be restricted to the surrounding troughs, the Bjørnøyrenna and Ingøydjupet. The result chapter examined both the seabed (figure ) and the URU (figure ), and no features indicative of fast flowing ice were found.  However, large amount of melting occurs during deglaciation close to the ice margin and a recent study in the central Barents Sea have revealed the first account of tunnel valley networks in the Northern Hemisphere paleo-ice sheet (Bjarnardóttir, et al., 2017).

The study documented the first tunnel valleys formed beneath the much reduced marine-based Barents Sea ice sheet during late deglaciation. The seabed tunnel valleys are interpreted to have a polygenetic origin, formed by steady-state drainage, outburst floods and ice erosion (Bjarnardóttir, et al., 2017). This warrants that the SW Barents Sea could have had suitable conditions for tunnel valley formation during the establishment of depression 1 and 2, and that

Based on this discussion, a pure tunnel valley origin is not concluded. The many uncertainties previously mentioned and the fact that the seismic data limit the termination of the depressions makes accurate interpretation difficult. The depression show clear similarities to the tunnel valleys and a fair suggestion can be made that some of the mechanisms, meltwater erosion and glacial erosion, played a part in their formation as well. Section 6.3, will discuss other local features that could have assisted in the generation of depression on the URU.

#### 6.2.1.2 Depression 3 and 4

Depression 3 and 4 are characterized by an elongated sub-circular shape and exhibit much of the same features as depression 1 and 2 (section 5.3-4). They are however much smaller in size covering areas of respectively 23.2541 and 12.2623km$^2$.

Depression 3 and 4 show signs of being erosional features as material clearly have been removed from the URU, and based on the E-W orientation of the depressions glacier erosion seems probable. The glacitectonic landform best suitable to describe the size and shape of the depressions are hill-hole pairs.

Hill-hole pairs consist of an ice-thrust hill and a similar looking source depression (section 2.6.2). These features have previously been located in the vicinity of the study area, on the Tromsøflaket (Rise, et al., 2016) and on the Norwegian-Svalbard margin (Ottesen, et al., 2005). However, the depressions in the study area do not show well-developed hills on their downglacier western end (fig. 6.2-2). Absence of the associated hills often occur due to subglacial erosion or long distance transport (Benn & Evans, 2010), which seems probable since the depression is located on the URU and subsequent glaciations occurred after their formation.

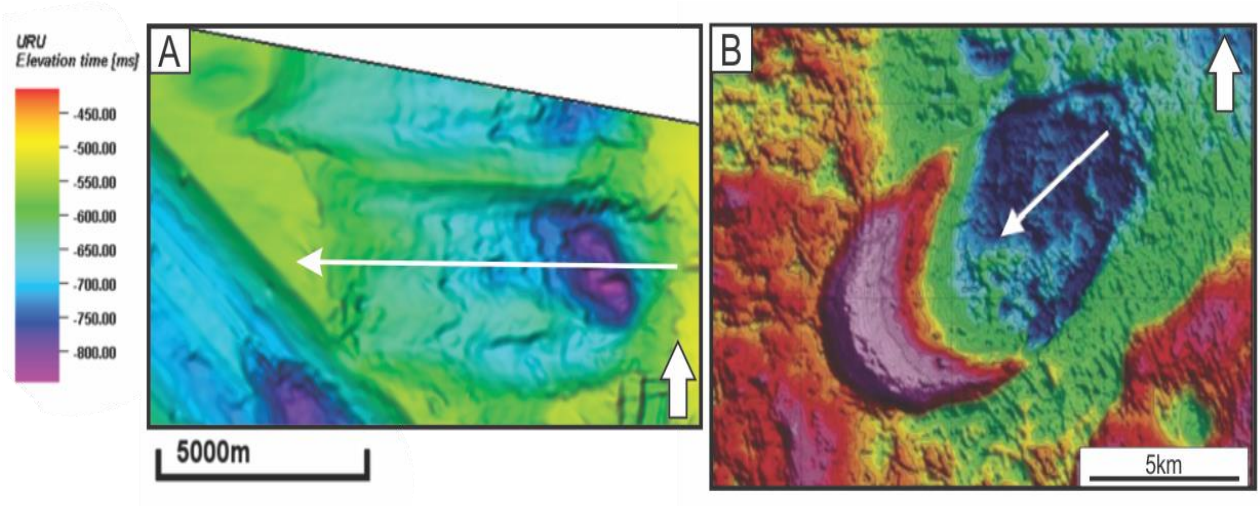


***Figure 6.2-2*** *A) depression 3 and 4 located on the URU in the study area. B) hill-hole pair on the seabed on the mid-Norwegian shelf. Figure modified from (Ottesen, et al., 2005). White arrow indicate direction of paleo ice flow.*

Hill-hole pairs are common features on shallow bank areas, as the Tromsøflaket. Ice here is relatively thin, flows slowly and sometimes frozen to the underlying surface. This freezing of meltwater under the glacier bed could act to drain excess pore water from the sediments leading to overconsolidation and tectonism (Rise, et al., 2016). The fact that the depressions are oriented E-W would suggest paleo ice moving in the same direction, compliant with ice flowing from the Ingøydjupet crossing over the Tromsøflaket.

Together with the missing downglacier hill, the depression on the URU have slope gradients further dissociating them from hill-hole pairs. One of the main characteristics of hill-hole pairs are their steep downglacier slope, but the depressions in the study area show the opposite, with steep slopes on the upglacier side. The steep upglacier slopes of depression 3 and 4 are similar to those of depression 1 and 2, and together with the other characteristics making all of the depressions comparable (section 5.3-.4), a theory that all of the depressions are formed in the same manner is suggested. If this assumption were true, it would exclude the tunnel valley origin of depression 1 and 2 since tunnel valleys are characterized by steep closed endings at both the up- and down-glacier side, and depression 3 and 4 as mentioned earlier have a much smaller slope gradient at the downglacier end.

These observations makes it difficult to classify the depressions as pure glaciotectonic features, and alternative mechanisms for their origin are discussed in the following section relating them to the structural setting and focussed fluid flow in the study area, 6.2.3.

## 6.2.2 Correlation between depressions

### 6.2.2.1 Timing of depression formation

Assuming that the depressions on the URU are features partially eroded by glaciers, and that they form parallel to ice-flow this thesis suggest that the depressions were formed at two different times. Depression 1 and 2 have a NW-SE orientation and depression 3 and 4 an E-W orientation, suggesting that the depressions were formed two at the time. Given that the depressions do not intersect or cross-cut each other, and that they reach the approximately same depth in the tertiary strata, it is difficult to argue for which pair formed first. Figure 6.2-3 cross-cut depression 1,2 and 3, here it is clearly recognized that the interpreted URU horizon connecting depression 2 and 3 show signs of being eroded multiple times by its flat appearance. Hence, no determination of which came first can be made.

If we further the theory from the previous discussion, section 6.2.1.2, that the depression are generated in the same manner, an argument could be made for the former pair being generated at a later stage. Depression 3 and 4 are smaller compared to the first pair, suggesting that their making might have been more short lived, and perhaps during a late stage in deglaciation when ice loses much of its direct erosional influence. Moreover, that depression 1 and 2 have been formed over a longer time span, supporting their lengthy extent. This line of arguments have many pitfalls and a more detailed study of paleo ice flow during the late Cenozoic would probably be more beneficial when determining their age according to their preferred orientation.

### 6.2.2.2 Internal structures

Examination of the internal appearance of the depressions (fig. 5.3-2, 5.3-3 and 5.3-4) reveal that the infilled sediment are composed of a series of cut-and-fill structures (Jørgensen & Sandersen, 2006). The buried depressions consist of 2-3 cut-and-fill structures, including the floors of the depressions. Depression 1 have been interpreted to have thee cut-and-fill structures, while the other depressions have two. The cut-and-fill structures represent the boundaries between the different units identified within the depressions (section 5.3). These boundaries are interpreted to represent erosional surfaces and periods of infilling related to repeated ice sheet advances and retreats (Kristensen, et al., 2007).

Figure 6.2-3 show a seismic profile crosscutting depression 1, 2 and 3. Here a clearly marked boundary between unit 1 and 2 is identified. Figure 6.2-4 show this boundary and its extent within all the depressions. Based on the interpreted boundary, unit correlation between the depressions are possible. Unit 1 within depression 1 and 2 clearly represent the first period of significant infilling within the erosional depressions. Unit 2, even though separated in the seismic profile, also correlate because the boundary separating them can be mapper across the two depressions and their seismic facies show resembling characteristics. Erosion and deposition has however been much more pronounced within depression 1, suggested by the elongated and deep extent of the erosional surface (figure 6.2-4). Unit 1 and 2 within depression 3 and 4 also correlate based on the same arguments. Nevertheless, they show an opposite infill trend, were most of the deposition occurred after the second ice sheet advance. No correlation between the units located the different depression pairs are possible, which furthers the already stated assumption that they were formed at different times.

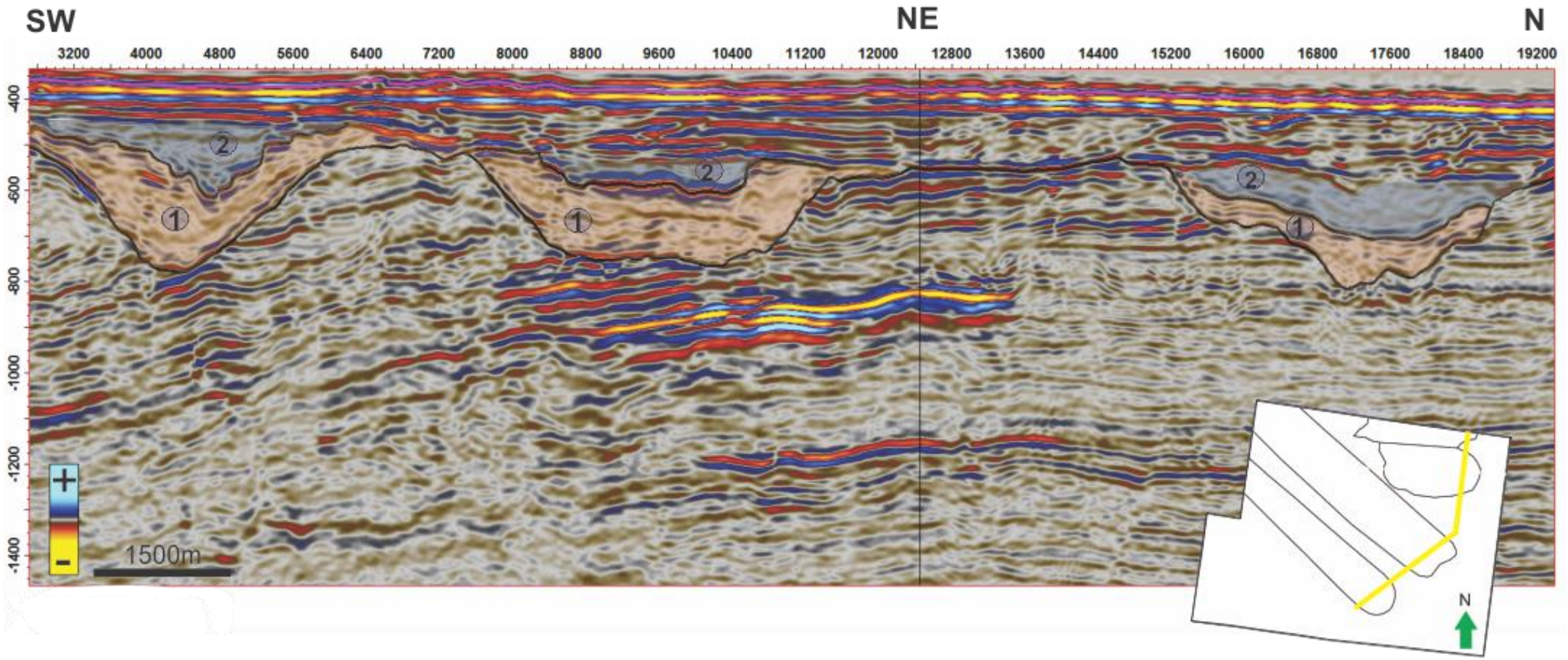


***Figure 6.2-3*** *Seismic section crossing over depression 1,2 and 3 on the URU. A clear boundary separating two units (unit 1 and unit 2) appear within the depressions. The boundary and the units are thought to represent a erosional surface and periods if infilling related to repeated ice sheet advances and retreats. No correlation can be made with the units in depression 1 and 2 to the units in depression 3 and 4. Unit 1 is marked by a transparent orange color while unit 2is marked by blue transparent color. Unit numbers to not represent the numbers presented in the result chapter (section 5.3.1, 5.3.2, 5.3.3). Location of seismic inline is indicated in lower right corner.*

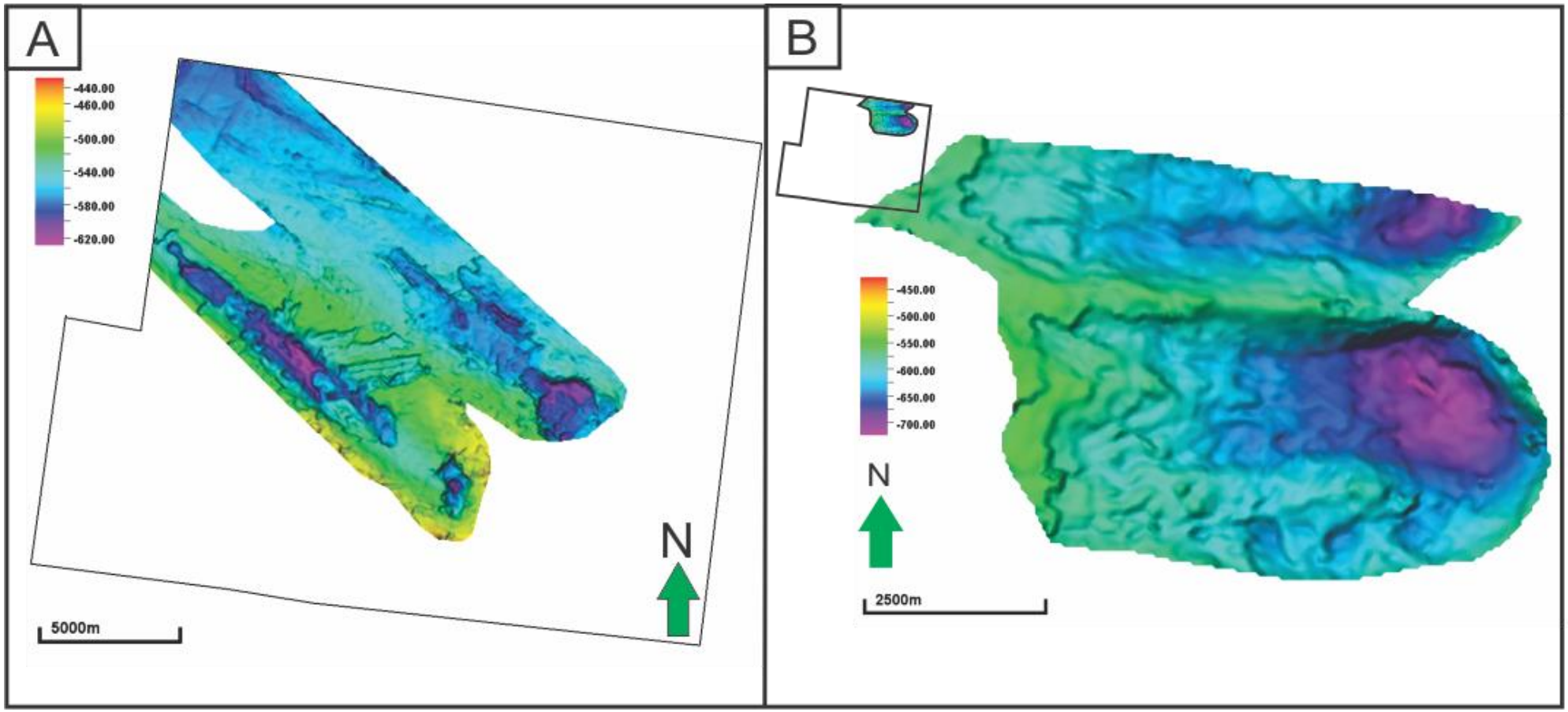


***Figure 6.2-4*** *Map of boundary between unit 1 and 2 within A) depression 1 and 2, and B) depression 3 and 4. These boundaries act to correlate different units within the depression pairs and do not intersect with each other.*

## 6.3 Link between focussed fluid flow and glacial erosion

The previous discussion did not lead to a conclusion on how the elongated depressions were formed, but a connection with glacial erosion seem probable at this point. The early discussion (section 6.1) described the fluid pathways within the study area. A focussing of gas migration though lateral migration in upper Tertiary strata, and leakage along deep-seated faults to the area beneath the depression onset were identified (section 5.3.4). This has led to the theory that these factors, glacial erosion and focused fluid flow, are connected.

Many publications have previously described the connection between gas-charged fluid escape and sub-circular depression on the seabed and buried horizons (Judd & Hovland, 1992; Max, 2003; Fichler, et al., 2005; Windsborrow, et al., 2016). These depressions are inferred to be results of processes common to the glacial environment during the Plio-Pleistocene. Among these are the formation and dissertation of gas hydrates and their connection to hydrocarbon leakage from deep reservoirs.

The gas hydrate system in the SW Barents Sea are strongly influenced by the glacial loading and unloading, erosion, sea level variations, and bottom water temperatures during the late Cenozoic glaciations. These factors led to the deepening of the GHSZ due to seafloor subsidence and sediment removal (Laberg, et al., 1998). Moreover, migration of thermogenic gas from deeper reservoir were severely influenced by the glacial erosion, leading to reactivations of faults affecting their ability to trap hydrocarbons. In addition could migrating gas further increase the thickness of the GHSZ by adding of gas trapped beneath the BSR (Laberg, et al., 1998; Vadakkepuliyambatta, et al., 2013).

During the LGM the GHSZ were approximately 350m below the present day seafloor in the study area (fig.2.5-4) (Chand, et al., 2012). Additionally, leakage along the rotated fault blocks in the RLFC provided a deep source of thermogenic gas to the boundary between the Loppa High and the RLFC (Vadakkepuliyambatta, et al., 2013). The depressions found in the study area lies at depths ranging from 354-390m (depth of depression 4 is not concluded, due to its limiting extent) below the seafloor, indicating they lie out of the GHSZ of the LGM. However, the focussed gas migration in this area would suggest that the zone could have extend deeper, besides the p-wave velocity used for calculations is also approximate, making comparison questionable. Regardless, the depressions would have been located in the hydrate-

forming zone at their early onset, and for the following discussion it is assumed that a GHSZ existed at the depth where the depressions was formed.

Formation of gas hydrate will desiccate and stiffen the host sediments by pore-water piracy, cementation, and the great strength and low volume of the hydrate compared to that of the gas and ice. The movement of ice-sheets are much dependent on the lateral shear at its margin and on the friction at its base, hence gas hydrate formation in the underlying strata would influence the basal friction and the velocity of the moving ice. Such areas of high basal friction are known as sticky spots, vital for the regulation of ice flow as they can lead to ice stream shut down (Windsborrow, et al., 2016). The theory of localized patches with increased basal friction fit well into the conceptual model of focused fluid flow along the deep-seated faults F1 and F2, and the position of the depressions in relation to these. Gas hydrates formed in the overlying units above the deep-seated faults are inferred to create strong frictional bonds with the ice. This process would lead to the formation of a decollement basal failure plane at the lower boundary of the GHSZ, where stiff hydrates overly the low strength over-pressured gas-bearing sediments (Bünz, et al., 2003; Benn & Evans, 2010; Windsborrow, et al., 2016). Subsequent thrusting by the slower moving ice would hence favour glacitectonic decollement in the substrata and sediment removal and re-deposition of the hydrate bearing sediments.

### 6.3.1 Conceptual model

A four-stage conceptual model is purposed for the formation of depression 1 and 2. This model infer the origin of the depressions to glacial erosion, focused fluid flow and gas hydrate formation and is suggested to relate to two ice sheet advancements and retreats.

The first stage of the formation relates to the first Barents Sea Ice sheet advancement towards the western shelf edge. As the ice-sheet moved over the Tromsøflaket the lithostatic pressure beneath the ice significantly increased, leading to a thickening of the GHSZ. Simultaneously the deep-seated fault blocks, F1 and F2, and the small-scale faults focussed deep thermogenic gas leakage towards the Loppa High in shallow tertiary strata. Given the constant supply of gas to localized regions, gas hydrates are inferred to form and create sticky spots. These areas of high basal friction would reduce the velocity of the already slow moving glacier and create a decollement plane at the base of the GHSZ.

The second stage is initiated when the ice sheet experiences a change in velocity, and ice streams within the Barents Sea ice sheet started to drain. This led to a decrease in ice thickness and a subsequent upward shift of the GHZS. Gas hydrates started do dissociate below the GHSZ and free gas accumulations trapped beneath the BSR became overpressured. Subsequent ice movement dislocated huge amounts hydrate bearing sediments at the decollement plane, eroding and re-depositing the hydrate bearing sediments further west. Continued erosion in form of pressurized meltwater and direct glacial erosion continued, generating elongated depressions with well-developed floors and sides.

The third stage is marked by the first retreat of the ice sheet were large amounts of glacial material were deposited within the depressions, and the first cut-and-fill structure were generated. The previous erosion and the unit deposited at this stage is thought to have generated a vertical seal, trapping gas beneath the depression.

The fourth and last stage represent the second glacial advancement and retreat. The ice sheet moved with the same orientation as the previous, hence erosion where confined to the depression floor and flanks were ice thickness were the greatest. It is proposed that the thickness of the ice sheet at this stage was not sufficient to generate a GHSZ reaching depths below the deepest point in the depressions, and gas were confined below the depressions, or migrated laterally towards the Loppa High, out of the study area. As the ice sheet advanced

over the depression and retreated, pressurized meltwater and ice located within the depression altered the upper boundary of the first deposited unit resulting in a highly undulating erosional boundary. Glacial sediments were continuously being deposited during the ice sheet retreat, and together with the second erosional boundary these deposits make up the second cut-and-fill structure, and the formation of the depressions were complete.

Subsequent subsidence and deposition from other glacial interstadials have preserved the depressions within the geological record of the study area.

Depression 3 and 4 are thought to have formed in the same manner as depression 1 and 2, however at another time when paleo ice flow were oriented E-W, and with a different erosional strength/or in a shorter timespan as they are much smaller in size. Moreover, the conceptual model is uncertain and further seismic analysis of the downglacier depression termination and sedimentary infill are proposed to gain a better classification of the tunnel valley resembling features.

# 7 Conclusion

- A 3D seismic survey (Caliente 3D) and 2D seismic lines located in the RLFC, bordering the Loppa High and the Tromsø basin have allowed mapping of the seismic stratigraphy, faults, amplitude anomalies and geomorphologic features in the SW Barents Sea.

- Seismic amplitude anomalies identified along an intra-Tertiary reflector, and in the upper Tertiary unit between the URU and a horizontal surface 480ms TWT below the seabed are thought to represent gas migration from depths below the inferred Top Kolje Formation.

- Mapping of faults, stratigraphy and amplitude anomalies revealed that vertical fluid migration are dominated by the faulted nature of the study area and fluids migrate along the westerly small-scale faults and the deep-seated faults (F1 and F2) into shallow Tertiary strata. A change from vertical to lateral migration are observed in proximity to the intra-Tertiary reflector. Lateral migration is suggested to follow the shallowing stratigraphy focussing fluid flow towards the Loppa High.

- Four elongated deep depression, with well-developed floors and sides are mapped on the interpreted URU reflector, S1. The depression have lengths ranging from 8.6-19.500km, widths from 1.8-4.2km and reached depths up to 390m below the seabed. Two of the depressions (dep. 1-2) have a NW-SE orientation and the other depressions (dep. 3-4) an E-W orientation. The orientation are inferred to represent paleo ice sheet streaming directions. Several theories for their origin are discussed, relating them to tunnel valleys, hill-hole pairs or an involvement between fluid flow and gas hydrate formation.

- The mapped deep-seated faults and the small-scale faults in the western region of the study area are suggested to have played an important role during the formation of the depressions as repeated glacial cycles would have affected the faults ability to efficiently trap gas form deeper reservoirs.

- Focussed fluid flow and glacial erosion are likely to play a major part in the origin of the depressions. A four-stage conceptual model is proposed for the formation of the depressions on the URU. Localized formation of gas hydrates create sticky spots underneath the Barents Sea Ice Sheet. Brittle glacitectonic deformation along a decollement failure plane at the base of the fluctuating GHSZ is suggested, leading to glacial erosion of the depressions and re-deposition of the gas hydrate bearing sediments. Subsequent glacial advances and retreats have continued erosion within the depression and deposited substantial amount of glacial material within them.

# 8 References

Aber, J. S., & Ber, A. (2007). Developments in Quarternary Sciences volume 6: Glaciotectonism. I *Developments in Quarternary Science* (ss. 1-246). London: Elsevier Science.

Andreassen, K. (2009). *Marine geophysics, Lecture notes for GEO-3123.* Tromsø.

Andreassen, K., Laberg, J. S., & Vorren, T. O. (2008). Seafloor geomorphology od the SW Barents Sea and its glaci-dynamic implications. *Geomorphology, 97*, 157-177.

Andreassen, K., Nilssen, E. G., & Ødegaard, C. M. (2007). Analysis of Shallow gas and fluid migration within the Plio-pleistocene sedimentary succession of the SW barents Sea continental margin using 3D seismic data. *Geo-Marine Letters, 27*(2), 155-171.

Aschenbrenner, B. C., & Achauer, C. W. (1960). minimun conditions for migration og oil in water-wet carbonate rocks. *AAPG Bull, 44*, 235-243.

Babitto, J. F., & Tsouris, C. (2009). Physical properties of gas hydrates: A review. *journal of thermodynamics, 2010*, 1-12.

Badley, M. E. (1985). *Practical seismic interpretation.* Boston: International Human Resources Development Corporation.

Benn, D. I., & Evans, D. J. (2010). *Glaciers & Glaciation* (2nd edition. utg.). London: Taylor and Francic.

Berndt, C. (2005). Focused fluid flow in passive continental margins. *Philosophical Transactions of the Royal society, 363*, 2855-2871.

Berndt, C., Bünz, S., & Mienert, J. (2003). Polygonal fault systems on the mid-Norwegian margin: a long-term source for fluid flow. *Geological Society, 216*, 283-290.

Bjarnardóttir, L. R., Winsborrow, M. C., & Andreassen, K. (2017). Large subglacial meltwater features in the central Barents Sea. *The Geological Society of America, 45*(2), 159-162.

Bjørlykke, K. (2010). *From Sedimentary Environments to Rock Physics.* Berlin: Springer-Verlag.

Brown, A. J. (2003). *interpretation of three dimentional seismic data* (6. utg.). Tulsa: American Association of petroleum geologists.

Bulat, J. (2005). Some considerations on the interpretation of seabed images based on commersial 3D seismic in the Faroe-Shetland Channel. *Basin Reasearch, 17*, 21-42.

Bünz, S., Mienert, J., & Berndt, C. (2003). Geological controls on the Storegga gas-hydrate system of the mid-norwegian continental margin. *Earth and Planetary Science Letters, 209*, 291-307.

Cartwright, J., Huuse, M., & Aplin, A. (2007). Seal bypass systems. *The American Association of Petroleum Geologist, 91*(8), 1141-1166.

Chand, S., & Minshull, T. A. (2003). Seismic constraints on the effects of gas hydrate on sediment physical properties and fluid flow: a review. *Geofluids, 3*, 275-289.

Chand, S., Mienert, J., Andreassen, K., Knies, J., Plassen, L., & Fotland, B. (2008). Gas hydrate stability zone modelling in areas of salt tectonics and pockmarks of the Barents Sea suggests an active hydrocarbon venting system. *Marine and petroleum geology, 25*, 625-636.

Chand, S., Thorsnes, T., Rise, L., Brunstad, H., Stoddart, D., Bøe, R., . . . Svolsbru, T. (2012). Multiple episodes of fluid flow in the SW Barents Sea (Loppa High) evidence by gas flares, pockmarks and gas hydrate accumulation. *Elsevier, 331-332*, 305-314.

Chopra, S., & Marfurt, K. J. (2005). Seismic attributes- A historical perspective. *Society of Exploration geophysics, 70*(5), 3SO-28SO.

Chopra, S., Castagna, j., & Portniaguine, O. (2006). Seismic resolution and thin-bed reflectivity unversion. *CSEG RECORDER, 31*(1), 19-25.

Clark, C. D., Tulaczyk, S. M., Stokes, C. R., & Canals, M. (2003). A groove-ploughing theory for the production of mega-scale glacial lineations, and its inplications for ice-stream mechanics. *Journal of Glaciology, 49*(165), 240-256.

Clennell, B. M., Hovland, M., Booth, J. S., Henry, P., & Winters, W. J. (1999). Formation of natural gas hydrates in marine sediments. 1. Comceptual model of gas hydrate growth conditioned by host properties. *Journal of geophysical research, 104*(B10), 22985-23003.

DAKE, L. (1978). *Fundementals of reservoir engineering* (1. utg.). Amsterdam: ELSEVIER.

Durand, B. (1988). Understanding og HC migration in sedimentary baisins (present state of knowledge). *Organic Geochemistry, 13*(1-3), 445-459.

Egholm, D. L., Clausen, O. R., Sandiford, M., Kristensen, M. B., & Korstgård, J. A. (2008). The mechanics of clay smearing along faults. *The Geological Society of America, 36*(10), 787-790.

Etiope, G., & Martinelli, G. (2001). Migration of carrier and trace gases in the geosphere: an overview. *Physics of Earth and Planetary Interiors, 129*(2002), 185-204.

Faleide, J. I., Gudlaugsson, S. T., & Jacquart, G. (1984). Evolution of the western Barents Sea. *Marine and Petroleum Geology, Elsevier, 1*(2), 137-150.

Faleide, j. i., Solheim, A., Fiedler, A., Hjelstuen, B. O., Andersen, E. S., & Vanneste, K. (1996). Late Cenozoic evolution of the western Barents Sea-Svalbard continental margin. *Global and Planetary Change, 12*(1), 53-74.

Faleide, J. I., Vpgenes, E., & Gudlaugsson, S. T. (1993). Late Mesozoic-Cenozoic evolution of the south-western Barents Sea in a regional rift-shear tectonic setting. *Marine and petroleum geolegy, 10*, 186-214.

Fertl, W. H., & Chilingarian, G. V. (1976). The importance of abnormal pressures to the oil industy. *Society of Petroleum Engineers, 29*(4), 1-11.

Fichler, C., Henriksen, S., Rueslaaatten, H., & Hovland, m. (2005). Noth Sea Quarternary morhology from seismic ang magnetic data: indications for gas hydrates during glaciations? *Petroleum Geoscience, 11*, 331-337.

Gabrielsen, R. H., Færseth, R. B., Jensen, L. N., Kalheim, J. E., & Riis, F. (1990). *Structural elements of the norwegian continental shelf. part 1: The Barents Sea Region.* stavanger: Oljedirektoratet.

Halland, E. K., Bjørnestad, A., Magnus, C., Riis, F., Meling, I. M., Gjeldvik, I. T., . . . Pham, V. (2016). *www.npd.no*. Hentet November 17.11.2016, 2016 fra http://www.npd.no/global/norsk/2-tema/lagring-og-bruk-av-co2/co2-atlas-barents-sea.pdf

Henriksen, E., Ryseth, A. E., Larssen, G. B., Heide, T., Rønning, K., & Sollid, K. (2011). Tectonostratigraphy of the greater Barents Sea: implications for petroleum systems. *Geological society, 35*, 163-195.

Judd, A. G., & Hovland, M. (1992). The evidence of shallow gas in marine sediments. *continental shelf research, 12*(10), 1081-1095.

Jørgensen, F., & Sandersen, P. B. (2006). Buried and open tunnel valleys in Denmark-erosion beneath multiple ice sheets. *Quartenary Science Reviews, 25*, 1339-1363.

Knutsen, S. M., Skjold, L. J., & Skott, P. H. (1992). Palaeocene and eocene development of the Tromsø Basin- sedimentary response to rifting and early aes-floor spreasing in the Barents Sea area. *norsk geologisk tidskrift, 72*, 191-207.

Kristensen, T. B., Huuse, M., Piotrowski, J. A., & Clausen, O. R. (2007). A morphometric analysis of tunnel valleys in the eastern North Sea based in 3D seismic data. *Journal of Quarternary Science, 22*(8), 801-815.

Krooss, B. M., & Laythaeuser, D. (1996). Molecular Diffusion of light hydrocarbons in sedimentary rocks and its role n migration and dissipation of natural gas. *AAPG memoir, 66*, 173-185.

Kvenvolden, K. A. (1998). A primer on the geological occurance of gas hydrate. *Geological Society, London, Special Publications, 137*, 9-30.

Laberg, J. S., Andreassen, K., & Knutsen, S. M. (1998). Inferred gas hydrate on the Barents Sea shelf- a model for its formation and a volume estimate. *Geo-Marine letters, 18*, 26-33.

Larssen, G. B., Elvebakk, G., Nilsson, I., Henriksen, L. B., Samuelsberg, T. J., Svånå, T. A., . . . Worsley, D. (2002). *www.reasearchgate.net*. Hentet november 18.11.2016, 2016 fra https://www.researchgate.net/profile/Tommy_Samuelsberg/publication/228993226_Upper_Paleozoic_Lithostratigraphy_of_the_southern_Norwegian_Barents_Sea/links/0f31752dce4627c90f000000.pdf

Løseth, H., Gading, M., & Wensaas, L. (2009). Hydrocarbon leakage interpreted on seismic data. *Marine and Petroleum Geology, 26*(7), 1304-1319.

Løseth, H., Wensaas, L., Arntsen, B., Hanken, N. M., Basire, C., & Graue, K. (2011). 1000m long gas blow-out pipes. *Marine and petroleum geology, 28*, 1047-1060.

MacRae, R. A., & Christians, A. R. (2013). A reexamination of Pleistocene tunnel vally distribution on the central Scotian Shelf. *can.J.Eart Sci, 50*, 535-544.

Mann, D. M., & Mackenzie, A. S. (1990). Prediction of pore fluid pressures in sedimentary basins. *Marine and Petroleum Geology, 7*(1), 55-65.

Maslin, M., Owen, M., Betts, R., Day, S., Jones, T. D., & Ridgwell, A. (2010). Gas hydrates: past and future geohazard. *Philosophical transactions of the royal society A, 368*(1919).

Max, m. D. (2003). *Natural Gas Hydrate. in Oceanic and permafrost Environments* (5. utg.). Springer.

Max, M. D., & Johnson, A. H. (2014). Hydrate petroleum system approach to natural gas hydrate exploration. *Petroleum Geoscience, 20*, 187-199.

Niewiarowski, W. (1995). Diagnosic fetures of sub-glacial channels of the Chelmo-Dobrzyn and the eastern Gniezo lakelands. *Questiones Geographicae, 4*, 225-231.

Noreco, Lundin, Conoco Phillips, & Other members of the Discos Consortium. (2013). *Norlex-norwegian Interactive offshore Stratigraphic lexicon*. Hentet 05 17.05.2017, 2017 fra http://nhm2.uio.no/norlex/StandardLithostratigraphicWallchartOffshoreNorway.pdf

NPD. (2016, 12 13). *www.factpages.npd.no*. Hentet 12 13, 2016 fra http://factpages.npd.no/FactPages/default.aspx?nav1=survey&nav2=PageView|Finished|2011&nav3=7484&culture=en

Ostanin, I., Anka, Z., Primo, R. d., & Bernal, A. (2013). Hydrocarbon plumbing systems above the Snøhvit gas field:Structural control and inplications for thermogenic methane leakage in the Hammerfest Basin, SW Barent Sea. *Marine and petroleum Geology, 43*, 1-20.

Ottesen, D., Dowdeswell, J. A., & Rise, L. (2005). Submarine landforms and the reconstruction of fast-flowing ice streams within large Quaternary ice sheet: The 2500-km-long Norwegian Svalbard margin(57-80N). *The Geological Society of America Bulletin, 117*, 1033-1050.

Rafaelsen, B. (2006). seismic resolution (and frequency filtering). *University of Tromsø*.

Rafaelsen, B., Andreassen, K., Kuilman, L. W., Lebesbye, E., Hogstad, K., & Midtbø, M. (2002). Geomorphology of buried glacigenic horizons in the Barent Sea from three-dimentional seismic data. *Geological Society, 203*, 259-276.

Rajan, A., Bünz, S., Mienert, J., & Smith, A. J. (2013). Gas hydrade systems in petroleum provinces of the SW-Barents Sea. *Marine and Petroleum Geology, 46*, 92-106.

Rise, L., Bellec, V. K., Ottesen, D., Bøe, R., & Thorsnes, T. (2016). Hill-hole pairs on the Norvegian continental shelf. *Atlas of Submarine Glacial Landforms:Modern, Quarternary and Ancient. Geological Society, London, 46*, 203-204.

Schlumberger. (2011). *Petrel Geophysics.* Huston: Schlumberger.

Schowalter, T. T. (1979). Mechanics of Secondary Hydrocarbon Migration and Entrapment. *The American Association og Petroleum Geologists Bulletin, 63*(5), 723-760.

Selly, R. C., & Sonnenberg, S. A. (2015). *Elements of petroleum geology* (third. utg.). Academic Press.

Sheriff, R. E. (1985). Aspects of Seismic Resolution: Chapter 1. I *Seismic Stratigraphy ||: An Integrated Approach to Hydrocarbon Exploration* (ss. 1-10). Tulsa, Okla: American Assosiation of Petroleum Geologists.

Sheriff, R. E. (1985). Limitations on Resolution of Seismic Reflections and Geological Detail Derivable from Them. I *Seismic Stratigraphy* || - *applications to hydrocarbon exploration* (ss. 3-14). Tulsa, Okla: American Association of Petroleum Geologists.

Sloan, E. D. (1998). Gas Hydrates: Review of Physical/chemical Properties. *American Chemical Society, 12*(2), 191-196.

Sloan, E. D. (1998). Physical/chemical properties of gas hydrates and application to world margin stability and climate change. *Geological Society, London, 137*, 31-50.

Smed, P. (1998). Die Entstehung der dänischen und norddeutschenRinnentäler (Tunneltäler) – Glaziologische Gesichtspunkte. *Eiszeitalter und Gegenwart, 48*, 1-18.

Smelror, M., Petrov, O. V., Larssen, G. B., & Werner, S. (2009). *Geological History of the Barents Sea* (1. utg.). trondheim: Norges geologiske undersøkelser.

Tissot, B., & Welte, D. (1978). *Petroleum formation ans occurence: A new approach to oil and gas exploration* (1. utg.). Berlin: Springer Science & business Media.

Vadakkepuliyambatta, S., Bünz, S., Mienert, J., & Chand, S. (2013). Distribution of subsurface fluid flow system in the SW Barents Sea. *Marine and Petroleum Geology, 43*, 208-221.

Vadakkepuliyambatta, S., Bünz, S., Tasianas, A., & Mienert, J. (2016). Iceberg ploughmarks in the SW Barents Sea imaged using high-resolution P-cable 3D seismic data. *The Geological Society of London, 46*, 281-282.

Verweij, J. M. (1993). *hydrocarbon migration system analysis.* Amsterdam: Elsevier.

vorren, T. O., Landvik, J. Y., Andreassen, K., & Laberg, J. S. (2011). Glacial history of the Barents Sea Region. *Developments in Quartenary Science, 15*, 361-372.

Windsborrow, M., Andreassen, K., Hubbard, A., Faverola, A. P., Guldlaugsson, E., & Patton, H. (2016). Regulation of ice stream flow through subglacial formation og gas hydrates. *Nature geoscience, 9*, 370-375.

Winsborrow, M. C., Andreassen, K., Corner, G. D., & Laberg, J. S. (2009). Deglaciation of a marine-based ice sheet: Late Weichselian palaer-ice dynamics and retreat in the southern Barents Sea reconstructed from onshore and offshore glacial geomorphology. *Quarternary Science Reviews, 29*, 424-442.

Winters, B., & Lorenson, T. (2002). *https://soundwaves.usgs.gov/2002/09/gas-hydrateLG.jpg*. Hentet 05 04, 2017

Worsley, D. (2008). The post-Caledonian development of Svalbard and the western Barents Sea. *Polar research, 27*, 298-317.